CONTROLLING PERFORMANCE OF LAMINATED COMPOSITES USING PIEZOELECTRIC MATERIALS

A Thesis

by

ZEAID FOUAD MOHAMMED HASAN

Submitted to the Office of Graduate Studies of
Texas A&M University
in partial fulfillment of the requirements for the degree of

MASTER OF SCIENCE

December 2010

Major Subject: Mechanical Engineering

Controlling Performance of Laminated Composites Using Piezoelectric Materials

CONTROLLING PERFORMANCE OF LAMINATED COMPOSITES USING PIEZOELECTRIC MATERIALS

A Thesis

by

ZEAID FOUAD MOHAMMED HASAN

Submitted to the Office of Graduate Studies of
Texas A&M University
in partial fulfillment of the requirements for the degree of

MASTER OF SCIENCE

Approved by:

Chair of Committee,	Anastasia Muliana
Committee Members,	J.N Reddy
	Rashid Abu Al-Rub
Head of Department,	Dennis O'Neal

December 2010

Major Subject: Mechanical Engineering

ABSTRACT

Controlling Performance of Laminated Composites Using Piezoelectric Materials.

(December 2010)

Zeaid Fouad Mohammed Hasan, B.Sc., Jordan University of Science and Technology

Chair of Advisory Committee: Dr. Anastasia Muliana

Composite materials are increasingly used in aerospace, underwater, and automotive structures. Their use in structural applications is dictated by the outstanding strength and stiffness while being lightweight in addition to their flexibility in tailoring the desired performance in the design of structures. The present study focuses on the failure analysis and shape control of smart composite laminates under coupled hygrothermal, electric and mechanical stimuli. A linear thermo-electro-elastic constitutive model for transversely isotropic materials is used for each ply in the composite laminates. The first-ply failure and ultimate laminate failure criteria of composite laminates are used to predict the failure stress and mode of the composite laminate where we incorporate various commonly known macroscopic failure criteria including Tsai-Hill, Tsai Wu, maximum stress and maximum strain for each lamina.

We study the use of piezoelectric materials such as lead zirconate titanate (PZT) and piezoelectric fiber composites as actuators for controlling deformation in composite laminates; this study focuses on bending deformation. The purpose is to minimize unwanted deformation, such as the one due to hygrothermal effect, by applying counter

deformation to avoid failure in such composite laminates. In addition, analysis based on the Classical Laminate Theory (CLT) is performed for Carbon/Epoxy (AS4/3501-6) thin laminate with stacking sequence $[90/45/-45/0]_s$ under uniaxial and biaxial in-plane loading.

One of the major types of failure in smart structures is caused by debonding of the actuator from the host structure which is caused by the high stress discontinuity between the interface of the host structure and the active part. By using embedded actuators, such that the active part is incorporated into one of the layers of the composite beam during the manufacturing process, the stress concentration effect can be reduced while obtaining similar actuation values. Moreover, a control algorithm is proposed that enables the composite laminate to overcome the failure load by using piezoelectric materials where a counter electric voltage could be applied which prevents failure from occurring. Furthermore, computer software called “Hyper Composite” was developed using Action Script® and Adobe Flash® in order to perform stress and failure analysis for general composite laminates. Several carpet plots were also generated to show the interacting behavior of two independent variables such as Young’s modulus, Poisson’s ratio, shear modulus and the coefficient of thermal and moisture expansion at different percentile constitutions for the laminate different plies. This computer software is useful for estimating overall properties of smart composite laminates in designing smart composite structures.

ACKNOWLEDGMENTS

First I would like to express my special thanks to my advisor, Dr. Anastasia Muliana, for her wisdom and guidance throughout my work and preparation of this thesis. Additionally, I would like to extend my deep thanks and appreciation to my committee member, Dr. J.N. Reddy and Dr. Rashid Abu Al-Rub, for their support as members of my advisory committee and for their encouragement. I would also like to thank my friend, Suhyib Al-Absi, for his generous assistance and help during the preparation for the Hyper Composite program. I would also like to thank my parents and sister, Fatima, for their support and encouragement. They were always there whenever needed. Finally, I would also like to thank my friends and colleagues, Mohammed Alqattawi, Muneer Masad, Ahamd Ashour, Ahmad Bani Younes, Dr.Wael, Nasir Al-Dien, Orkan and Ghassan Atmeh, for their help and support.

TABLE OF CONTENTS

Page

CHAPTER Page

LIST OF FIGURES

Page

Page

Page

Page

Page

LIST OF TABLES

Page

Page

Page

Page

NOMENCLATURE

[A] = Extensional stiffness matrix

[B] = Coupling stiffness matrix

[C] = Stiffness matrix

[D] = Bending stiffness matrix

$\mathbf{E_1}$ = Longitudinal Young's Modulus

$\mathbf{E_2}$ = Transverse Young's Modulus

$\mathbf{F_{1t}}$ = Longitudinal Tensile Strength

$\mathbf{F_{2t}}$ = Transverse Tensile Strength

$\mathbf{F_6}$ = In-plane shear Strength

$\mathbf{F_{1c}}$ = Longitudinal Compressive Strength

$\mathbf{F_{2c}}$ = Transverse Compressive Strength

$\mathbf{G_{12}}$ = In-plane Shear Modulus

h = Laminate Thickness

$\mathbf{M_x}$, $\mathbf{M_y}$ = Bending Moments per unit length

$\mathbf{N_x}$, $\mathbf{N_y}$ = Normal force per unit length

[Q] = Reduced Stiffness Matrix

[T] = Transformation Matrix

u = Displacement in x direction

v = Displacement in y direction

w = Displacement in z direction

n = Number of plies in the laminate

$\mathbf{t_k}$ = Thickness of the ply

$\mathbf{r_1}$, $\mathbf{r_{12}}$ = Stiffness Reduction Factors

$\mathbf{\nu_{12}}$ = Major Poisson's ratio

$\mathbf{\nu_{21}}$ = Minor Poisson's ratio

$\mathbf{\alpha_1}$ = Longitudinal thermal expansion coefficient

$\mathbf{\alpha_2}$ = Transverse thermal expansion coefficient

$\mathbf{\beta_1}$ = Longitudinal moisture expansion coefficient

$\mathbf{\beta_2}$ = Transverse moisture expansion coefficient

$\mathbf{d_{ij}}$ = Piezoelectric strain coefficients

$\mathbf{e_{ij}}$ = Piezoelectric stress coefficients

ξ_i = Electric field components

V = Electric potential

ω_{ij} = Dielectric coefficients

CHAPTER I

INTRODUCTION

Composite materials are multiphase materials obtained through the artificial combination of different materials in order to attain properties that the individual components by themselves cannot attain. Applications of composite materials abound and continue to expand. They include aerospace, aircraft, automotive, marine, energy, infrastructure, armor, biomedical, and recreational (sports) applications. Aerospace structure, such as space antennae, mirrors, and optical instrumentation, make use of lightweight and extremely stiff graphite composite. A very high degree of dimensional stability under severe environmental conditions can be achieved because these composite can be designed to have nearly zero coefficients of thermal and hydric expansion. The high-stiff, high-strength, and low-density characteristics make composites highly desirable in primarily and secondary structures of both military and civilian aircraft. The Boeing 777 aircraft, for example, uses composites in fairings, floor beams, wing trailing edge surfaces, and empennage. The strongest sign of acceptance of composites in civil aviation is their use in the Boeing 787 aircraft and the world's largest airliner Airbus A380. Composite materials, such as carbon/epoxy and graphite/titanium, account for approximately 50% of the weight of the Boeing 787, including most of the fuselage and wing. Composites are used in various forms in the transportation industry, including automotive parts and automobile, truck, and railcar frames. In the energy

---

This thesis follows the style of *Engineering Structures*.

production field, carbon fiber composites have been used in the blades of wind turbine generators that significantly improve power output at a greatly reduced cost.

Composites have unique advantages over monolithic materials, such as high strength, high stiffness, long fatigue life, low density, and adaptability to the intended function of the structure. Additional improvements can be realized in corrosion resistance, wear resistance, appearance, temperature-dependent behavior, environment stability, thermal insulation and conductivity, and acoustic insulation. Composites also afford the unique possibility of designing the material, the manufacturing procedure, and the structure in one unified and concurrent process. The large number of degrees of freedom available enables simultaneous material optimization for several given constraints, such as minimum weight, maximum dynamic stability, cost effectiveness, and so on. However, the entire process requires a reliable database of material properties standardized structural analysis method, modeling and simulation techniques, and model for materials processing. Composite laminates containing plies of two or more different types of materials are called hybrid composites and more specifically interplay hybrid composites. In some cases it may be advantageous to intermingle different types of fibers, such as glass and carbon or aramid and carbon, within the same unidirectional ply. Such composites are called intraply hybrid composites; of course one may combine intraply hybrid layers with other layers to form an intraply/interplay hybrid composite. Failure analysis of composite materials has been investigated by many researchers, a description of failure criteria’s developed in the past decades could be found in [1]. In general, failure of composite materials can be considered from microscopic or

macroscopic points of view. In the microscopic point of view failure of the composite materials is recognized due to the damage on the molecular level. This type of analysis is usually complicated and intractable, while, macroscopic behavior of composite materials can be deduced from the microscopic behavior [2]. In practice, macroscopic behavior is determined from the load-displacement data of a given test specimen, without the deep understanding of the activities at microscopic level. One important area of concentration, besides the failure load, is the mode of failure. Laminated composite may fail by fiber yielding, matrix yielding, and fiber breakage, delamination of layer or by fracture. The first three failure modes depend on the constituent's strength properties, whereas delamination is basically due to stacking sequence of different laminas. Fracture is caused by the pre-existing voids and cracks in the constituent material. Macroscopic failure criteria, which are discussed here, are based on the tensile, compressive and shear strengths of the individual lamina.

Hemelrijck et al. [3] developed a test bench for testing composite laminates under biaxial loading. In addition, a comined numerical and experimental method was obtained to determine the inplane stiffness parameters from testing a single cruciform test specimen. A full three-dimensional finite element model was used and the numerical results were validated with strain gauge, digital image correlation, and electronic speckle pattern interferometry data. Reddy and Pandey [4] developed a finite-element computational procedure based on the first-ply failure analysis of laminated composite plates where the procedure was based on the first-order shear deformation theory and a tensor polynomial failure criterion that contains the maximum stress, maximum strain,

the Hill, Tsai-Wu and Hoffman failure criteria as special cases. By using each criterion, a first-ply failure analysis of composite laminates subjected to in-plane and/or bending loads was performed. Mayes and Hansen [5] used a constituent stress-based failure criterion to construct a nonlinear progressive failure algorithm for investigating the material failure strengths of composite laminates. The proposed failure analysis was used to simulate the nonlinear laminate behavior and progressive damage of selected laminates under both uniaxial and biaxial loading. A micromechanics based theory was incorporated in their analysis in order to extract the stress and strain fields for composites constituents during a routine finite element analysis. Yang et al. [6] studied the effects of multi-axial loading of composite shafts under monotonic and fatigue conditions on its failure. They proposed a damage criterion for multi-axial monotonic loading considering the contribution of both normal and shear stresses on the plane of failure. In addition, several multi-axial fatigue failure models were proposed considering mean and cyclic normal stress and shear stress at the plane of failure, as well as the mean and cyclic normal strain and shear strain at the plane of failure and their capability for predicting the fatigue life of the composite under study. The experimental data showed an excellent agreement with the proposed model for various loading conditions. Takeda et al. [7] focused on understanding the deformation and progressive failure behavior of glass/epoxy plain weave fabric-reinforced laminates subjected to uniaxial tension at cryogenic temperatures. Cryogenic tensile tests were conducted on the woven-fabric laminates and a finite element model for progressive failure analysis of woven-fabric composite panels was also developed. The failure of the epoxy resin matrix in the

transverse fiber bundle was predicted to occur using the maximum strain failure criterion. A comparison was made between the finite element predictions and the experimental data which show good agreement.

Pipes et al. [8] have studied the hygrothermal response of laminated composite systems. A plate element is used to analyze the laminae stresses resulting from hygrothermal and mechanical loading. A six-ply graphite/epoxy laminate is considered for the analysis of hygrothermal effects. The effective moisture bending and in plane force resultants are developed and combined with thermal loads. Shen and Springer [9] have studied the effects of moisture and temperature on ultimate strength of Thornel 300/Fiberite 1034 epoxy composite. Eight-ply T300/1034 specimens have been placed in environmental chambers in which temperature and relative humidity have been controlled and kept constant. The ultimate tensile strength has been measured with material temperatures and moisture contents ranging from 200°K to 422°K and 0% to 1.5%, respectively. It was found that the ultimate strengths of 0° and 45° laminates change insignificantly due to variation of temperature and moisture. In the case of 90° laminates, the reduction in strength is as high as 60 to 90%. Upadhyay and Lyons [10] have studied the effect of hygrothermal conditions on polymer matrix composite (PMC) laminates. The hygrothermal conditions are incorporated by changing the stiffness coefficients of the laminate. Empirical relations between the moisture content and temperature level are given by Chamis [11]. Nonlinear theory is adopted in calculating the elastic deflections and the results are compared to that of a linear theory. Two types of loads, namely, in-plane and uniform transverse load are applied on these laminates. It

is found that the presence of moisture and temperature in a laminate significantly affects the deflections caused by the loads. It is also observed that the linear theory yields high differences between dry and wet results.

In new generations the driving force for technological changes has led to a new family of engineered materials and structures exhibiting multifunctional capabilities which are naturally seen in biological systems, leading to a new era of smart materials. Smart Materials and Intelligent Structures have been a matter of interest since the late 1970s, when the benefits of embedding optical fibers in composite materials were recognized [12]. The structures with surface mounted or embedded sensors and actuators that have the capability to sense and adapt to external stimuli are referred to as smart structures [13]. The feedback circuitry linking sensing and actuating is external to the sensor and actuator components; this in fact distinguishes between a smart structural systems from an intelligent structural system. Intelligent structural systems involve smart components in which the functions of sensing, feedback control, and actuating are all integrated. This type of system finds applications in aircraft wings, helicopter rotors and automobiles. One of the main motivations behind the vast attentions on smart materials and structures in recent years is its ability to incorporate active materials into the structure as sensors and actuators so that it could be used to monitor the integrity/health of the structure to enable a structure to change its shape or its material properties [14], or to control vibration [15]. These lead to improving performance and service life of the system. The research on the use of piezoelectric materials as distributed sensors and actuators for smart structural system was initiated more than forty years ago beginning

with the book by Tiersten [16] on piezoelectric plate vibration, and several other books have also appeared on the mechanics of piezoelectric and smart plates and shells [17-19].

In shape control one intends to specify the spatial distribution, or the shape, of an actuating control unit, such that the displacement field of a structure distorted from its original shape eventually vanishes, or such that the structure follows some desired field of path. The disturbances that distort the shape of structures may be transient (dynamic), or they may be slowly varying in time (quasi-/static). Shape control represents a branch of structural engineering that is closely related to control engineering. When the external disturbances as well as their effects upon the structural deformation are known in advance, the necessary control actuation may be estimated from an inverse structural analysis. Such a procedure is sometimes called a passive control strategy. When we do not know the external disturbances in advance, or when the structural properties are uncertain, yet we are able to measure some deformations; principles of automatic or active control can be utilized in order to solve the problem. Many researchers can be recognized for their unique work in shape control using piezoelectric material, Lee and Moon [20-22] have several contributions in shape control using piezoelectric layers, where these layers were developed and experimentally implemented so as to excite a specific structural mode, or to measure a specific modal content of the structural vibrations excited by external disturbances. Koconis et al. [23] investigated the changes in shapes of fiber-reinforced composite beams, plates, and shells affected by embedded piezoelectric actuators analytically. Tzou et al. [24] studied the distributed structural

control of elastic shell continua using spatially distributed modal piezoelectric actuators and some generic distributed feedback algorithms with spatial feedback functions were formulated. Finite difference modeling and shape control of piezoelectric actuator embedded elastic plates was also considered by Agrawal et al. [25], estimating optimal actuation voltages to match the deflection of the plate to a desired deflection. Several other solutions related to smart structures could be found in [26-27].

The mechanics of smart material systems involves coupling between electric, magnetic, thermal, mechanical and other effects. In addition to this coupling, it may be necessary to account for geometric and material nonlinearities. An example is the use of an electromechanical transducer that is characterized by five important properties including the resonant frequency, acoustic impedance, mechanical damping coefficient, electromechanical coupling coefficient, and the electric impedance. If nonlinear electroelastic equations are included in the model, some or all of these properties can be tuned; for instance, in an electrostrictive material, the electromechanical coupling coefficient can be tuned with a bias field [13]. In order to tune the first fundamental resonant frequency of the transducer, thin rubber layers are introduced in a multi-layer PZT laminate [28]. The thin rubber layers necessitate the use of nonlinear elastic relations, such nonlinearity in electroelastic formulations was considered by Toupin [29], also, a two-dimensional theory of electrostriction was considered by Knops [30] and solved a simplified boundary value problem using complex potentials.

1.1 Motivation

The design and analysis of composite structures, especially those that incorporate different types of active materials between the composite laminates remain of interest to researchers in many engineering disciplines. The reason is due to their outstanding mechanical performance added to their lowweight and unique and tailorable physical properties while having the ability to take corrective actions under external stimuli's such as thermal or mechanical. The past few decades have seen the development and integration of active materials into a variety of host structures as a superior means of measuring and controlling its behavior. Piezoceramics remain the most widely used "smart" or active material because they offer high actuation authority and sensing over a wide range of frequencies. Specifically, piezoceramic materials have been extensively studied and employed in aerospace structures by performing shape control. Active Fiber Composite (AFC) and Macro Fiber Composite (MFC) are types of piezoceramic material that offer structural flexibility and high actuation authority. The present study focuses on the use of several different types of piezoelectric materials on the shape control of composite laminates and observes each types ability to induce bending on the composite beam. While extensive studies on failure in laminated composites have been conducted, understanding the failure behavior of smart composite structures are limited, therefore, the failure analysis of smart composite laminates is also considered in the current study for two types of loadings conditions, uniaxial and biaxial, including hygrothermal effects of the composites laminates. Carpet plots are also provided for several different material properties which are mainly used in design aspects of

composite materials. A control methodology is also proposed that is used for feedback control using active materials where, practical simulation implementation is also provided.

1.2 Research Objective

This study focuses on the failure analysis of composite laminates under coupled mechanical, hygrothermal and electrical effects. The studied smart composite laminates follow linear thermo-electro-elastic behavior. The first-ply failure and ultimate laminate failure criteria of composite laminates are used in order to predict the failure load and mode of a composite laminate where we incorporate various commonly known macroscopic failure criteria including Tsai-Hill, Tsai Wu, Maximum stress and Maximum Strain. A detailed calculations based on the Classical Laminate Theory (CLT) is performed for Carbon/Epoxy (AS4/3501-6) laminate with stacking sequence $[90/45/-45/0]_s$ under uniaxial tensile loading. In Addition, we study the use of piezoelectric materials as actuators for shape control of composite laminates such as PZT and other piezoelectric fiber composites such as Active fiber composites (AFC) and Micrfiber composites (MFC). One of the major types of failure in smart structures is caused by debondining of the actuator from the host structure [31] which is caused by the high stress discontinuity between the interface of the host structure and the active part, by using embedded actuators, such that, the active part is incorporated into one of the layers of the composite beam during the manufacturing process, the shear stress discontinuity can be minimized while obtaining similar actuation values. Moreover, a control algorithm is proposed that enables the composite laminate to overcome the failure load

by using an active material such as AFC, MFC and PZT where, a counter electric voltage could be applied which prevents failure from occurring. The finite element software Abaqus is used to verify the present approach. Furthermore, computer software called “Hyper Composite” was developed using Action Script® and Adobe Flash® in order to perform stress and failure analysis for general composite laminates. Several carpet plots were also generated to show the interacting behavior of two independent variables such as Young’s modulus, Poisson’s ratio and shear modulus at different percentile constitutions for the laminate different plies.

1.3 Thesis Outline

In Chapter II, we begin by introducing some of the basic concepts and terminologies used in composite materials followed by the thermodynamic relations for coupling thermal, electrical and mechanical properties. In addition, we present the macromechanical stress analysis of a single lamina and laminates that are generally used in composite materials analysis based on the classical lamination theory including hygrothermal and electric effects.

Chapter III presents an overview on the types of actuators that are used in shape control of smart structures including piezoelectric fiber composites such as AFC and MFC. A detailed analytical solution for a cantilever beam based on the theory of elasticity is presented for a composite material made of two different constituents; the results were compared with solutions obtained from mechanics of materials and a finite element (FE) implemented using the commercial software Abaqus. The aim of presenting this solution is to gain strong confidence in the element type and mesh size

used in FEwhile dealing with more complex structures. The effect of using several different types of actuators on the behavior of a composite laminate are also studied and compared with each other in order to observe their power to bend the plate enough to counteract any type of external stimuli such as thermal or mechanical deformations.

Chapter IV presents the failure analysis of composite laminates including hygrothermal and electric effects using the first-ply failure and ultimate laminate failure criteria of composite laminates to predict the failure load and mode of a composite laminate under a uniaxial tensile load where various commonly known macroscopic failure criteria were used including Tsai-Hill, Tsai Wu, Maximum stress and Maximum Strain.

Chapter V introduces the computer software “Hyper Composite” and compares its results with those previously obtained in Chapter IV; moreover, the results are compared with available experimental results in the literature. A failure control algorithm is proposed based on the results obtained from the first ply failure analysis where these results are used to attain a recommended voltage value which can be actuated through the active parts of the composite laminate to prevent failure from occurring. A practical control circuit is also proposed and implemented through the simulation software PROTEOUS where we use a microcontroller as the smart part that is activated when the stress value exceeds that of failure.

Chapter VI presents discussion and future work.

CHAPTER II

LINEAR RESPONSE OF SMART COMPOSITES WITH COUPLED MECHANICAL AND NON-MECHANICAL EFFECTS

In this chapter, we start by introducing some basic concepts and terminologies that are used in linear analysis of smart composite materials. Thermodynamic relations for coupling thermal, electrical and mechanical properties are presented in section one. The macromechanical stress analysis of a single lamina and laminates that are generally used in composite materials based on the classical lamination theory including both hygrothemal and electric effects are presented in section three.

2.1 Thermodynamic Relations for Coupling Thermal, Electrical and Mechanical Properties

One of the important aspects when dealing with materials is the coupling effects induced by several different types of external stimuli that affect the overall behavior of the material, for example, electric charge in a polar material may be induced by an external electric field, or by a stress through the piezoelectric effect, and by a temperature change through the pyroelectric effect, similarly, the mechanical strain in a piezoelectric material may be induced by an electric field through the converse piezoelectric effect or by an external stress and also by a temperature change, due to the thermal expansion of the material. This coupling of different effects places important experimental constraints on property measurements. Assume, for example, that an electric field is applied on a piezoelectric material under constant temperature conditions. If the sample is mechanically free to change its dimensions, the resulting

strain is due to the pure piezoelectric effect, while if the sample is partially clamped for example a thin film deposited on a thick substrate, the resulting stress will be a contribution of the piezoelectric strain and the mechanical strain due to clamping conditions. The coupling between the thermal, elastic and electrical parameters of a material can be introduced using the thermodynamic approach which gives relations between materials parameters measured under different experimental conditions. These relations are essential for modeling and understanding the response of piezoelectric and pyroelectric devices.

It is well known from the first law of thermodynamics that the reversible change dU in the internal energy U of an elastic dielectric that is subjected to a small change of the strain d$\boldsymbol{\varepsilon}$, electric displacement d$\mathbf{D}$, and entropy dη is given by

$$dU = Td\eta + \sigma_{ij}\varepsilon_{ij} + \xi_i dD_i \tag{2.1}$$

where T is the temperature of the material, D_i is the scalar component of the dielectric displacement vector, η is the specific entropy and ξ_i is the scalar component of the electric field vector. A Legendre transformation of U is performed in order to express the thermodynamic function in terms of other independent variables. Experimental tests are often done under isothermal conditions, and electric field and stress are usually applied, therefore, it is useful to pick the following (T, $\boldsymbol{\sigma}$, $\boldsymbol{\xi}$) as independent variables. This is done by adding the expression ($-T\,\eta - \boldsymbol{\sigma\varepsilon} - \boldsymbol{\xi}\mathbf{D}$) to U resulting in the following free energy function which is known as the Gibbs free energy

$$G = U - T\eta - \sigma_{ij}\varepsilon_{ij} - \xi_i D_i \tag{2.2}$$

The differential of G gives together with Eq. (2.1)

$$dG = -\eta dT - \varepsilon_{ij} d\sigma_{ij} - D_i d\xi_i \tag{2.3}$$

From Eq. (2.3) one obtains

$$\eta = -\left(\frac{\partial G}{\partial T}\right)_{\sigma,\,\xi} \qquad \sigma_{ij} = -\left(\frac{\partial G}{\partial \sigma_{ij}}\right)_{T,\xi} \qquad D_i = -\left(\frac{\partial G}{\partial \xi_i}\right)_{\sigma,T} \tag{2.4}$$

where the subscripts indicate variables that are kept constant. The total differentials of η, $\boldsymbol{\sigma}$ and $\mathbf{D}$ can be written as

$$\begin{aligned} d\eta &= \left(\frac{\partial \eta}{\partial T}\right)_{\sigma,\xi} dT + \left(\frac{\partial \eta}{\partial \sigma_{ij}}\right)_{T,\xi} d\sigma_{ij} + \left(\frac{\partial \eta}{\partial \xi_i}\right)_{T,\sigma} d\xi_i \\ d\sigma_{ij} &= \left(\frac{\partial \sigma_{ij}}{\partial T}\right)_{\sigma,\xi} dT + \left(\frac{\partial \sigma_{ij}}{\partial \sigma_{kl}}\right)_{T,\xi} d\sigma_{kl} + \left(\frac{\partial \sigma_{ij}}{\partial \xi_k}\right)_{T,\sigma} d\xi_k \\ dD_i &= \left(\frac{\partial D_i}{\partial T}\right)_{\sigma,\xi} dT + \left(\frac{\partial D_i}{\partial \sigma_{jk}}\right)_{T,\xi} d\sigma_{jk} + \left(\frac{\partial D_i}{\partial \xi_j}\right)_{T,\sigma} d\xi_j \end{aligned} \tag{2.5}$$

Each of the partial derivatives in Eq. (2.5) identifies a physical effect which is defined as the heat capacity, piezoelectric effect, electrocaloric effect, thermal expansion, elastic compliance, converse piezoelectricity, pyroelectric effect, direct piezoelectricity, and dielectric permittivity respectively [32]. To simplify notation, the elastic compliance and piezoelectric coefficient tensors may be written in the matrix or

reduced notation form, following the Voigt convention where a pair of indices *ii* = 11; 22; 33 is, for example, replaced with the single index *m* = 1; 2; 3, respectively, and the mixed pairs of indices (which represent shear components of strain and stress tensors) *ij* = 23 or 32, 13 or 31, 12 or 21 are written as *m* = 4; 5; 6, respectively. From here, the linear piezoelectric constitutive equations can be expressed as

$$\begin{aligned} \varepsilon_m &= S_{mn}^{T,\xi}\sigma_n + d_{im}^{T,\sigma}\xi_i + \alpha_m \Delta T \\ D_i &= d_{im}^{T,\xi}\sigma_m + \omega_{ij}^{T,\sigma}\xi_j + p_i \Delta T \end{aligned} \tag{2.6}$$

where **α** is the thermal expansion tensor, **d** is the piezoelectric strain coefficient tensor, **S** is the compliance tensor, **p** is the pyroelectric vector and **ω** is the permittivity tensor. This constitutive model only includes linear effects. In the case of strong fields or strongly nonlinear material response, these relations can be extended to include higher-order terms [32].

2.2 Terminologies and Definitions

2.2.1 Classification of General Composites

Composites are distinguished by the spatial arrangement of the material phases. To be a composite at least two such phases need to occur where the matrix phase surrounds and connects one or more inclusion phases. Composites can be classified according to the diverse shapes of inclusions that may be used such as particulate, fibrous, and lamellar topologies as shown in Figure 2.1. Composites can also be represented through a combination of these inclusion types. In steel concrete, for example, mineral particles and metal fibers are joined by a binder material, in aerospace applications; the combination of glass fibers and aluminum laminae are used in several

components of the aircraft structure such as the wing and fuselage, one famous example on their use in aircraft industry is the Boeing 787 in which 50% of the whole structure is made out of composite materials. The listed types of inclusions may be further categorized with respect to their geometry and relative arrangement. In the case of fibrous inclusions, there are continuous or discontinuous fibers of straight or curled shape in a regular or irregular layout as shown in Figure 2.2. More complicated fiber structures arise when textile techniques like stitching, braiding, or knitting are involved.

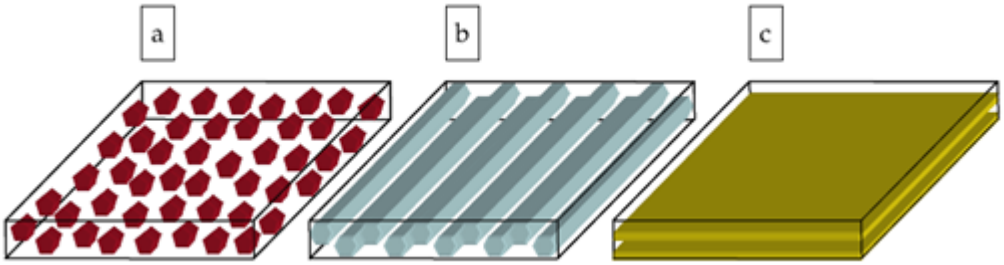

Figure 2.1: Classifications of Composites: a) Particulate b) Fibourus c) Lamellar

2.2.2 Lamina and Laminate

A lamina, or ply, is a plane (or curved) layer of unidirectional fibers or woven fabric in a matrix. In the case of unidirectional fibers, it is also referred to as unidirectional lamina (UD). The lamina is an orthotropic material with principal material axes in the direction of the fibers (longitudinal), normal to the fibers in the plane of the lamina (in-plane transverse), and normal to

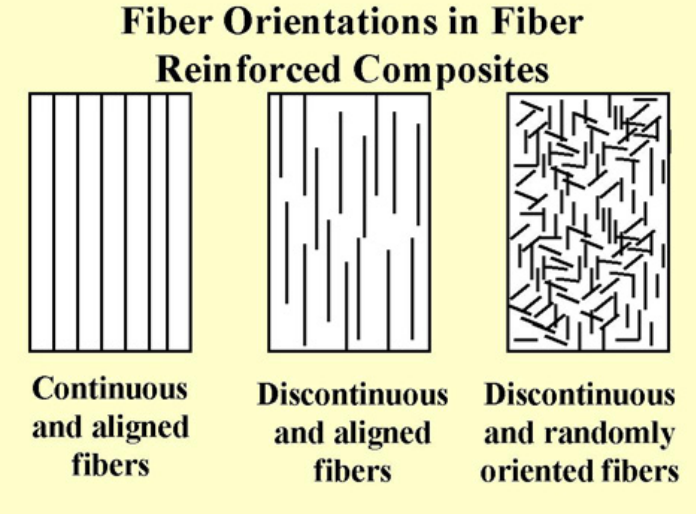

Figure 2.2: Fiber orientation in fiber reinforced composites

the plane of lamina. These principal axes are designated as 1, 2, and 3, respectively. In the case of woven fabric composites, the warp and the fill directions are in-plane 1 and 2 principal directions, respectively.

A laminate is made up of two or more unidirectional laminae or plies stacked together at various orientations. The laminae (or plies, or layers) can be of various thicknesses and consist of different materials. Since the orientation of the principal material axes varies from ply to ply, it is more convenient to analyze laminates using common fixed system or coordinates (x_1, x_2, x_3). The orientation of a given ply is given by the angle between the reference x-axis and the major principal material axis (fiber orientation or warp direction) of the ply, measured in a counterclockwise direction on the x_1-x_2 plane.

2.2.3 Anisotropy-Orthotropy-Isotropy

Many material properties, such as stiffness, strength, thermal expansion, thermal conductivity, and permeability are associated with a direction or axis (vectorial or tensorial quantities). A material is anisotropic when its properties at a point vary with direction or depend on the orientation of reference axes. If the properties of the material along any direction are the same as those along symmetric direction with respect to a plane, then that plane is defined as a plane of material symmetry. A material may have zero, one, two, three, or an infinite number of planes of material symmetry through a point. A material without any planes of symmetry is called general anisotropic (or aeolotropic). At the other extreme, an isotropic material has an infinite number of planes of symmetry where its properties are the same in all directions or are independent of the orientation of reference axes. Of special relevance to composite material are orthotropic materials, that is, materials having at least three mutually perpendicular planes of symmetry. The intersections of these planes define three mutually perpendicular axes, called principal axes of material symmetry or simply principal material axes. The concept of isotropy/anisotropy is also associated with a scale or characteristic volume. For example, the composite material is considered homogeneous and anisotropic on a macroscopic scale with regards to its mechanical and non-mechanical response. On a microscopic scale, the material is heterogeneous (when its properties vary from point to point, or depend on location).

2.3 Macromechanical Analysis of a Single Lamina

As mentioned previously in Chapter II, the difference between a lamina and a laminate, where a lamina is a thin layer of a composite material that is generally of a thickness on the order of 0.005 in. (0.125 mm), and a laminate is constructed by stacking a number of such lamina in the direction of the lamina thickness. Mechanical structures made of these laminates are subjected to various loads, such as bending and twisting. The design and analysis of such laminated structures demands knowledge of the stresses and strains in the laminate. Understanding the mechanical analysis of a lamina precedes understanding that of a laminate. If the lamina is made of homogeneous fibers and an isotropic homogeneous matrix, the stiffness of the lamina varies from point to point depending on whether the point is in the fiber, the matrix, or the fiber–matrix interface. Accounting for these variations will make any kind of mechanical modeling of the lamina very complicated. For this reason, the macromechanical analysis of a lamina is based on average properties and considering the lamina to be homogeneous with regards to its thermo-electro-mechanical properties.

2.3.1 Stress-Strain Relations

The state of stress can be represented by nine stress components, σ_{ij} (where i, j = 1, 2, 3) acting on the sides of an element cube as shown in Figure 2.3 Similarly, the state of deformation is represented by nine strain components, ε_{ij}.

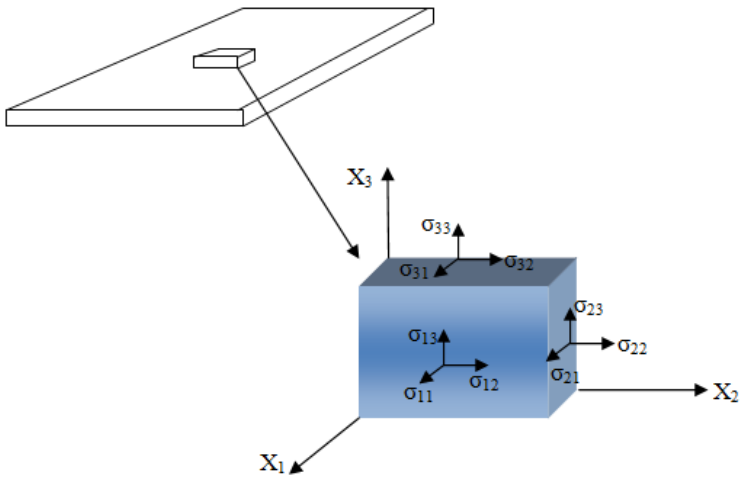

Figure 2.3: Lamina under state of plane stress

Imposing symmetry of the stress and strain tensors obtained from the conservation of angular momentum

$$\begin{aligned} \sigma_{ij} &= \sigma_{ji} \quad (i, j = 1, 2, 3) \\ \varepsilon_{ij} &= \varepsilon_{ji} \end{aligned} \tag{2.7}$$

Thus the stress-strain relation for anisotropic body is given as follows for a three-dimensional body in a 1–2–3 orthogonal Cartesian coordinate system

$$\begin{bmatrix} \sigma_1 \\ \sigma_2 \\ \sigma_3 \\ \tau_4 \\ \tau_5 \\ \tau_6 \end{bmatrix} = \begin{bmatrix} C_{11} & C_{12} & C_{13} & C_{14} & C_{15} & C_{16} \\ C_{21} & C_{22} & C_{23} & C_{24} & C_{25} & C_{26} \\ C_{31} & C_{32} & C_{33} & C_{34} & C_{35} & C_{36} \\ C_{41} & C_{42} & C_{43} & C_{44} & C_{45} & C_{46} \\ C_{51} & C_{52} & C_{53} & C_{54} & C_{55} & C_{56} \\ C_{61} & C_{62} & C_{63} & C_{64} & C_{65} & C_{66} \end{bmatrix} \begin{bmatrix} \varepsilon_1 \\ \varepsilon_2 \\ \varepsilon_3 \\ \gamma_4 \\ \gamma_5 \\ \gamma_6 \end{bmatrix} \tag{2.8}$$

where the 6 x 6 [C] matrix is called the stiffness matrix and contains 36 constants. They also can be written in indicial notation as follows

$$\begin{aligned} \sigma_i &= C_{ij}\varepsilon_j, \ (\text{where i, } j = 1,2,3,\ldots,6) \\ \varepsilon_i &= S_{ij}\sigma_j \end{aligned} \tag{2.9}$$

- Orthotropic Material

An Orthotropic material as defined previously is a material which has three mutually perpendicular planes of material symmetry. The stress-strain relation have the same form as anisotropic material, however, the number of independent elastic constants are reduced to nine, because the stiffness and the compliance terms are interrelated.

$$\begin{bmatrix} \sigma_1 \\ \sigma_2 \\ \sigma_3 \\ \tau_4 \\ \tau_5 \\ \tau_6 \end{bmatrix} = \begin{bmatrix} C_{11} & C_{12} & C_{13} & 0 & 0 & 0 \\ C_{21} & C_{22} & C_{23} & 0 & 0 & 0 \\ C_{31} & C_{32} & C_{33} & 0 & 0 & 0 \\ 0 & 0 & 0 & C_{44} & 0 & 0 \\ 0 & 0 & 0 & 0 & C_{55} & 0 \\ 0 & 0 & 0 & 0 & 0 & C_{66} \end{bmatrix} \begin{bmatrix} \varepsilon_1 \\ \varepsilon_2 \\ \varepsilon_3 \\ \gamma_4 \\ \gamma_5 \\ \gamma_6 \end{bmatrix} \tag{2.10}$$

- Transversely Isotropic Material

An orthotropic material is called a transversely isotropic when one of its principal planes is a plane of isotropy, that is at every point there is a plane on which the mechanical properties are the same in all directions. The stress-train relations for a transversely isotropic material are simplified for a two-three planes of isotropy such that

$$\begin{aligned} C_{12} &= C_{13} \\ C_{22} &= C_{33} \\ C_{55} &= C_{66} \end{aligned} \tag{2.11}$$

Thus, the stress-strain relations for a transversely isotropic material are reduced to

$$\begin{bmatrix}\sigma_1\\ \sigma_2\\ \sigma_3\\ \tau_4\\ \tau_5\\ \tau_6\end{bmatrix}=\begin{bmatrix}C_{11} & C_{12} & C_{12} & 0 & 0 & 0\\ C_{12} & C_{22} & C_{23} & 0 & 0 & 0\\ C_{12} & C_{23} & C_{22} & 0 & 0 & 0\\ 0 & 0 & 0 & \frac{C_{22}-C_{23}}{2} & 0 & 0\\ 0 & 0 & 0 & 0 & C_{55} & 0\\ 0 & 0 & 0 & 0 & 0 & C_{55}\end{bmatrix}\begin{bmatrix}\varepsilon_1\\ \varepsilon_2\\ \varepsilon_3\\ \gamma_4\\ \gamma_5\\ \gamma_6\end{bmatrix} \tag{2.12}$$

The relations above show that in orthotropic material with transversely isotropy are characterized by only five independent elastic constants.

- Isotropic Material

An isotropic material is characterized by an infinite number of planes of material symmetry through a point. For such a material, subscript 1, 2, and 3 in the material constants are interchangeable, thus the stress-train relations are reduced to

$$\begin{bmatrix}\sigma_1\\ \sigma_2\\ \sigma_3\\ \tau_4\\ \tau_5\\ \tau_6\end{bmatrix}=\begin{bmatrix}C_{11} & C_{12} & C_{12} & 0 & 0 & 0\\ C_{12} & C_{11} & C_{12} & 0 & 0 & 0\\ C_{12} & C_{12} & C_{11} & 0 & 0 & 0\\ 0 & 0 & 0 & \frac{C_{11}-C_{12}}{2} & 0 & 0\\ 0 & 0 & 0 & 0 & \frac{C_{11}-C_{12}}{2} & 0\\ 0 & 0 & 0 & 0 & 0 & \frac{C_{11}-C_{12}}{2}\end{bmatrix}\begin{bmatrix}\varepsilon_1\\ \varepsilon_2\\ \varepsilon_3\\ \gamma_4\\ \gamma_5\\ \gamma_6\end{bmatrix} \tag{2.13}$$

So, an isotropic material is fully characterized by only two independent constants, the stiffnesses C_{11} and C_{12}. We summarize the number of independent elastic constants for various types of materials

• *Anisotropic*: 36

• *Orthotropic*: 9

• *Transversely Isotropic*: 5

• *Isotropic*: 2

2.3.2 Constitutive Relations for a Thin Lamina

In so structural applications, composites materials are used in the form of thin laminates loaded in the plane of the laminate. Thus, composite laminae and laminates can be considered to be under a condition of plane stress with all stress components in the out–of-plane direction being zero that is

$$\begin{aligned} \sigma_3 &= 0 \\ \tau_4 &= 0 \\ \tau_5 &= 0 \end{aligned} \tag{2.14}$$

This results in the following hygrothermoelectroelastic (It is assumed that the moisture concentration has a similar effect as expansion/contraction due to temperature changes. In practice, moisture concentration can cause swelling in the constituents, affecting the thermo-electro-elastic properties of the composite and its effect is often unrecoverable. Likewise, temperature changes can alter the properties of materials) constitutive equation for the k^{th} layer that is characterized as an orthotropic layer including piezoelectric effect

$$\begin{bmatrix} \sigma_1 \\ \sigma_2 \\ \sigma_6 \end{bmatrix}_k = \begin{bmatrix} Q_{11} & Q_{12} & 0 \\ Q_{12} & Q_{22} & 0 \\ 0 & 0 & Q_{66} \end{bmatrix}_k \left\{ \begin{bmatrix} \varepsilon_1 \\ \varepsilon_2 \\ \varepsilon_6 \end{bmatrix} - \begin{bmatrix} \alpha_1 \\ \alpha_2 \\ \alpha_6 \end{bmatrix}_k \Delta T - \begin{bmatrix} \beta_1 \\ \beta_2 \\ \beta_6 \end{bmatrix}_k \Delta C \right\} - \begin{bmatrix} 0 & 0 & e_{31} \\ 0 & 0 & e_{32} \\ 0 & 0 & 0 \end{bmatrix}_k \begin{bmatrix} \xi_1 \\ \xi_2 \\ \xi_3 \end{bmatrix}_k \tag{2.15}$$

$$\begin{bmatrix} D_1 \\ D_2 \\ D_3 \end{bmatrix}_k = \begin{bmatrix} 0 & 0 & 0 & e_{15} & 0 \\ 0 & 0 & e_{24} & 0 & 0 \\ e_{31} & e_{32} & 0 & 0 & 0 \end{bmatrix}_k \begin{bmatrix} \varepsilon_1 \\ \varepsilon_2 \\ \varepsilon_4 \\ \varepsilon_5 \\ \varepsilon_6 \end{bmatrix} + \begin{bmatrix} \omega_{11} & 0 & 0 \\ 0 & \omega_{22} & 0 \\ 0 & 0 & \omega_{33} \end{bmatrix}_k \begin{bmatrix} \xi_1 \\ \xi_2 \\ \xi_3 \end{bmatrix}_k \tag{2.16}$$

where Q_{ij} are the components of the plane stress-reduced stiffnesses, e_{ij} are the componenets of the piezoelectric constants, ω_{ij} are the dielectric constants of the k_{th} lamina in its material coordinate system. σ_i, ε_i, ξ_i, D_i are the stress, strain, electric field and electric displacement scalar components, respectively, referred to the material coordinate system (x_1, x_2, x_3). α_{ij}, β_{ij} are the scalar coefficients of thermal and moisture expansion, respectively, in the x_1, x_2 direction. ΔT and ΔC are the temperature and moisture changes from a reference state. The coefficients $Q_{(k)ij}$ are known in terms of the engineering constants of the k^{th} layer as follows

$$\begin{aligned} Q_{11} &= \frac{E_1}{1-\nu_{21}\nu_{12}} \\ Q_{12} &= \frac{\nu_{12}E_2}{1-\nu_{21}\nu_{12}} \\ Q_{22} &= \frac{E_2}{1-\nu_{21}\nu_{12}} \\ Q_{66} &= G_{12} \end{aligned} \tag{2.17}$$

Thus, a single orthotropic lamina can be fully characterized by four independent constants through any of the following combinations

$$Q_{11},\ Q_{12}, Q_{22}, Q_{66}, \text{ or}$$
$$S_{11}, S_{12}, S_{22}, S_{66}, \text{ or}$$

$$E_1, E_2, \nu_{12}, G_{12}$$

Poisson's ratio ν_{21} is not independent due to imposing symmetry conditions for the stiffness and compliance matrices as it is related to ν_{12}, E_1 and E_2 by

$$\frac{\nu_{12}}{E_1} = \frac{\nu_{21}}{E_2} \tag{2.18}$$

The stress based piezoelectric constants are known in terms of the strain based piezoelectric constants and elastic stiffnesses as

$$\begin{bmatrix} 0 & 0 & e_{13} \\ 0 & 0 & e_{23} \\ 0 & 0 & 0 \end{bmatrix}_k = \begin{bmatrix} 0 & 0 & d_{13} \\ 0 & 0 & d_{23} \\ 0 & 0 & 0 \end{bmatrix}_k \begin{bmatrix} Q_{11} & Q_{12} & 0 \\ Q_{12} & Q_{22} & 0 \\ 0 & 0 & Q_{66} \end{bmatrix}_k \tag{2.19}$$

2.3.3 Transformation of the Constitutive Relation

Generally, a laminate does not consist only of unidirectional laminae because of their low stiffness and strength properties in the transverse direction. Therefore, in most laminates, some laminae are placed at an angle. Thus it is necessary to develop the stress–strain relationship for an angle lamina.

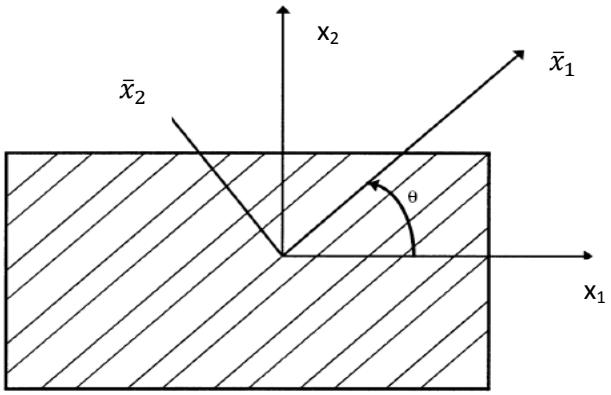

Figure 2.4: Local and global axes of a single lamina

Figure 2.4 shows us the coordinate system used for angle lamina. The stress and strain components referred to the principle material axes (x_1, x_2) can be expressed in terms of those refereed to the loading axes ($\bar{x}_1, \bar{x}_2$)by the following transformation relations

$$\begin{bmatrix} \bar{\sigma}_1 \\ \bar{\sigma}_2 \\ \bar{\sigma}_6 \end{bmatrix} = [T]^{-1} \begin{bmatrix} \sigma_1 \\ \sigma_2 \\ \sigma_6 \end{bmatrix}$$
$$\begin{bmatrix} \varepsilon_1 \\ \varepsilon_2 \\ 0.5\times\gamma_6 \end{bmatrix} = [T] \begin{bmatrix} \bar{\varepsilon}_1 \\ \bar{\varepsilon}_2 \\ 0.5\times\bar{\gamma}_6 \end{bmatrix} \qquad (2.20)$$

where [T] is called the transformation matrix and is defined as

$$[T]=\begin{bmatrix} c^2 & s^2 & 2sc \\ s^2 & c^2 & -2sc \\ -sc & sc & c^2-s^2 \end{bmatrix}$$

$$[T]^{-1}=\begin{bmatrix} c^2 & s^2 & -2sc \\ s^2 & c^2 & 2sc \\ sc & -sc & c^2-s^2 \end{bmatrix} \tag{2.21}$$

$$c = cos(\theta)$$

$$s = sin(\theta) \tag{2.22}$$

when the lamina is loaded only in the tension or compression along the principle material axes, there is no shear strain in the principle direction. Similarly, when the lamina is loaded under pure shear on the principle plane (1, 2), only a shear strain is produced on the 1, 2 plane. Thus, there is no coupling between normal stresses and shear deformation and between shear stress and normal strain. This is not the case when the lamina is loaded along arbitrary axes, then the stress-strain relation take the form

$$\begin{bmatrix} \bar{\sigma}_1 \\ \bar{\sigma}_2 \\ \bar{\sigma}_6 \end{bmatrix}_k = \begin{bmatrix} \bar{Q}_{11} & \bar{Q}_{12} & \bar{Q}_{16} \\ \bar{Q}_{12} & \bar{Q}_{22} & \bar{Q}_{23} \\ \bar{Q}_{16} & \bar{Q}_{26} & \bar{Q}_{66} \end{bmatrix}_k \left\{ \begin{bmatrix} \bar{\varepsilon}_1 \\ \bar{\varepsilon}_2 \\ \bar{\gamma}_6 \end{bmatrix} - \begin{bmatrix} \bar{\alpha}_1 \\ \bar{\alpha}_2 \\ \bar{\alpha}_6 \end{bmatrix}_k \Delta T - \begin{bmatrix} \bar{\beta}_1 \\ \bar{\beta}_2 \\ \bar{\beta}_6 \end{bmatrix}_k \Delta C \right\} - \begin{bmatrix} 0 & 0 & \bar{e}_{31} \\ 0 & 0 & \bar{e}_{32} \\ 0 & 0 & \bar{e}_{36} \end{bmatrix}_k \begin{bmatrix} \bar{\xi}_1 \\ \bar{\xi}_2 \\ \bar{\xi}_3 \end{bmatrix}_k \tag{2.23}$$

$$\begin{bmatrix} \bar{D}_1 \\ \bar{D}_2 \\ \bar{D}_3 \end{bmatrix}_k = \begin{bmatrix} 0 & 0 & \bar{e}_{14} & \bar{e}_{15} & 0 \\ 0 & 0 & \bar{e}_{24} & \bar{e}_{25} & 0 \\ \bar{e}_{31} & \bar{e}_{32} & 0 & 0 & \bar{e}_{36} \end{bmatrix}_k \begin{bmatrix} \bar{\varepsilon}_1 \\ \bar{\varepsilon}_2 \\ \bar{\gamma}_4 \\ \bar{\gamma}_5 \\ \bar{\gamma}_6 \end{bmatrix} + \begin{bmatrix} \bar{\omega}_{11} & 0 & 0 \\ 0 & \bar{\omega}_{22} & 0 \\ 0 & 0 & \bar{\omega}_{33} \end{bmatrix}_k \begin{bmatrix} \bar{\xi}_1 \\ \bar{\xi}_2 \\ \bar{\xi}_3 \end{bmatrix}_k \tag{2.24}$$

where $\overline{Q}_{ij}$ are called the elements of the transformed reduced stiffness matrix Q_{ij} and are given by

$$\begin{aligned}
\overline{Q}_{11} &= Q_{11}c^4 + Q_{22}s^4 + 2(Q_{12} + 2Q_{66})s^2c^2 \\
\overline{Q}_{12} &= \left(Q_{11} + Q_{22} - 4Q_{66}\right)s^2c^2 + Q_{12}(c^4 + s^2) \\
\overline{Q}_{22} &= Q_{11}s^4 + Q_{22}c^4 + 2(Q_{12} + 2Q_{66})s^2c^2 \\
\overline{Q}_{16} &= \left(Q_{11} - Q_{12} - 2Q_{66}\right)c^3s - \left(Q_{22} - Q_{12} - 2Q_{66}\right)s^3c \\
\overline{Q}_{26} &= \left(Q_{11} - Q_{12} - 2Q_{66}\right)cs^3 - \left(Q_{22} - Q_{12} - 2Q_{66}\right)c^3s \\
\overline{Q}_{66} &= \left(Q_{11} + Q_{22} - 2Q_{12} - 2Q_{66}\right)s^2c^2 + Q_{66}(s^4 + c^4)
\end{aligned} \tag{2.25}$$

The transformed thermal and moisture coefficients of expansion are defined as follows

$$\begin{aligned}
\overline{\alpha}_1 &= \alpha_1c^2 + \alpha_2s^2 \\
\overline{\alpha}_2 &= \alpha_1s^2 + \alpha_2c^2 \\
\overline{\alpha}_6 &= 2(\alpha_1 - \alpha_2)sc \\
\overline{\beta}_1 &= \beta_1c^2 + \beta_2s^2 \\
\overline{\beta}_2 &= \beta_1s^2 + \beta_2c^2 \\
\overline{\beta}_6 &= 2(\beta_1 - \beta_2)sc
\end{aligned} \tag{2.26}$$

Also, the transformed piezoelectric moduli are defined as

$$
\begin{aligned}
\overline{e}_{31} &= e_{31}c^2 + e_{32}s^2 \\
\overline{e}_{32} &= e_{31}s^2 + e_{32}c^2 \\
\overline{e}_{33} &= e_{33} \\
\overline{e}_{36} &= (e_{31} - e_{32})sc \\
\overline{e}_{14} &= (e_{15} - e_{24})sc \\
\overline{e}_{24} &= e_{24}c^2 + e_{15}s^2 \\
\overline{e}_{15} &= e_{15}c^2 + e_{24}s^2 \\
\overline{e}_{25} &= (e_{15} - e_{24})sc
\end{aligned}
\tag{2.27}
$$

And the transformed dielectric coefficient are defined as

$$
\begin{aligned}
\overline{\omega}_{11} &= \omega_{11}c^2 + \omega_{22}s^2 \\
\overline{\omega}_{22} &= \omega_{11}s^2 + \omega_{22}c^2 \\
\overline{\omega}_{12} &= (\omega_{11} - \omega_{22})sc
\end{aligned}
\tag{2.28}
$$

2.4 Macromechanical Analysis of a Laminate

It is apparent that the overall behavior of a multidirectional laminate is a function of the properties and stacking sequence of the individual layers. The so-called classical lamination theory predicts the behavior of the laminate within the framework of the following assumptions and restrictions:

- Each layer (lamina) of the laminate is quasi –homogenous and orthotropic
- The laminate is thin with its lateral dimensions much larger than its thickness and is loaded in its plane only, that is, the laminate and its layers (except for their edges) are in a state of plane stress ($\sigma_3 = \tau_4 = \tau_5 = 0$)

- All displacements are small compared with the thickness of the laminate (u, v, $w << h$)
- Displacements are continuous throughout the laminate
- In-plane displacements vary linearly through the thickness of the laminate, that is, u and v displacements in the x_1-x_2 directions are linear functions of x_3
- Straight lines normal to the middle surface remain straight and normal to that surface after deformation. This implies that transverse shear strains γ_4 and γ_5 are zero
- Strain-displacement and stress-strain relations are linear.

Normal distances from the middle surface remain constant, that is, the transverse normal strain ε_3 is zero. This implies that the transverse displacement w is independent of the thickness coordinate x_3. Figure 2.5 shows two cross sections before and after loading, we can observe the deformation that has occurred after loading. Assume u_0, v_0, and w_0 to be displacements in the x_1, x_2, and x_3 directions, respectively, at the midplane and u, v, and w are the displacements at any point in the x_1, x_2, and x_3 directions, respectively. At any point other than the midplane, the two displacements in the x_1–x_2 plane will depend on the axial location of the point and the slope of the laminate midplane with the x_1 and x_2 directions. In formulating the theory, it is assumed that the layers are perfectly bonded together. Further, restrict the formulation to linear elastic material behavior, small strains and displacements, and to the case in which the temperature and electric fields are given. The Kirchhoff hypothesis leads to the displacement field

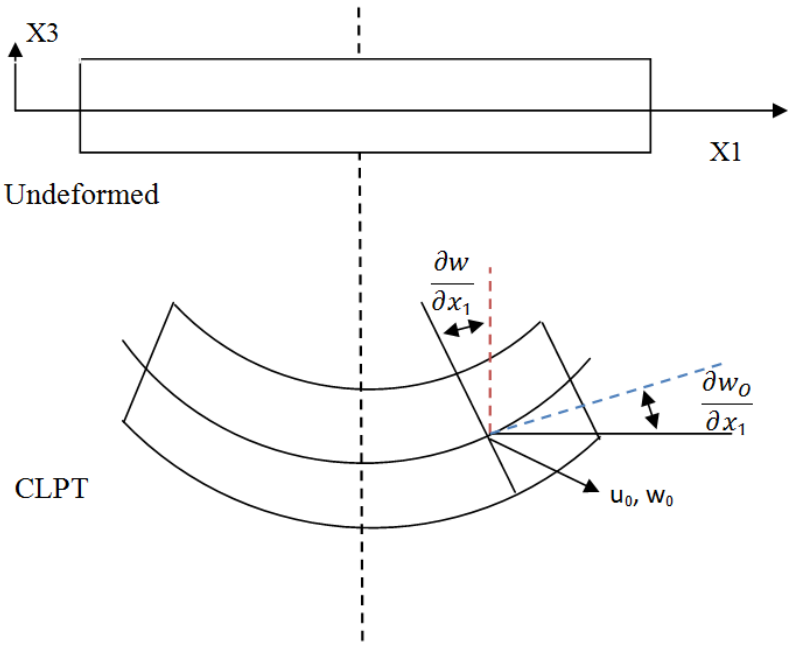

Figure 2.5: Kinematics of deformation of a plate edge for CLP

$$u(x_1, x_2, x_3, t) = u_0(x_1, x_2, x_3, t) - z\frac{\partial w_0}{\partial x} \tag{2.29}$$

$$v(x_1, x_2, x_3, t) = v_0(x_1, x_2, x_3, t) - z\frac{\partial w_0}{\partial x_2} \tag{2.30}$$

$$w(x_1, x_2, x_3, t) = w_0(x_1, x_2, x_3, t) \tag{2.31}$$

The nonzero strains associated with the displacement field in Eq. (2.30-2.32) are given by

$$\begin{Bmatrix} \varepsilon_1 \\ \varepsilon_2 \\ \gamma_6 \end{Bmatrix} = \begin{Bmatrix} \varepsilon_1^0 \\ \varepsilon_2^0 \\ \gamma_6^0 \end{Bmatrix} + z\begin{Bmatrix} \varepsilon_1^1 \\ \varepsilon_2^1 \\ \gamma_6^1 \end{Bmatrix} \tag{2.32}$$

$$\begin{Bmatrix} \varepsilon_1^0 \\ \varepsilon_2^0 \\ \gamma_6^0 \end{Bmatrix} = \begin{Bmatrix} \dfrac{\partial u_0}{\partial x_1} + \dfrac{1}{2}\left(\dfrac{\partial w_0}{\partial x_1}\right)^2 \\ \dfrac{\partial v_0}{\partial x_2} + \dfrac{1}{2}\left(\dfrac{\partial w_0}{\partial x_2}\right)^2 \\ \dfrac{\partial u_0}{\partial x_2} + \dfrac{\partial v_0}{\partial x_1} + \dfrac{\partial w_0}{\partial x_1}\dfrac{\partial w_0}{\partial x_2} \end{Bmatrix} \tag{2.33}$$

$$\begin{Bmatrix} \varepsilon_1^1 \\ \varepsilon_2^1 \\ \gamma_6^1 \end{Bmatrix} = \begin{Bmatrix} -\dfrac{\partial^2 w_0}{\partial x_1{}^2} \\ -\dfrac{\partial^2 w_0}{\partial x_2{}^2} \\ -2\dfrac{\partial^2 w_0}{\partial x_1 \partial x_2} \end{Bmatrix} \tag{2.34}$$

where $\varepsilon_1^0, \varepsilon_2^0, \gamma_6^0$ are the membrane strains and $\varepsilon_1, \varepsilon_2, \gamma_6$ are the flexural (bending) strains. The transverse strains $\varepsilon_4\ \varepsilon_5\ \varepsilon_3$ are zero in the classical plate theory (for thin structural materials). Note from Eq. (2.32) that all strain components vary linearly through the laminate thickness, and they are independent of the material variations through the laminate thickness while the stresses discontinuity from lamina to lamina as shown in Figure 2.6.

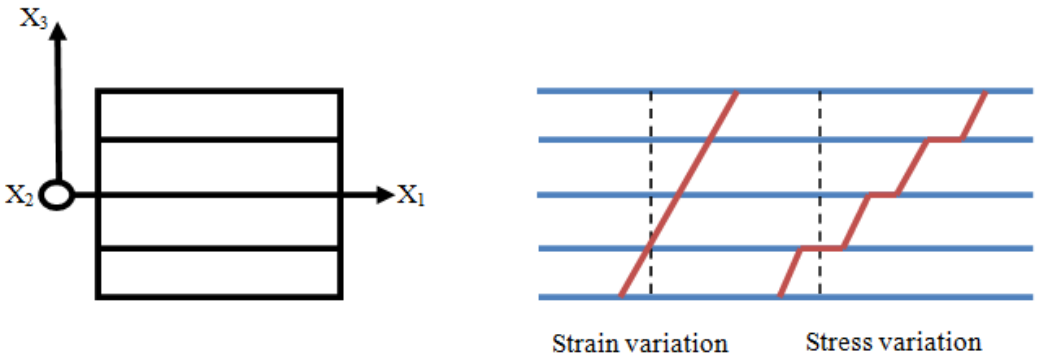

Figure 2.6: Illistration of linear strain and stress variation in a composite laminate

Because of the discontinuous variation of stresses from layer to layer, it is more convenient to deal with the integrated effect of these stresses on the laminate. Thus, we seek expressions relating forces and moments to laminate deformation. The stresses acting on a layer k of a laminate given by Eq. (2.15) can be replaced by resultant forces and moments. Consider a laminate made of *n* plies as shown in Figure 2.7 where each ply has a thickness of t_k. Then the thickness of the laminate h is given as

$$h = \sum_{k=1}^{n} t_k \tag{2.35}$$

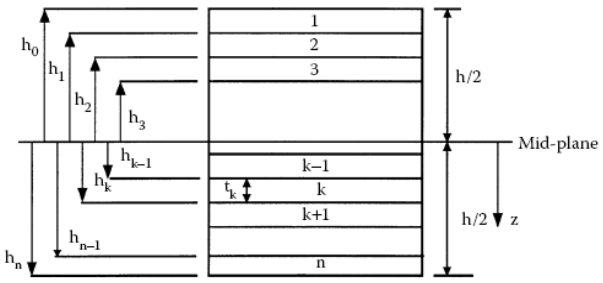

Figure 2.7: Coordinate locations of plies in a laminate

Integrating the global stresses in each lamina gives the resultant forces per unit length in the x_1–x_2 plane through the laminate thickness as

$$\begin{bmatrix} N_1 \\ N_2 \\ N_6 \end{bmatrix} = \sum_{k=1}^{n} \int_{h_{k-1}}^{h_k} \begin{bmatrix} \overline{\sigma_1} \\ \overline{\sigma_2} \\ \overline{\sigma_6} \end{bmatrix} dz = \sum_{k=1}^{n} \int_{h_{k-1}}^{h_k} \left(\begin{bmatrix} \overline{Q}_{11} & \overline{Q}_{12} & \overline{Q}_{13} \\ \overline{Q}_{21} & \overline{Q}_{22} & \overline{Q}_{23} \\ \overline{Q}_{61} & \overline{Q}_{62} & \overline{Q}_{66} \end{bmatrix}_k \left\{ \begin{bmatrix} \overline{\varepsilon_1} \\ \overline{\varepsilon_2} \\ \overline{\gamma_6} \end{bmatrix} - \begin{bmatrix} \overline{\alpha_1} \\ \overline{\alpha_2} \\ \overline{\alpha_6} \end{bmatrix} \Delta T - \begin{bmatrix} \overline{\beta_1} \\ \overline{\beta_2} \\ \overline{\beta_6} \end{bmatrix} \Delta C \right\} \right)$$

$$- \begin{bmatrix} 0 & 0 & \overline{e_{31}} \\ 0 & 0 & \overline{e_{32}} \\ 0 & 0 & \overline{e_{36}} \end{bmatrix}_k \begin{Bmatrix} \overline{\xi_1} \\ \overline{\xi_2} \\ \overline{\xi_3} \end{Bmatrix}_k = \begin{bmatrix} A_{11} & A_{12} & A_{16} \\ A_{21} & A_{22} & A_{26} \\ A_{16} & A_{26} & A_{66} \end{bmatrix} \begin{Bmatrix} \overline{\varepsilon_1^0} \\ \overline{\varepsilon_2^0} \\ \overline{\gamma_6^0} \end{Bmatrix} + z \begin{bmatrix} B_{11} & B_{12} & B_{16} \\ B_{21} & B_{22} & B_{26} \\ B_{16} & B_{26} & B_{66} \end{bmatrix} \begin{Bmatrix} \overline{\varepsilon_1^1} \\ \overline{\varepsilon_2^1} \\ \overline{\gamma_6^1} \end{Bmatrix} - \begin{bmatrix} \overline{N_1^{HT}} \\ \overline{N_2^{HT}} \\ \overline{N_6^{HT}} \end{bmatrix} - \begin{bmatrix} \overline{N_1^{P}} \\ \overline{N_2^{P}} \\ \overline{N_6^{P}} \end{bmatrix} \tag{2.36}$$

where N^{HT} and N^{P} are the thermal and electric force resultants which are given as

$$\begin{bmatrix} \overline{N_1^{HT}} \\ \overline{N_2^{HT}} \\ \overline{N_6^{HT}} \end{bmatrix} = \sum_{k=1}^{n} \int_{h_{k-1}}^{h_k} \begin{bmatrix} \overline{Q}_{11} & \overline{Q}_{12} & \overline{Q}_{13} \\ \overline{Q}_{21} & \overline{Q}_{22} & \overline{Q}_{23} \\ \overline{Q}_{61} & \overline{Q}_{62} & \overline{Q}_{66} \end{bmatrix}_k \left\{ \begin{bmatrix} \overline{\varepsilon_1} \\ \overline{\varepsilon_2} \\ \overline{\gamma_6} \end{bmatrix} - \begin{bmatrix} \overline{\alpha_1} \\ \overline{\alpha_2} \\ \overline{\alpha_6} \end{bmatrix}_k \Delta T - \begin{bmatrix} \overline{\beta_1} \\ \overline{\beta_2} \\ \overline{\beta_6} \end{bmatrix}_k \Delta C \right\} \tag{2.37}$$

$$\begin{bmatrix} \overline{N_1^{P}} \\ \overline{N_2^{P}} \\ \overline{N_6^{P}} \end{bmatrix} = \sum_{k=1}^{n_a} \int_{h_{k-1}}^{h_k} \begin{bmatrix} 0 & 0 & \overline{e_{31}} \\ 0 & 0 & \overline{e_{32}} \\ 0 & 0 & \overline{e_{36}} \end{bmatrix}_k \begin{Bmatrix} \overline{\xi_1} \\ \overline{\xi_2} \\ \overline{\xi_3} \end{Bmatrix}_k dz \tag{2.38}$$

where n_a is the number of actuating layers. Similarly, integrating the global stresses in each lamina gives the resulting moments per unit length in the x–y plane through the laminate thickness as

$$\begin{bmatrix} M_1 \\ M_2 \\ M_6 \end{bmatrix} = \begin{bmatrix} B_{11} & B_{12} & B_{16} \\ B_{21} & B_{22} & B_{26} \\ B_{16} & B_{26} & B_{66} \end{bmatrix} \begin{Bmatrix} \overline{\varepsilon_1^0} \\ \overline{\varepsilon_2^0} \\ \overline{\gamma_6^0} \end{Bmatrix} + \begin{bmatrix} D_{11} & D_{12} & D_{16} \\ D_{21} & D_{22} & D_{26} \\ D_{16} & D_{26} & D_{66} \end{bmatrix} \begin{Bmatrix} \overline{\varepsilon_1^1} \\ \overline{\varepsilon_2^1} \\ \overline{\gamma_6^1} \end{Bmatrix} - \begin{bmatrix} \overline{M_1^{HT}} \\ \overline{M_2^{HT}} \\ \overline{M_6^{HT}} \end{bmatrix} - \begin{bmatrix} \overline{M_1^{P}} \\ \overline{M_2^{P}} \\ \overline{M_6^{P}} \end{bmatrix} \quad (2.39)$$

where M^{HT} and M^{P} are thermal and electric moment resultants given as

$$\begin{bmatrix} \overline{M_1^{HT}} \\ \overline{M_2^{HT}} \\ \overline{M_6^{HT}} \end{bmatrix} = \sum_{k=1}^{n} \int_{h_{k-1}}^{h_k} \begin{bmatrix} \overline{Q}_{11} & \overline{Q}_{12} & \overline{Q}_{13} \\ \overline{Q}_{21} & \overline{Q}_{22} & \overline{Q}_{23} \\ \overline{Q}_{61} & \overline{Q}_{62} & \overline{Q}_{66} \end{bmatrix}_k \left\{ \begin{bmatrix} \overline{\varepsilon_1} \\ \overline{\varepsilon_2} \\ \overline{\gamma_6} \end{bmatrix} - \begin{bmatrix} \overline{\alpha_1} \\ \overline{\alpha_2} \\ \overline{\alpha_6} \end{bmatrix}_k \Delta T - \begin{bmatrix} \overline{\beta_1} \\ \overline{\beta_2} \\ \overline{\beta_6} \end{bmatrix}_k \Delta C \right\} z dz \quad (2.40)$$

$$\begin{bmatrix} \overline{M_1^{P}} \\ \overline{M_2^{P}} \\ \overline{M_6^{P}} \end{bmatrix} = \sum_{k=1}^{n_a} \int_{z_{k-1}}^{z_k} \begin{bmatrix} 0 & 0 & \overline{e_{31}} \\ 0 & 0 & \overline{e_{32}} \\ 0 & 0 & \overline{e_{36}} \end{bmatrix}^k \begin{Bmatrix} \overline{\xi_1} \\ \overline{\xi_2} \\ \overline{\xi_3} \end{Bmatrix}^k z dz \quad (2.41)$$

where N_1, N_2 are the normal force per unit length, N_6 is the shear force per unit length, M_1, M_2 are the bending moments per unit length and M_6 is the twisting moments per unit length.

The A, B, and D matrices are called the extensional, coupling, and bending stiffness matrices, respectively. The extensional stiffness matrix A relates the resultant in-plane forces to the in-plane strains, and the bending stiffness matrix D relates the resultant bending moments to the plate curvatures. The coupling stiffness matrix B couples the force and moment terms to the midplane strains and midplane curvatures. Are given as,

$$A_{ij} = \sum_{k=1}^{n} \left[\overline{Q_{ij}}\right]_k (h_k - h_{k-1}) \rightarrow i = 1,2,6;\ j = 1,2,6$$
$$B_{ij} = \frac{1}{2}\sum_{k=1}^{n} \left[\overline{Q_{ij}}\right]_k ({h^2}_k - {h^2}_{k-1}) \rightarrow i = 1,2,6;\ j = 1,2,6 \qquad (2.42)$$
$$D_{ij} = \frac{1}{3}\sum_{k=1}^{n} \left[\overline{Q_{ij}}\right]_k ({h^3}_k - {h^3}_{k-1}) \rightarrow i = 1,2,6;\ j = 1,2,6$$

The stress resultants are related to the displacement gradients and electric fields as follows

$$\begin{bmatrix} N_1 \\ N_2 \\ N_6 \end{bmatrix} = \begin{bmatrix} A_{11} & A_{12} & A_{16} \\ A_{21} & A_{22} & A_{26} \\ A_{16} & A_{26} & A_{66} \end{bmatrix} \begin{Bmatrix} \frac{\partial u_0}{\partial x_1} + \frac{1}{2}\left(\frac{\partial w_0}{\partial x_1}\right)^2 \\ \frac{\partial v_0}{\partial x_2} + \frac{1}{2}\left(\frac{\partial w_0}{\partial x_2}\right)^2 \\ \frac{\partial u_0}{\partial x_2} + \frac{\partial v_0}{\partial x_1} + \frac{\partial w_0}{\partial x_1}\frac{\partial w_0}{\partial x_2} \end{Bmatrix} - \begin{bmatrix} B_{11} & B_{12} & B_{16} \\ B_{21} & B_{22} & B_{26} \\ B_{16} & B_{26} & B_{66} \end{bmatrix} \begin{Bmatrix} \frac{\partial^2 w_0}{\partial {x_1}^2} \\ \frac{\partial^2 w_0}{\partial {x_2}^2} \\ 2\frac{\partial^2 w_0}{\partial x_1 \partial x_2} \end{Bmatrix} \qquad (2.43)$$
$$- \begin{Bmatrix} A_1^{HT} \\ A_2^{HT} \\ A_6^{HT} \end{Bmatrix} - \begin{Bmatrix} A_1^{P} \\ A_2^{p} \\ A_6^{p} \end{Bmatrix}$$

$$\begin{bmatrix} M_1 \\ M_2 \\ M_6 \end{bmatrix} = \begin{bmatrix} B_{11} & B_{12} & B_{16} \\ B_{21} & B_{22} & B_{26} \\ B_{16} & B_{26} & B_{66} \end{bmatrix} \begin{Bmatrix} \frac{\partial u_0}{\partial x_1} + \frac{1}{2}\left(\frac{\partial w_0}{\partial x_1}\right)^2 \\ \frac{\partial v_0}{\partial x_2} + \frac{1}{2}\left(\frac{\partial w_0}{\partial x_2}\right)^2 \\ \frac{\partial u_0}{\partial x_2} + \frac{\partial v_0}{\partial x_1} + \frac{\partial w_0}{\partial x_1}\frac{\partial w_0}{\partial x_2} \end{Bmatrix} - \begin{bmatrix} D_{11} & D_{12} & D_{16} \\ D_{21} & D_{22} & D_{26} \\ D_{16} & D_{26} & D_{66} \end{bmatrix} \begin{Bmatrix} \frac{\partial^2 w_0}{\partial {x_1}^2} \\ \frac{\partial^2 w_0}{\partial {x_2}^2} \\ 2\frac{\partial^2 w_0}{\partial x_1 \partial x_2} \end{Bmatrix}$$
$$- \begin{Bmatrix} B_1^{HT} \\ B_2^{HT} \\ B_6^{HT} \end{Bmatrix} - \begin{Bmatrix} B_1^{p} \\ B_2^{p} \\ B_6^{p} \end{Bmatrix} \qquad (2.44)$$

Assuming that the electric fields vary linearly within k_{th} layer; the hygrothermal and piezoelectric stiffnesses are defined as [33]

$$A_i^{HT} = \frac{1}{2}\sum_{k=1}^{N}\sum_{j=1,2,6}\overline{Q_{ij}^k}\overline{\alpha_j^k}(T_1^k + T_2^k)h_k + \overline{Q_{ij}^k}\overline{\beta_j^k}(C_1^k + C_2^k)h_k \tag{2.45}$$

$$\begin{aligned} B_i^{HT} &= \frac{1}{6}\sum_{k=1}^{N}\sum_{j=1,2,6}\overline{Q_{ij}^k}\overline{\alpha_j^k}[T_1^k(h_k + 3z_k) + T_2^k(2h_k + 3z_k)]h_k \\ &+\overline{Q_{ij}^k}\overline{\beta_j^k}[C_1^k(h_k + 3z_k) + C_2^k(2h_k + 3z_k)]h_k \end{aligned} \tag{2.46}$$

$$A_i^p = \frac{1}{2}\sum_{k=1}^{Na}\sum_{j=1,2,6}\overline{Q_{ij}^k}\overline{d_{3j}^k}(\xi_1^k + \xi_1^k)h_k \tag{2.47}$$

$$B_i^p = \frac{1}{6}\sum_{k=1}^{Na}\sum_{j=1,2,6}\overline{Q_{ij}^k}\overline{d_{3j}^k}[\xi_1^k(h_k + 3z_k) + \xi_2^k(2h_k + 3z_k)]h_k \tag{2.48}$$

The electric field E is defined as

$$\xi_1^k = \xi_2^k = \frac{V_k}{h_k} \tag{2.49}$$

where V_k is the applied voltage across the k^{th} layer and h_k is the thickness of the layer. Here we want to note that the direction of application of the electric field varies with the direction of polarization of the piezoelectric material.

CHAPTER III

SHAPE CONTROL OF COMPOSITE LAMINATES USING PIEZOELECTRIC MATERIALS

In this chapter, we start by introducing various piezoelectric materials which are used as actuators for shape control of smart structures which include piezoelectric fiber composites such as AFC and MFC. A detailed analytical solution is then presented for analyzing deformation of a cantilever beam based on the theory of elasticity; the results were compared with the solutions obtained from mechanics of materials and a model implemented using the commercial finite element software Abaqus. The aim for presenting this solution is to gain strong confidence in the element type and mesh size used in the FE analysis while dealing with more complex structures. The effect of using several different types of actuators on the behavior of a composite laminate is also studied and compared with each other in order to observe their capability in controlling deformation in composite beams due to external stimuli such as thermal or mechanical deformations. The actuators considered and their properties are summarized in Table 3.1 on page 59. The composite laminate is made of Carbon/Epoxy AS4 (3501-6) with symmetric laminates [Actuator/90/45/-45/0]s where the FE software Abaqus is used to perform this study.

3.1 Piezoelectric Materials

The phenomenon of piezoelectricity was discovered in 1880 by the Jacques and Pierre Curie brothers. They found out that when a mechanical stress was applied on crystals such as tourmaline, tourmaline, topaz, quartz, Rochelle salt and cane sugar,

electrical charges appeared with opposite signs on opposite surfaces and there charges were proportional to the stress.

Significant impetus has been generated by the discovery of piezoelectricity in polycrystalline ceramic materials like barium-titanate (BT) in the 1940's and lead-zirconate-titanate (PZT) in the 1950's; the latter still dominates transducer applications since it attains relatively high compliance and high piezoelectric properties, making them suitable as actuators. Semicrystalline piezoelectric polymers on the basis of polyvinylidenefluoride (PVDF) usually in the form of thin films have been available since the late 1960's. Newer development tendencies are directed towards the improvement of PZT ceramics by doping them with additional components such as La2O3 or producing artificial piezoelectric monocrystals [34].

Piezoelectric materials exhibit electromechanical coupling, which is useful for the design of devices for sensing and actuation. The coupling is exhibited by the fact that piezoelectric materials produce an electrical displacement when a mechanical stress is applied which is termed the direct piezoelectric effect and can also produce mechanical strain under the application of an electric field which is known as the converse piezoelectric effect.

Traditional piezoelectric ceramics are brittle and easy to break during handling and service. Piezoelectric Fiber Composite (PFC) was developed to improve the fault of piezoelectric ceramics. It is formed by combining piezoelectric ceramic fibers and epoxy matrix sandwiched between two electrode layers. They have high stiffness and large bandwidth, making them possible to use a wide range of signals in actuator applications.

They also have better strength and conformability than PZTs, creating more flexible and pliable structure and improving resistant to brittle damage and they can be integrated into laminated composite structures or other host structures and used for health monitoring, energy harvesting, and controlling shape changes.

3.1.1 Active Fiber Composite

Active fiber composites AFCs have been proven as a commercial efficient method for large-scale actuation and sensing in active structures. Through a series of projects active fiber composites have matured from objects of laboratory study to a technology for meeting the demands of high performance defense applications, as well as those of emerging commercial markets for smart technology devices. AFCs have been successfully implemented in a number of defense applications, including integral actuators for dynamic twist control in rotorcraft blades, systems to reduce radiated noise in torpedoes, and buffet load alleviation and vibration damping on twin tail military aircraft. Commercial applications for AFCs include active structural control in sporting goods products, as well as systems for condition-based maintenance and structural health monitoring in automotive and aerospace markets [35].

AFC actuators consist of unidirectional, aligned piezoelectric fibers, a resin matrix system, and interdigital electrodes, as shown in Figure 3.1. The advantages over monolithic piezoceramic actuators include higher planar actuation strains, tailorable directional actuation, robustness to damage, conformability to curved surfaces, and potential for large area distributed actuation and sensing systems. Piezoceramic fibers of

small (~250 μm) characteristic crosssectional dimension provide increased specific strength over monolithic materials.

Integral passive materials laminated into the composite, such as glass fibers, can further improve toughness, increasing robustness without compromising the ability to conform to curved shapes. Active fiber composites operate in the longitudinal mode and thus have significantly higher specific work output than planar monolithic piezoceramics. In addition, the directional nature of actuation permits design of modal actuators and sensors without reliance on the host structure to transmit the actuation through structural coupling mechanisms. Large area, multiple ply AFC actuators are easy to fabricate, simplifying leads and connections, and minimizing technology insertion costs.

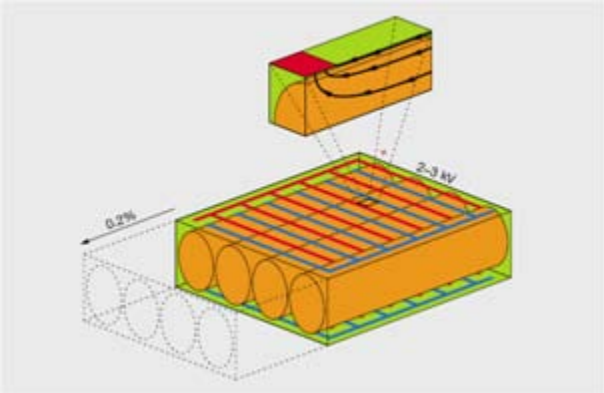

Figure 3.1: Active fiber composite concept [17]

More demanding AFC applications require improved part-to-part consistency and greater mechanical displacement and force outputs. In the military these applications include distributed integral actuators for active aeroelastic control in sensorcraft and unmanned combat air vehicles (UCAVs). In these applications, improvements in

actuator strain and energy density are paramount. Other applications include structural-acoustic control on launch vehicle shrouds to reduce noise transmission to the payload, which require conformable actuators of high authority. In many commercial applications, higher strain output at lower electric fields is needed to reduce costs associated with high voltage drive and control electronics.

3.1.2 Microfiber Composite

Microfiber Composites are similar to the AFCs in the sense that both consist of the same three primary components; active piezoceramic fibers aligned in a unidirectional manner, interdigitated electrodes, and an adhesive polymer matrix, however, the MFC has one difference that greatly affects the manufacturing process and the performance of the actuator, it has rectangular fibers embedded in the polymer matrix. In addition, MFC results in larger fiber volume contents than the AFC moreover; the maximum fiber volume content of AFC is less than 0.785 because of the restriction in the fiber geometry. The fiber volume content of MFC could reach up to 0.824 [18]. High fiber volume content enhances the performance of the composite and improves the stiffness and strength of the composites. The MFC is extremely flexible, durable and has the advantage of higher Electromechanical coupling coefficients granted through the interdigitated electrodes. Allowing the MFC to be produced at a much lower cost than the AFC and therefore are causing the AFC to be overlooked when determining the ideal actuator for a specific application. Additionally, the rectangular fiber geometry of the MFC guarantees consistent contact between the IDEs and piezoceramic fibers, reducing attenuation on the IDE electric field due to the low dielectric constant of the epoxy

matrix. Because of the improved electrical contact, MFC strain performance exceeds AFC strain performance by up to 150% [36]. Since both AFC and MFC use polymer matrix constituents which are known for their viscoelastic behavior, this could result in the overall time-dependent behaviors of these actuators.

Engineering properties of MFC are determined either estimated or experimentally found, a complete and experimentally validated set of orthotropic mechanical properties can be found in [37]. Measuring the maximum free-strain actuation capabilities of a typical reference MFC device, the maximum peak-to-peak actuation strain of approximately 2000 micro strain in the longitudinal direction is typical for all NASA-standard MFC devices. The free-strain output of the MFC, as with most piezoceramic devices, varies considerably with the driving electric field amplitude. This variability in effective piezoelectric constants (d_{33}, d_{31}) is nonlinear, but repeatable.

3.2 Finite Element Verification

A detailed analytical solution for a cantilever beam under the application of a tip load based on the theory of elasticity for one material and a composite material is presented in order to obtain the displacement field; the results were compared with the solutions from mechanics of materials and a model implemented using the commercial finite element software Abaqus. The aim of presenting this solution is to gain strong confidence in the element type and mesh size used while dealing with more complex structures. The geometry and the loading of the composite beam considered are shown in Figure 3.2. We first consider the case of having a material with piezoelectric properties and another without.

The BC's at the top and bottom are given as

$$\begin{aligned} y = b, n = j,\ t = 0, &\rightarrow \sigma_{xy}^{(1)} = 0,\ \sigma_{yy}^{(1)} = 0 \\ y = -b, n = -j,\ t = 0, &\rightarrow \sigma_{xy}^{(2)} = 0,\ \sigma_{yy}^{(2)} = 0 \end{aligned} \tag{3.1}$$

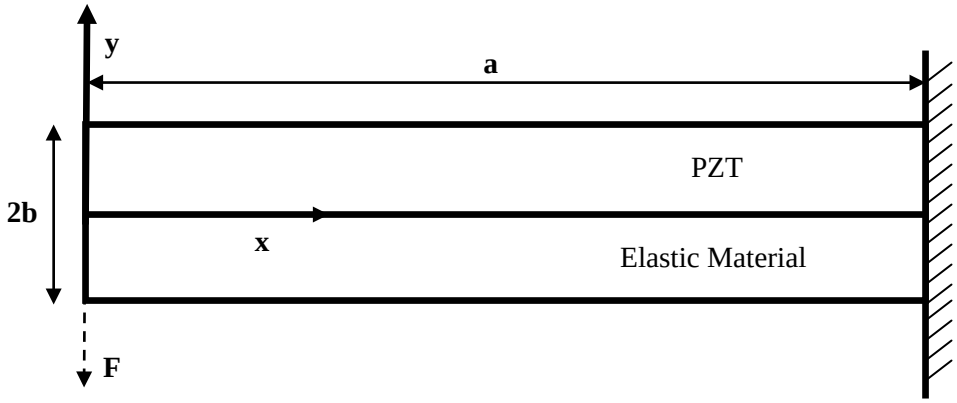

Figure 3.2: Cantilever composite beam made of a two different materials under a tip load

where superscript (1) indicates the elastic material layer and (2) indicates the PZT layer, also, note that **t** is defined as the traction vector, **n** is the unit outward normal (*i, j, k*) vector. The BC's at x = 0,

Forces

$$-Fj = \int_{-b}^{0} t dA + \int_{0}^{b} t dA \tag{3.2}$$

$$-F = \int_{-b}^{0} -\sigma_{xy}^{(1)} dy - \int_{0}^{b} \sigma_{xy}^{(2)} dy \tag{3.3}$$

Moments

$$0 = \int_{-b}^{0} -y\sigma_{xx}^{(1)} dy - \int_{0}^{b} y\sigma_{xx}^{(2)} dy \tag{3.4}$$

In order to solve this problem, we are going to assume an Airy stress function of the form

$$\begin{aligned} \Phi_1 &= c_1 xy^3 + c_2 xy + c_3 xy^2 \text{ for Elastic Material} \\ \Phi_2 &= c_4 xy^3 + c_5 xy + c_6 xy^2 \text{ for the Piezoelectric Material} \end{aligned} \tag{3.5}$$

where c_1-c_6 are unknowns to be determined and from boundary, equilibrium and compatibility conditions. Following the Theory of Elasticity for plane problems we have

$$\sigma_{xx} = \Phi_{,yy} \quad \sigma_{yy} = \Phi_{,xx} \quad \sigma_{xy} = -\Phi_{,xy} \tag{3.6}$$

where "," denotes differentiation with respect to the indicial variable. Substituting Eq. (3.5) into Eq. (3.6) we get

$$\begin{aligned} \sigma_{xx}^{(1)} &= 6c_1 xy + 2c_3 x & \sigma_{xx}^{(2)} &= 6c_4 xy + 2c_6 x \\ \sigma_{yy}^{(1)} &= 0 & \sigma_{yy}^{(2)} &= 0 \\ \sigma_{xy}^{(1)} &= -3c_1 y^2 - c_2 - 2c_3 y & \sigma_{xy}^{(2)} &= -3c_4 y^2 - c_5 - 2c_6 y \end{aligned} \tag{3.7}$$

Substituting into Eq. (3.1) and Eq. (3.3) obtaining

$$\begin{aligned} &\sigma_{xy}^{(1)}(x,\ y = -b) = 0 \\ &-3c_1 b^2 - c_2 + 2c_3 b = 0 \\ &\sigma_{xy}^{(2)}(x,\ y = b) = 0 \\ &-3c_4 b^2 - c_5 - 2c_6 b = 0 \end{aligned} \tag{3.8}$$

$$-F = c_1 b^3 + c_2 b - c_3 b^2 + c_4 b^3 + c_5 b + c_6 b^2 \tag{3.9}$$

At the interface (x, y = 0); the tractions are equal and opposite i.e $t_1 = -t_2$

$$\sigma_{xy}^{(1)} = \sigma_{xy}^{(2)} \text{ and } \sigma_{yy}^{(1)} = \sigma_{yy}^{(2)} \tag{3.10}$$

Giving

$$c_2 = c_5 \tag{3.11}$$

From Stress-Strain & Strain-Displacement relations we find that

$$\varepsilon_{ij} = \frac{1+\nu}{E}\sigma_{ij} - \frac{\nu}{E}\sigma_{kk}\delta_{ij} \text{ where } i, j, k = x, y \tag{3.12}$$

Written in terms of displacements and in matrix format as follows

$$[\varepsilon] = \begin{bmatrix} u_{x,x} & \frac{1}{2}(u_{x,y} + u_{y,x}) & 0 \\ \frac{1}{2}(u_{x,y} + u_{y,x}) & u_{y,y} & 0 \\ 0 & 0 & 0 \end{bmatrix} \tag{3.13}$$

$$\varepsilon_{xx}^{(1)} = u_{x,x}^{(1)} = \frac{\sigma_{xx}^{(1)}}{E_1} \qquad u_x^{(1)} = \int \frac{\sigma_{xx}^{(1)}}{E_1} dx + A(y)$$

$$\varepsilon_{yy}^{(1)} = u_{y,y}^{(1)} = -\nu_1 \frac{\sigma_{xx}^{(1)}}{E_1} \qquad u_y^{(1)} = \int -\nu_1 \frac{\sigma_{xx}^{(1)}}{E_1} dx + B(x)$$

(3.14)

where E_1, v_1 are the Young's modulus and Poisson's ratio for the first material respectively. A(y), B(x) are constants of integration. Substituting the stress values we get

$$u_x^{(1)} = \left(\frac{3}{E_1}\right)c_1x^2y + \left(\frac{1}{E_1}\right)c_3x^2 + \quad (y)A$$
$$u_y^{(1)} = \left(\frac{-3\nu_1}{E_1}\right)c_1xy^2 - \left(\frac{2\nu_1}{E_1}\right)c_3xy + B(x) \tag{3.15}$$

Now, for the piezoelectric material we have the constitutive relations defined by Eq. (2.6) and assuming open circuit analysis for the piezoelectric (i.e D = 0) we have

$$\varepsilon_{xx}^{(2)} = u_{x,x}^{(2)} = S_{11}\sigma_{xx}^{(2)} + d_{31}E_3 \qquad u_x^{(2)} = \int (S_{11}\sigma_{xx}^{(2)} + d_{31}\xi_3)dx + C(y)$$
$$\varepsilon_{yy}^{(2)} = u_{y,y}^{(2)} = S_{21}\sigma_{xx}^{(2)} + d_{32}E_3 \qquad u_y^{(2)} = \int (S_{21}\sigma_{xx}^{(2)} + d_{32}\xi_3)\ dx + D(x) \tag{3.16}$$

where S_{11} and S_{12} are the first and second components in the compliance matrix respectively. It can be observed from Eq. (3.16) that the electric field used is ξ_3 and this is due to the fact that most piezoelectric materials are poled through their thickness and the electric field is applied in that similar direction. C(y) and D(x) are constants of integration. Substituting the stress values we get

$$u_x^{(2)} = S_{11}\left(3c_4x^2y + c_6x^2\right) + d_{31}\xi_3x + C(y)$$
$$u_y^{(2)} = S_{21}\left(3c_4xy^2 + 2c_6xy\right) + d_{32}\xi_3y + D(x) \tag{3.17}$$

Also, defining the shear strains for elastic material as

$$2\varepsilon_{xy}^{(1)} = u_{x,y}^{(1)} + u_{y,x}^{(1)} \quad 2\lambda\sigma_{xy}^{(1)} = u_{x,y} + u_{y,x}$$
$$2\lambda\left(-3c_1y^2 - c_2 - 2c_3y\right) = \left(\frac{3}{E_1}\right)c_1x^2 + A'(y) \tag{3.18}$$
$$-\left(\frac{3v_1}{E_1}\right)c_1y^2 - \left(\frac{2v_1}{E_1}\right)c_3y + B'(x)$$

where $\lambda = ((1+v_1)/E_1)$. And for material 2 as

$$2\varepsilon_{xy}^{(2)} = u_{x,y}^{(2)} + u_{y,x}^{(2)} \quad 2\sigma_{xy}^{(2)} = u_{x,y} + u_{y,x}$$
$$2S_{66}(-3c_4y^2 - c_5 - 2c_6y) = S_{11}\left(3c_4x^2\right) + C\left(y\right) \tag{3.19}$$
$$+ S_{21}\left(3c_4y^2 + 2c_6y\right) + D\left(x\right)$$

Rearranging the above equation such that separating between x, y and the constants as follows.

For elastic material we get

$$6\lambda c_1y^2 - 4\lambda c_3y - A\left(y\right) + \left(\frac{3v_1}{E_1}\right)c_1y^2 + \left(\frac{2v_1}{E_1}\right)c_3y = F_1\left(y\right) \tag{3.20}$$

$$-\left(\frac{3}{E_1}\right)c_1x^2 - B\left(x\right) = G_1\left(x\right) \tag{3.21}$$

$$2\lambda c_2 = K_1 \tag{3.22}$$

$$F_1\left(y\right) + G_1\left(x\right) = K_1 \tag{3.23}$$

and for the PZT we get

$$-6S_{66}c_4y^2 - 4S_{66}c_6y - C\left(y\right) - S_{21}\left(3c_4y^2 + 2c_6y\right) = F_2\left(y\right) \tag{3.24}$$

$$-3S_{11}c_4x^2 - D\left(x\right) = G_2\left(x\right) \tag{3.25}$$

$$2S_{66}c_5 = K_2 \tag{3.26}$$

$$F_2\left(y\right) + G_2\left(x\right) = K_2 \tag{3.27}$$

Such equation means that F(x) must be some constant d and G(x) some constant e. Otherwise F(x) and G(y) would vary with x and y, respectively and by varying x alone, or y alone, the equality would be violated. Thus

$$\begin{aligned} d_1 + e_1 &= K_1 \\ d_2 + e_2 &= K_2 \end{aligned} \tag{3.28}$$

Equating Eq. (3.28) with both Eq. (3.20) and Eq. (3.24) we get

$$-6\lambda c_1 y^2 - 4\lambda c_3 y - A'(y) + \left(\frac{3v_1}{E_1}\right) c_1 y^2 + \left(\frac{2v_1}{E_1}\right) c_3 y = d_1 \ldots\ldots \text{ Rearranging}$$

$$A'(y) = -6\lambda c_1 y^2 - 4\lambda c_3 y - d_1 + \left(\frac{3v_1}{E_1}\right) c_1 y^2 + \left(\frac{2v_1}{E_1}\right) c_3 y \ldots\ldots \textit{Integrating} \tag{3.29}$$

$$A(y) = -2\lambda c_1 y^3 - 2\lambda c_3 y^2 - d_1 y + \left(\frac{v_1}{E_1}\right) c_1 y^3 + \left(\frac{v_1}{E_1}\right) c_3 y^2 + p_1$$

The same is done to B(x), C(y) and D(x), we get

$$B(x) = -\left(\frac{1}{E_1}\right) c_1 x^3 - e_1 x + p_2 \tag{3.30}$$

$$C(y) = -2S_{66} c_4 y^3 - 2S_{66} c_6 y^2 - d_2 y - S_{21}\left(c_4 y^3 + c_6 y^2\right) + p_3 \tag{3.31}$$

$$D(x) = -S_{11} c_4 x^3 - e_2 x + p_4 \tag{3.32}$$

Defining the BC's at x = a, y = 0 as

$$u_x^{(1)} = u_x^{(2)} = u_y^{(1)} = u_y^{(2)} = 0,\ u_{y,x}^{(1)} = u_{y,x}^{(2)} = 0 \tag{3.33}$$

From here, we get six equation and another two equations from Eq. (3.28), we can find p_1, p_2, p_3, p_4, e_1, e_2, d_1, d_2 as

$$
\begin{aligned}
p_1 &= -\left(\frac{1}{E_1}\right)c_3a^2 \\
p_2 &= \left(\frac{1}{E_1}\right)c_1a^3 + e_1a \\
p_3 &= -S_{11}c_6a^2 - d_{31}\xi_3a \\
p_4 &= S_{11}c_4a^3 + e_2a
\end{aligned}
\tag{3.34}
$$

$$
\begin{aligned}
e_1 &= -\left(\frac{3}{E_1}\right)c_1a^2 \\
e_2 &= -3S_{11}c_4a^2 \\
d_1 &= K_1 - e_1 \\
d_2 &= K_2 - e_2
\end{aligned}
\tag{3.35}
$$

Returning to the last BC which is the continuity of the displacements at the interface (x, y=0) i.e $u_{x1} = u_{x2}$, $u_{y1} = u_{y2}$ we get

$$\left(\frac{1}{E_1}\right)c_3x^2 + A(0) = S_{11}c_6x^2 + d_{31}\xi_3x + C(0) \tag{3.36}$$

$$B(x) = D(x) \tag{3.37}$$

Finally, we obtain six equations with six unknown's (c_1-c_6) and they can be solved by using any available mathematical software package such as Matlab. When considering the case of having two materials in which neither one exhibit piezoelectric properties, the solution is similar and the only difference will be in the constitutive model used for each material.

In addition, as a special case when both materials have the same properties resulting in the solution for a single material which is given as

$$2\mu u_y = -3c_1 xy^2 - c_2 x + \frac{D_1}{4} xy^2 - \frac{D_1}{6} x^3 + qx + b_1 \tag{3.38}$$

$$c_1 = \frac{F}{4b^3}, c_2 = -3c_1 b^2, D_1 = 6c_1(1-\nu), q = c_2 + \frac{D_1}{2} a^2$$

$$b_1 = -qa + \frac{D_1}{6} a^3 + c_2 a$$

(3.39)

From here we compare the results obtained from the previous derivation with that obtained from an FE model implemented using the commercial software Abaqus. The beam is modeled using 20-node quadratic continuum elements with reduced integration (C3D20R) for the elastic part and an extra degree of freedom for the electrical potential (C3D20RE) were used to model the part which exhibits piezoelectric properties. First, we compare the analytical results obtained from the elasticity solution for only one material with those obtained from mechanics of materials and the FE model. The FE beam model is meshed with 4 elements through the thickness, 8 elements along the width and 100 elements along the length; the mesh is presented in Figure 3.3. Figure 3.4 shows the deflection of an aluminum cantilever beam along its length measured from the center line under the action of a tip load (1kN). We see that the solution obtained from theory of elasticity and the FE model are very close to each other with a max error of 2% while 6% error was obtained when comparing it with that calculated from strength of materials. In the case of a composite material, we first consider two different materials where none of them exhibit piezoelectric properties

(both have elastic properties only). The composite consisted of steel as the first part and aluminum as the second part. The mesh is similar to that used in the single material case except that 4 elements were used through the thickness of each part of the beam. Figure 3.5 shows the deflection of the cantilever composite beam along its length measured from the center line under the action of a tip load (1kN). We see that the solution obtained from the theory of elasticity and the FE model are very close to each other with a max error of (3%).

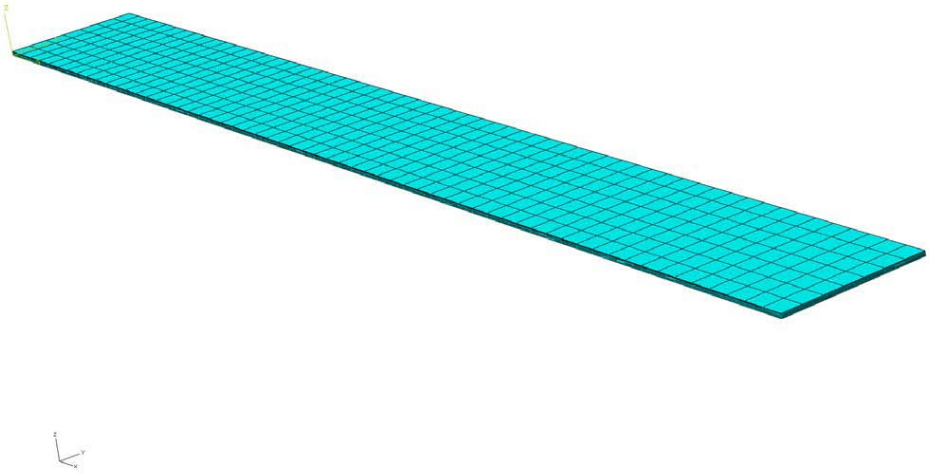

Figure 3.3: Mesh of the FE beam model

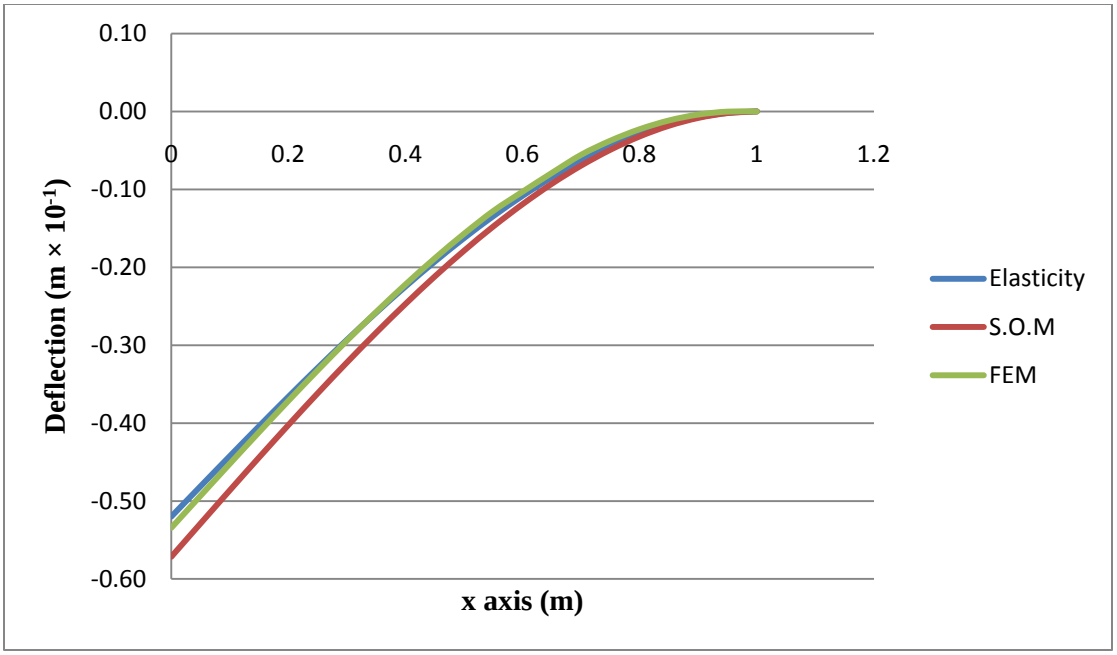

Figure 3.4: Predicted deflection of a cantilever homogenous beam using elasticity solution, strength of materials and finite elements

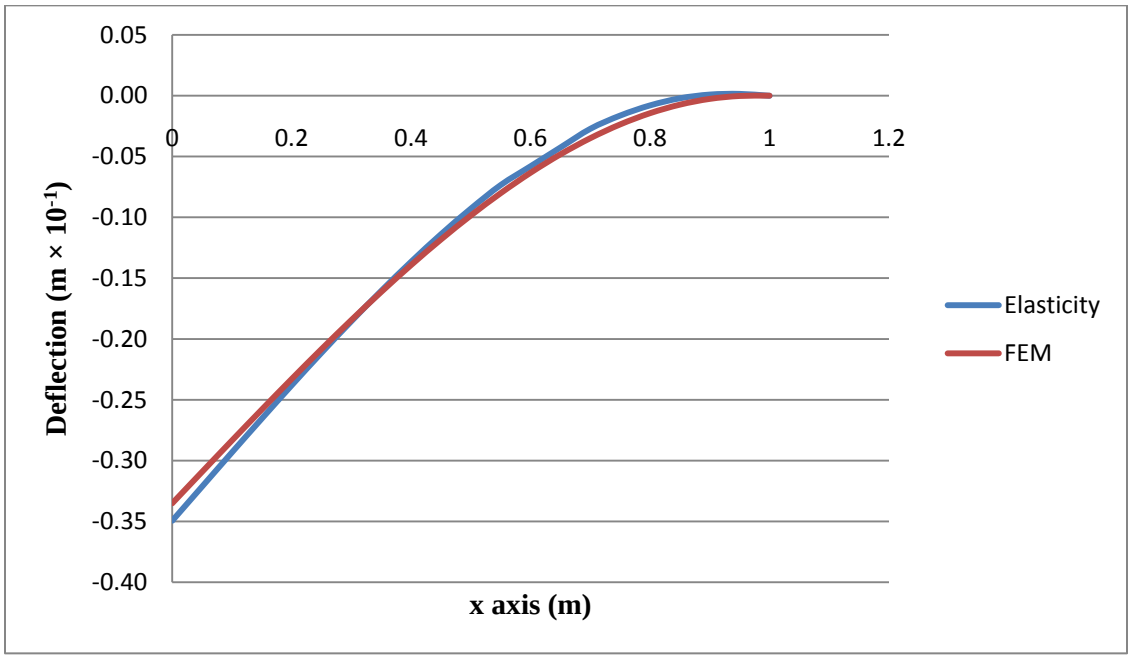

Figure 3.5: Predicted deflection of a composite beam using elasticity solution and finite elements

We also considered the case of a composite material but this time, one of the materials exhibits piezoelectric properties. The composite consisted of PZT-5H as the first part and aluminum as the second part. The mesh is similar to that used in the single material case except that 4 elements were used through the thickness of each part of the beam and an extra degree of freedom element for the electrical potential (C3D20RE) were used to model the part which exhibits piezoelectric properties. Figure 3.6 shows the deflection of the composite cantilever beam along its length measured from the center line under the action of a tip load of (1kN) and zero electric field along the piezoelectric material. We see that the solution obtained from the theory of elasticity and the FE model are very close to each other with a max error of (3%).

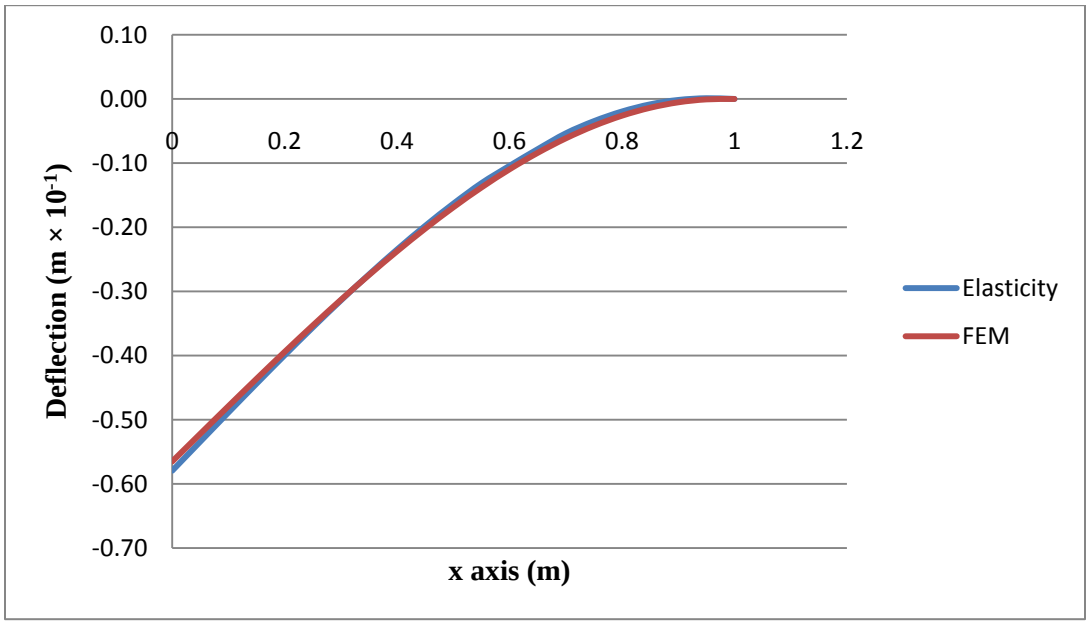

Figure 3.6: Predicted deflection of a composite beam with one part exhibiting piezoelectric properties using elasticity solution and finite elements

Moreover, we want to observe the effect of applying a voltage difference through the thickness of the active part on the deflection of an isotropic beam such as aluminum and compare the results with those obtained from FE. We consider the case of using a single piezoelectric patch on one side and on both sides of an elastic beam as shown in Figure 3.7. The equations governing the deflection of the beam under the application of a voltage difference for both cases are given as [38]

$$y(x) = \frac{K_1 V_1}{2}(x - x_1)^2$$
$$K_k = \frac{\kappa_k}{V_k} \rightarrow (k = 1, 2, ...n) \tag{3.40}$$

For the double actuator case the curvature equation is given as

$$\kappa = \frac{\xi_p d_{31} w_p \left[\frac{t}{2} + t_b + \frac{t_p}{2} \right](V_1 - V_2)}{EI} \tag{3.41}$$

And for the single actuator is given as

$$\kappa = \frac{M}{EI} - \frac{ES}{EI}\left[\frac{P(EI) - M(ES)}{(EA)(EI) - (ES)^2} \right] \tag{3.42}$$

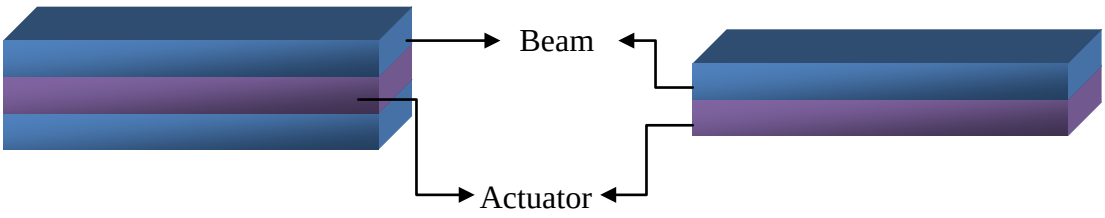

Figure 3.7: Schematic of a beam with double bond and single bonded actuator

It can be observed from Eq. (3.41) that when applying a similar voltage value to both actuators, the resulting deflection becomes zero and a tension compression effect will take place rather than an out of plane deflection. First, we consider using only one PZT actuator attached to an aluminum beam, the geometry of the beam is shown in Figure 3.8. The FE mesh is similar to those used in the mechanical load case except that 4 elements were used through the thickness of the aluminum beam and 2 elements through the actuator with an extra degree of freedom for the electrical potential.

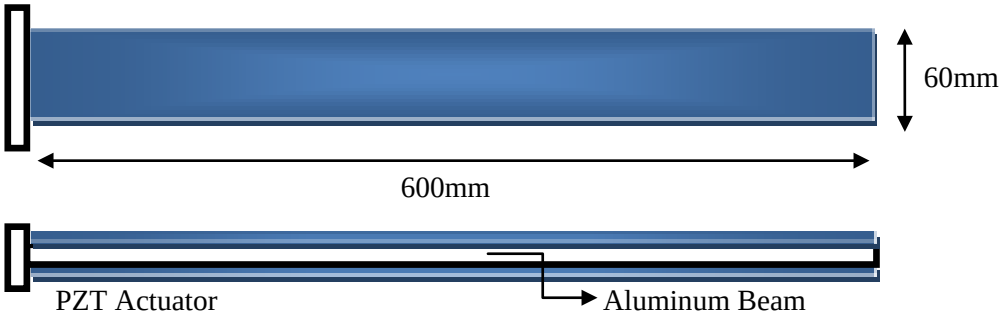

Figure 3.8: Schematic of the aluminum beam with PZT actuator

Figure 3.9 shows the deflection of a cantilever beam along its length measured from the center line subjected to a through the thickness voltage difference of 40V and 80V corresponding to a 20.5V/mm and 41V/mm electric field respectively. We see that the results obtained from the analytical solution and the FE model are very close to each other with a max error of (2%). Similarly, two actuators attached to an aluminum beam are also considered. Figure 3.9 shows the deflection of a cantilever beam along its length measured from the center line subjected to a voltage difference of 40V and 80V

corresponding to a 20.5V/mm and 41V/mm electric field respectively. We see that the results obtained from the analytical solution and the FE model are close to each other with a max error of (8%). Moreover, it can be concluded that when using a double bonded actuators more deflection is obtained for the same voltage value than the single bonded case due to the amplification displacement where each layer (ideally) will displace the same amount leading to higher deflection.

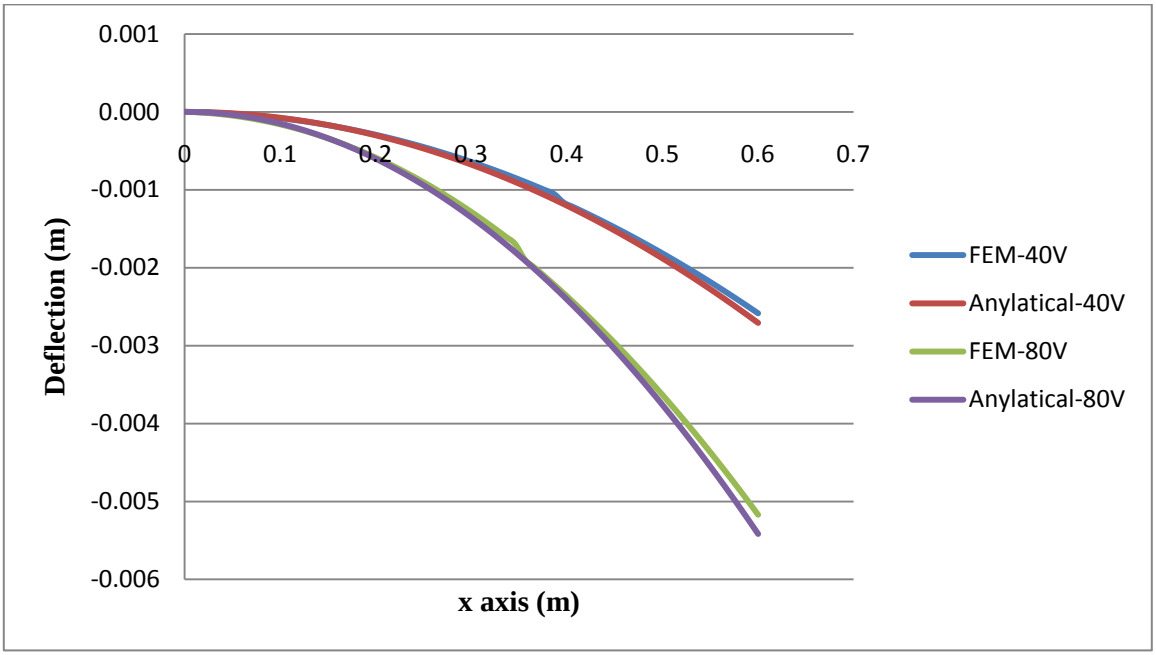

Figure 3.9: Predicted deflection of a composite beam using a single actuator under the application of through thickness electric potential

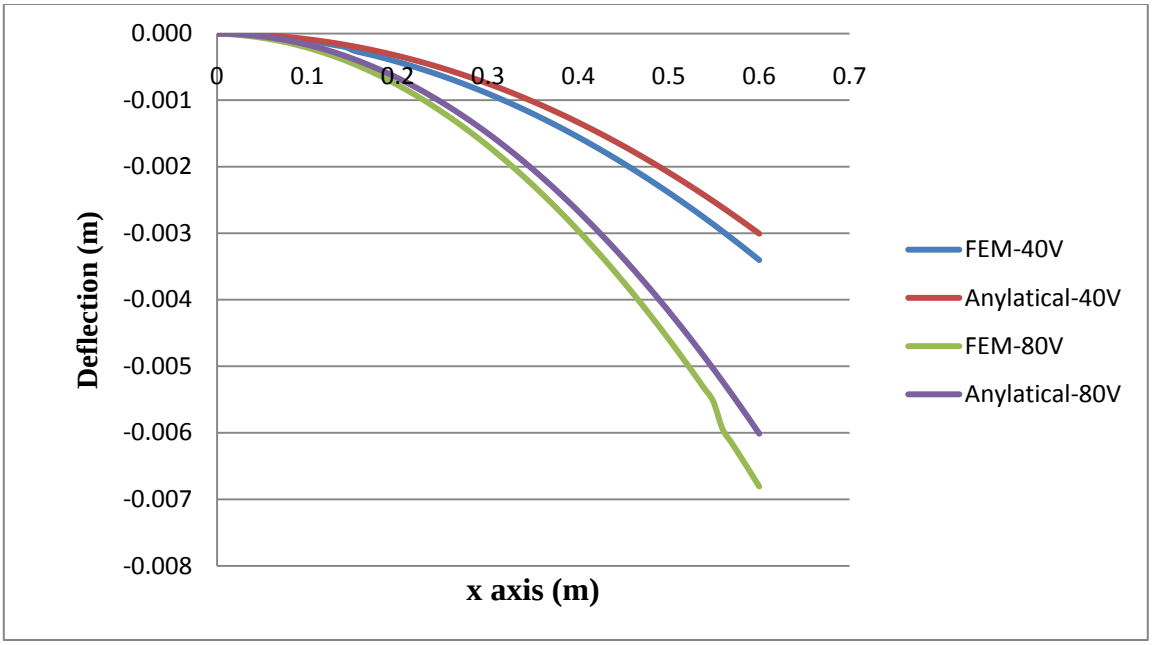

Figure 3.10: Predicted deflection of a composite beam for two actuators under the application of through thickness electric potential

From the previous analysis, we were able to verify the solution obtained from the FE model with analytical solutions, hence, we can use similar FE models to construct more complex structures as we will see in the previous section where we use patch actuators distributed along a composite laminate beam in order to observe their effect on the shape control of the composite beam.

3.3 The Analysis of Laminated Beams using CLPT

In dealing with symmetric laminates, the equations for bending deflection and stretching displacements are uncoupled; in the case when the in-plane forces are zero, the in-plane displacements (u, v) are zero and the problem is reduced to solving for bending deflection and stresses. In deriving the laminated beam theory we assume that

$$M_y = M_{xy} = 0 \tag{3.43}$$

Substituting into Eq. (2.40) gives in the absence of temperature effects

$$\begin{bmatrix} M_x \\ M_y \\ M_{xy} \end{bmatrix} = -\begin{bmatrix} D_{11} & D_{12} & D_{16} \\ D_{21} & D_{22} & D_{26} \\ D_{16} & D_{26} & D_{66} \end{bmatrix} \begin{Bmatrix} \frac{\partial^2 w_0}{\partial x_1^{\,2}} \\ \frac{\partial^2 w_0}{\partial x_2^{\,2}} \\ 2\frac{\partial^2 w_0}{\partial x_1 \partial x_2} \end{Bmatrix} - \begin{Bmatrix} B_1^p \\ B_2^p \\ B_6^p \end{Bmatrix} \tag{3.44}$$

In inverse form

$$\begin{Bmatrix} \frac{\partial^2 w_0}{\partial x_1^{\,2}} \\ \frac{\partial^2 w_0}{\partial x_2^{\,2}} \\ 2\frac{\partial^2 w_0}{\partial x_1 \partial x_2} \end{Bmatrix} = -inv\left(\begin{bmatrix} D_{11} & D_{12} & D_{16} \\ D_{21} & D_{22} & D_{26} \\ D_{16} & D_{26} & D_{66} \end{bmatrix}\right)\left(\begin{bmatrix} M_x \\ M_y \\ M_{xy} \end{bmatrix} + \begin{Bmatrix} B_1^p \\ B_2^p \\ B_6^p \end{Bmatrix}\right) \tag{3.45}$$

By assuming that the laminated beam under consideration is long enough compared to its width and thickness to make the effects of the Poisson ratio and shear coupling on the deflection negligible. Then the transverse deflection can be treated only as a function of coordinate x (along the length of the beam); from here we get

$$\frac{\partial^2 w_0}{\partial x_1^{\,2}} = -\widetilde{D_{11}}(M_x + B_1^p) \tag{3.46}$$

The "~" symbol indicates the components of the inverse matrix. For static bending without the axial force we have

$$\frac{\partial^2 w_0}{\partial x_1^{\,2}} = -\frac{M_x}{E_{xx} I_{yy}} \rightarrow E_{xx} I_{yy} \frac{\partial^4 w_0}{\partial x_1^{\,4}} = q \tag{3.47}$$

where $E_{xx} = \frac{12}{h^3 \widetilde{D_{11}}}$, $I_{yy} = \frac{1}{12} bh^3$, q is the distributed force, $\widetilde{D_{11}}$ is the coefficient of inverse of bending stiffness matrix. Equation. (3.47) is identical to the form, of the Euler-Bernoulli beam theory of homogeneous, isotropic beams. Considering a simply supported and a cantilever beam, we have the following boundary conditions respectively,

$$w_0(0) = 0; \frac{dw_0}{dx_1}(l/2) = 0$$
$$w_0(0) = 0; \frac{dw_0}{dx_1}(0) = 0 \tag{3.48}$$

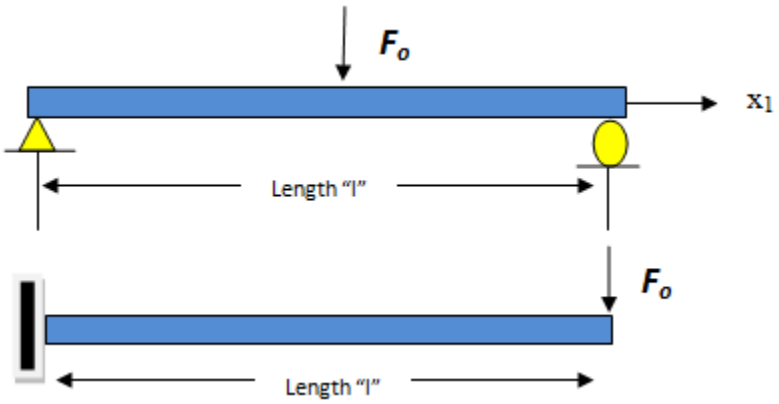

Figure 3.11: Schematic of a simply supported and a cantilever beam under application of point load

Applying these boundary conditions to the governing equations to get the transverse deflection of laminated composite beam including electric effects subjected to

point load as shown in Figure 3.11. The transverse deflection for a simply supported beam and a cantilever beam are given as

$$w_0(x_1) = \frac{1}{E_{xx} I_{yy}} \left[-\frac{F_0 x_1^{\,3}}{12} - \frac{B_1^p x_1^{\,2}}{2} + \frac{F_0 l^2 x_1}{16} + \frac{B_1^p l x_1}{2} \right] \tag{3.49}$$

$$w_0(x_1) = \frac{1}{E_{xx} I_{yy}} \left[-\frac{F_0 x_1^{\,3}}{12} - \frac{B_1^p x_1^{\,2}}{2} \right] \tag{3.50}$$

The in-plane stresses in the k_{th} layer can be computed from Eq. (2.24) and are given as

$$\bar{\sigma}_{x1}^k(x_1, x_3) = \frac{x_3(M(x_1) + B_1^p)}{b} \left(\overline{Q_{11}^k} \widetilde{D_{11}} + \overline{Q_{12}^k} \widetilde{D_{12}} + \overline{Q_{16}^k} \widetilde{D_{16}} \right) + \frac{x_3(B_2^p)}{b} \left(\overline{Q_{11}^k} \widetilde{D_{12}} + \overline{Q_{12}^k} \widetilde{D_{22}} + \overline{Q_{16}^k} \widetilde{D_{26}} \right) + \frac{x_3(B_6^p)}{b} \left(\overline{Q_{11}^k} \widetilde{D_{16}} + \overline{Q_{12}^k} \widetilde{D_{26}} + \overline{Q_{16}^k} \widetilde{D_{66}} \right) \tag{3.51}$$

$$\bar{\sigma}_{x2}^k(x_1, x_3) = \frac{x_3(M(x_1) + B_1^p)}{b} \left(\overline{Q_{12}^k} \widetilde{D_{11}} + \overline{Q_{22}^k} \widetilde{D_{12}} + \overline{Q_{26}^k} \widetilde{D_{16}} \right) + \frac{x_3(B_2^p)}{b} \left(\overline{Q_{12}^k} \widetilde{D_{12}} + \overline{Q_{22}^k} \widetilde{D_{22}} + \overline{Q_{26}^k} \widetilde{D_{26}} \right) + \frac{x_3(B_6^p)}{b} \left(\overline{Q_{12}^k} \widetilde{D_{16}} + \overline{Q_{22}^k} \widetilde{D_{26}} + \overline{Q_{26}^k} \widetilde{D_{66}} \right) \tag{3.52}$$

$$\bar{\sigma}_{x1x2}^k(x_1, x_3) = \frac{x_3(M(x_1) + B_1^p)}{b} \left(\overline{Q_{16}^k} \widetilde{D_{11}} + \overline{Q_{26}^k} \widetilde{D_{12}} + \overline{Q_{66}^k} \widetilde{D_{16}} \right) + \frac{x_3(B_2^p)}{b} \left(\overline{Q_{16}^k} \widetilde{D_{12}} + \overline{Q_{26}^k} \widetilde{D_{22}} + \overline{Q_{66}^k} \widetilde{D_{26}} \right) + \frac{x_3(B_6^p)}{b} \left(\overline{Q_{16}^k} \widetilde{D_{16}} + \overline{Q_{26}^k} \widetilde{D_{26}} + \overline{Q_{66}^k} \widetilde{D_{66}} \right) \tag{3.53}$$

The stresses given above are approximate and are not valid especially in the free-edge zone, where the stress state is three dimensional. The width of the edge zone is about the order of the thickness of the beam.

3.4 Shape Control of Composite Laminates

In the following section, we present the effect of using several different types of actuators on the shape control of composite laminates, the actuators considered and their properties are summarized in Table 3.1, note that subscript 1 indicates longitudinal fiber direction in the composite while 3 indicates the poling direction for piezoelectric materials. Active fiber composites can be classified into two types based on the method used in embedding the active fibers into the passive matrix. Figure 3.12 shows a schematic of the first type, where, the PZT rods are incorporated into the matrix along the actuator thickness; a similar behavior is observed to that when using pure PZT actuators where the voltage is applied through the actuator thickness. The second type is shown in Figure 3.13, in this type, the fibers are embedded along the longitudinal direction of the actuator which lead to longer fibers than those used in the first type, moreover, electrodes are attached to the upper and lower surface of the actuator which serve as the part where the electric potential is applied given the electrode spacing. Both types are investigated in the following study.

Table 3.1: Material properties of the actuators and composite beam

Property	Variable	Units	Carbon Epoxy(AS4-3601)	MFC (60%)	AFC (60%)	PZT-5H	PZT-5A
Young's Modulus	E1	GPa	147	30.0	35	61	61
	E2	GPa	10.3	15.5	10.41	61	61
	E3	GPa	10.3	15.5	10.41	48	53.2
Poisson's Raito	ν12	-	0.27	0.35	0.35	0.31	0.384
	ν13	-	0.27	0.4	0.38	0.31	0.4
	ν23	-	0.54	0.4	0.38	0.31	0.4
Shear Modulus	G12	GPa	7	5.7	4.4	23.3	22.5
	G13	GPa	7	10.7	4.96	19.1	21
	G23	GPa	3.7	10.7	4.96	19.1	21
Piezoelectric Coefficients	d31	pm/V	-	-198	-260	-274	-171
	d32	pm/V	-	-198	-260	-274	-171
	d33	pm/V	-	418	540	593	374
	d15	pm/V	-	-	-	741	584
	d24	pm/V	-	-	-	741	584
Thickness	t	m	0.000127/ply	0.0003	0.0003	0.0003	0.0003

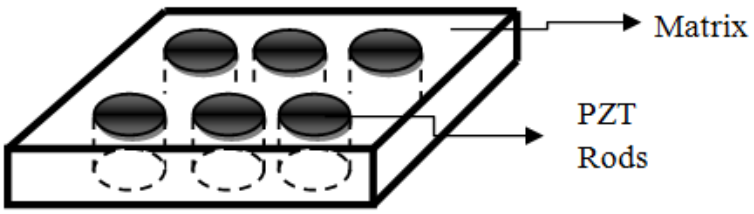

Figure 3.12: Piezoelectric fiber composite with fibers embedded through the matrix thickness

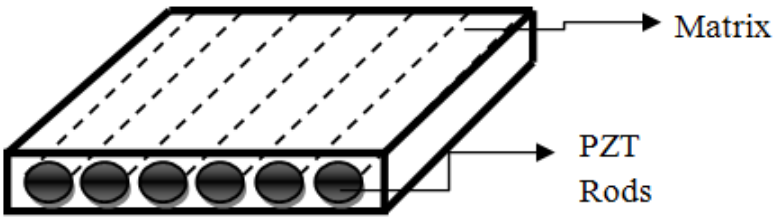

Figure 3.13: Piezoelectric fiber composite with fibers embedded through the matrix length

The composite laminate is made of Carbon /Epoxy AS4 (3501-6) with symmetric laminates [Actuator/90/45/-45/0]s. The finite element software Abaqus is used to develop a 3D model in order to predict the response of a simply supported composite beam and a cantilever beam subjected to a voltage difference across the actuators. A schematic of the composite beam and the dimensions used is shown in Figure 3.14 and Figure 3.15.

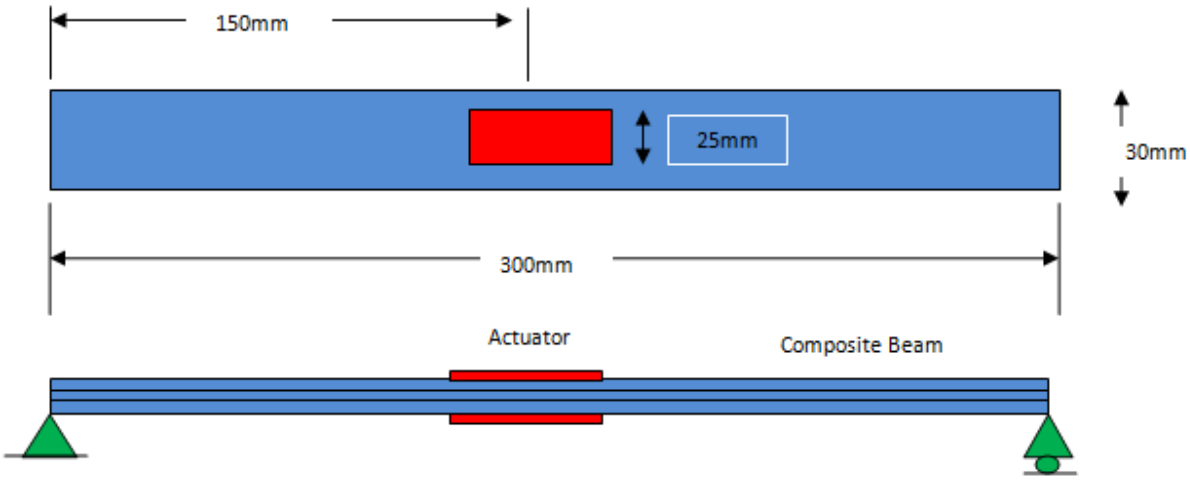

Figure 3.14: Schematic of a simply supported composite beam with actuator attached

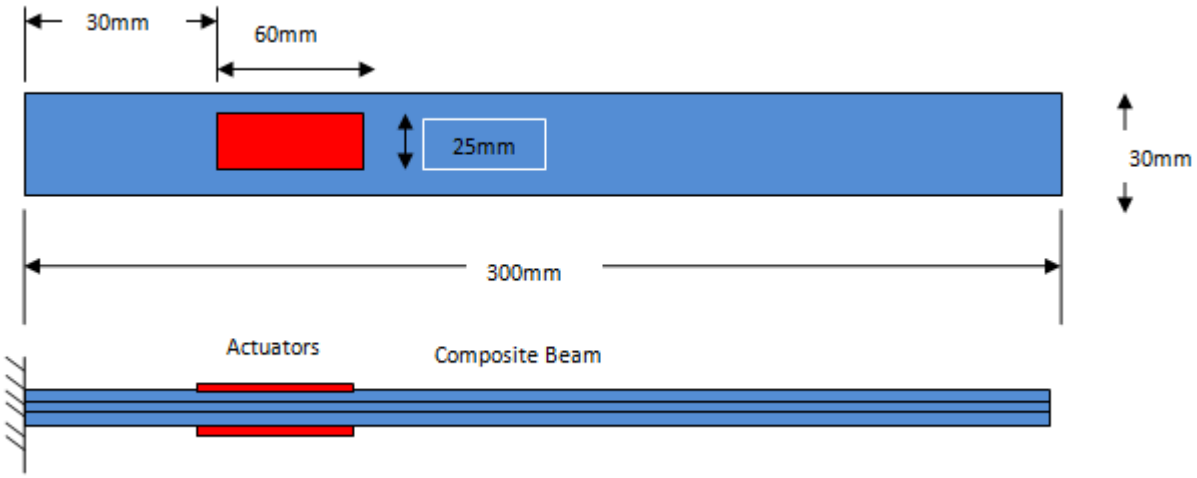

Figure 3.15: Schematic of a cantilever composite beam with actuator attached

Figure 3.16 shows the response of a simply supported composite beam subjected to a 1.25 MV/m electric field considering the first type of the piezoelectric fiber actuators and both PZT actuators mentioned previously. The maximum displacement (0.76mm at the mid length of the beam) corresponding to a 0.253% strain is obtained by using PZT-5H because of its high piezoelectric coefficient through the actuation direction while the MFC actuator gave the least displacement value since it has a low piezoelectric coefficient in the actuation direction compared to AFC. The response of the same composite beam subjected to a 2.5 MV/m electric field is shown in Figure 3.17. By applying a higher voltage difference through the actuators, a higher deflection is obtained, where; in this case the maximum displacement is 1.58mm corresponding to a 0.527% strain by using a PZT-5H actuator and the minimum displacement is obtained by using the MFC actuator for the same reasons mentioned previously.

Figure 3.18 and Figure 3.19 show the response of a cantilever composite beam subjected to a 1.25MV/m, 2.5MV/m electric field considering the first type of the piezoelectric fiber actuators and both PZT actuators mentioned previously. The max displacement obtained is 2.2mm, 4.7mm (0.733%, 1.57% strain) by using PZT-5H in both cases respectively. It is evident that the composite laminates with cantilever beam boundary conditions have larger deflections than the simply supported boundary conditions for any applied voltage considered. Figure 3.20 shows the response of a simply supported composite beam subjected to a 1.25 MV/m electric field but this time, the second type piezoelectric fiber actuators are used in addition to both PZT actuators mentioned previously.

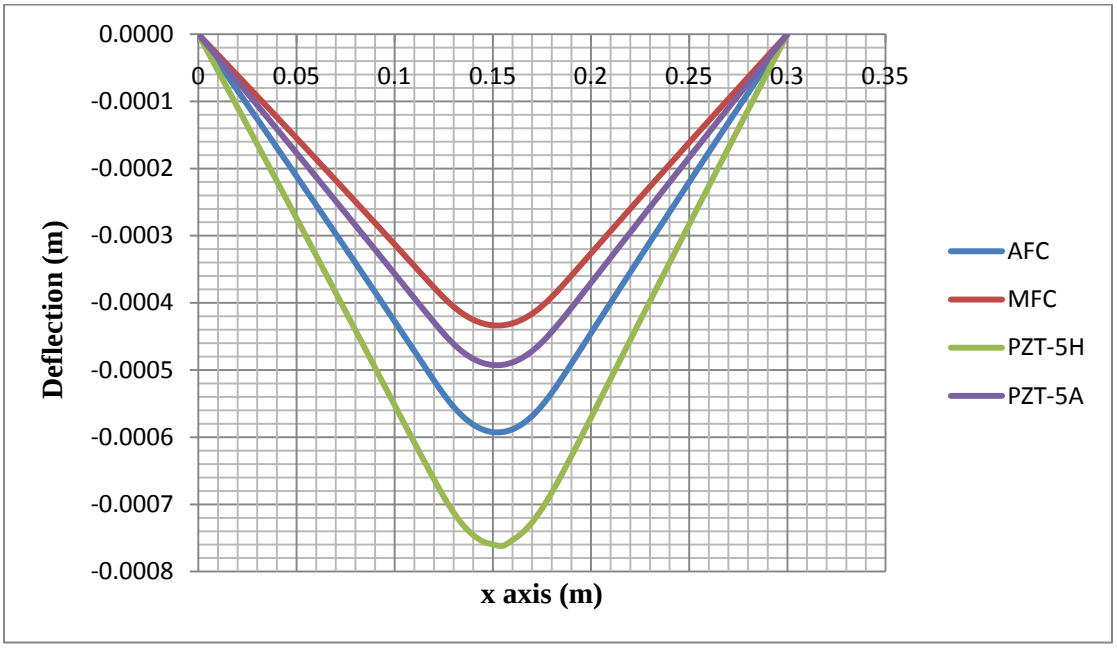

Figure 3.16: Predicted steady-state deflection of a simply supported composite beam subjected to different actuators under 1.25MV/m electric field

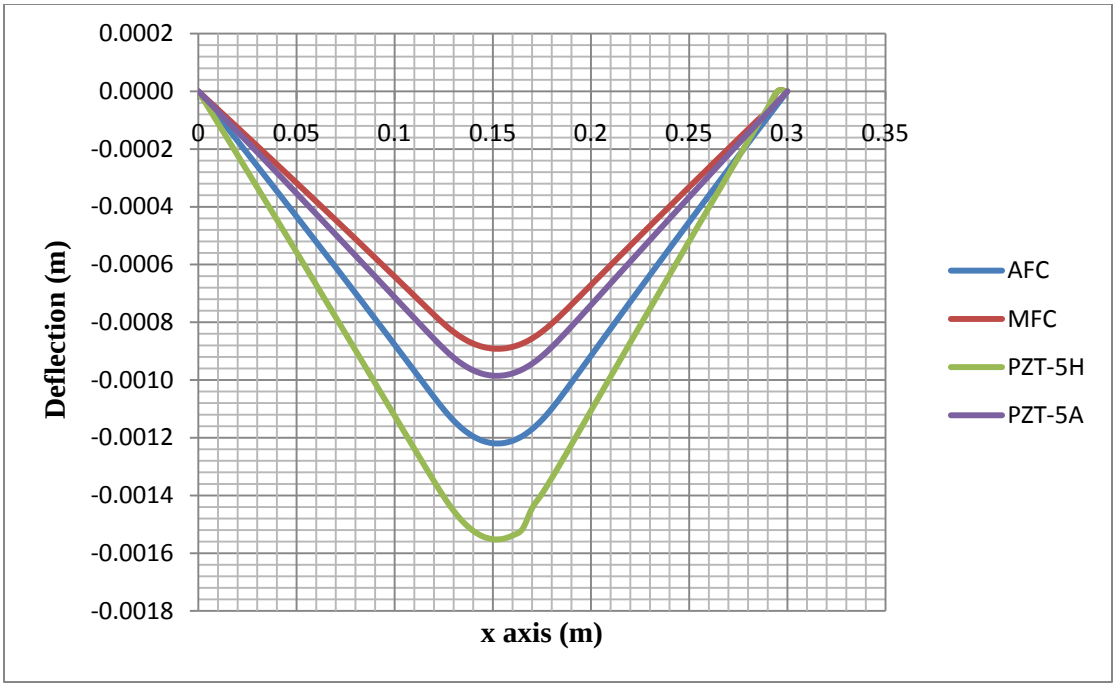

Figure 3.17: Predicted steady-state deflection of a simply supported composite beam subjected to different actuators under 2.5MV/m electric field

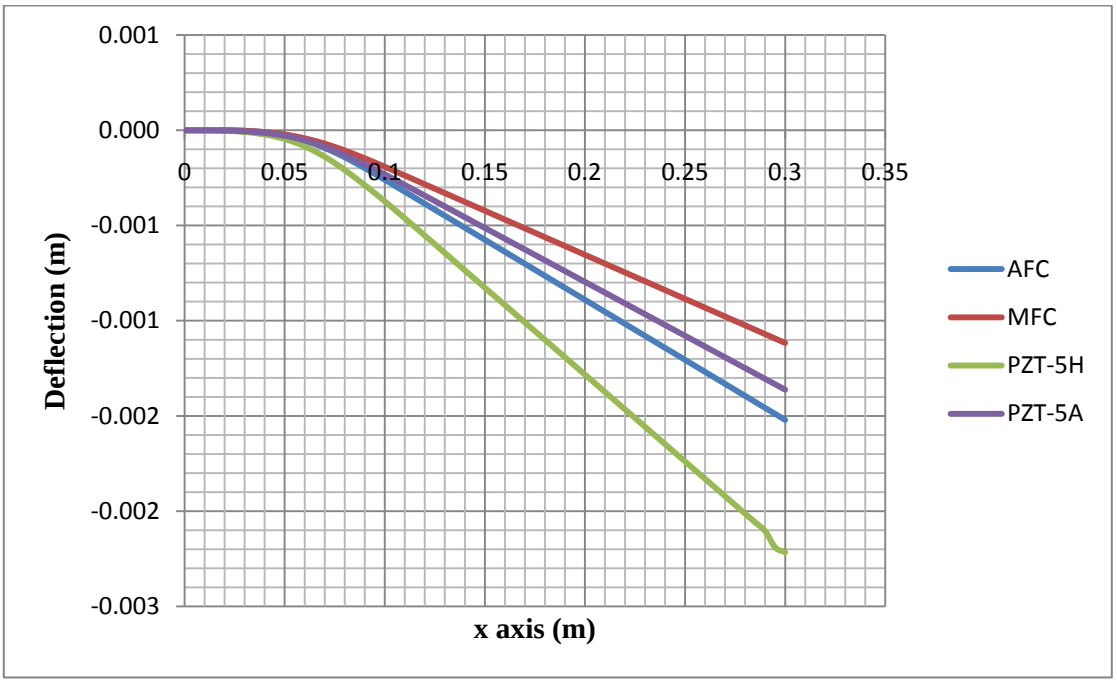

Figure 3.18: Predicted steady-state deflection of a cantilever composite beam subjected to different actuators under 1.25MV/m electric field

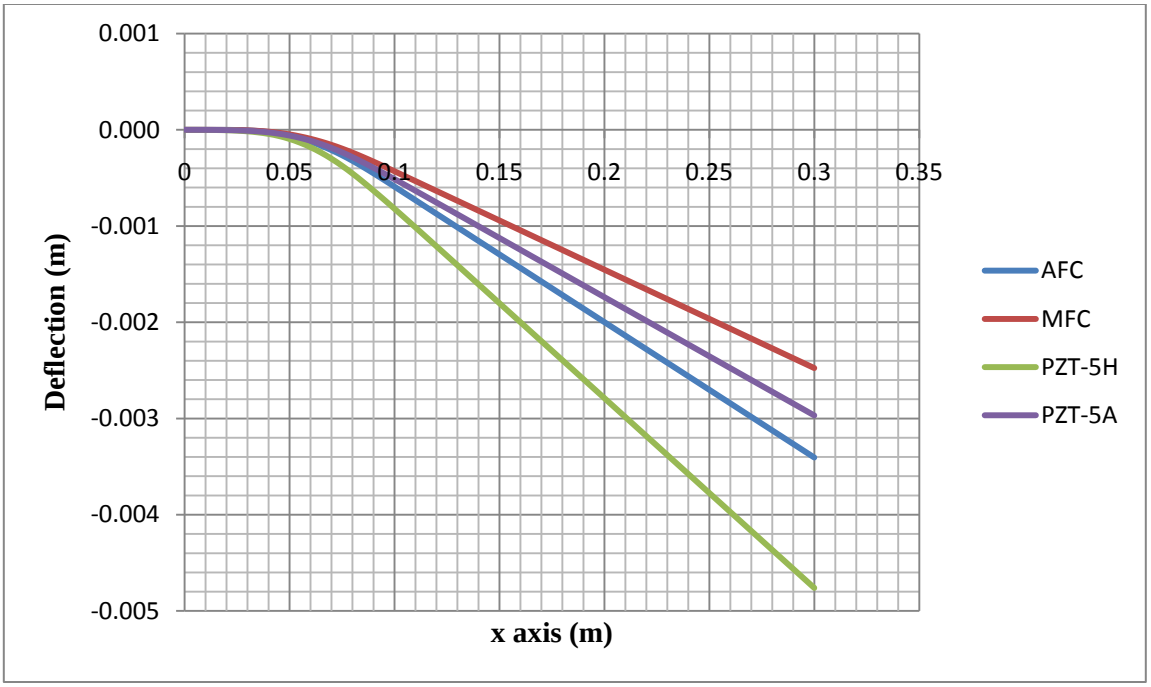

Figure 3.19: Predicted steady-state deflection of a cantilever composite beam subjected to different actuators under 2.5MV/m electric field

The maximum displacement (1.2mm at the mid length of the beam) corresponding to a 0.4% strain is obtained by using the AFC actuator. In this case, both piezoelectric fiber composites are actuated along the longitudinal direction through the electrodes that are attached to the upper and lower parts of the actuator and both have higher piezoelectric coefficients than the PZT actuators in this case. The lowest displacement obtained (0.5mm, 0.17% stain) in this case is given by using PZT-5A actuator that has the least piezoelectric coefficients. The response of the same composite beam subjected to a 2.5 MV/m electric field is shown in Figure 3.21. By applying a higher voltage difference through the actuators, a higher deflection is obtained, where; in this case the maximum displacement is 2.4mm corresponding to a 0.8% strain by using

the AFC actuator and the minimum displacement is obtained by using the PZT-5A actuator for the same reasons mentioned previously. Figure 3.22 and Figure 3.23 show the response of a cantilever composite beam subjected to a 1.25 MV/m and 2.5MV/m electric field across the different actuators. The max displacement obtained is 4.3mm, 8.2mm (1.4%, 2.73% strain) by using the AFC actuator in both cases respectively. AFC and MFC have the advantage of having a more flexible behavior caused by embedding piezoelectric materials in the form of fibers into a polymer matrix, unlike the brittle and inflexible nature of PZT. It can be concluded that by using either type of the actuators presented, the deflection produced can be used to counter react external stimuli's that are applied to the composite beam, also, since all the actuators are suitable in overcoming the deflection of the beam; it is more convenient to use AFCs and MFCs due to their advantages of giving higher deflection, yet, more flexible and can sustain higher electric fields.

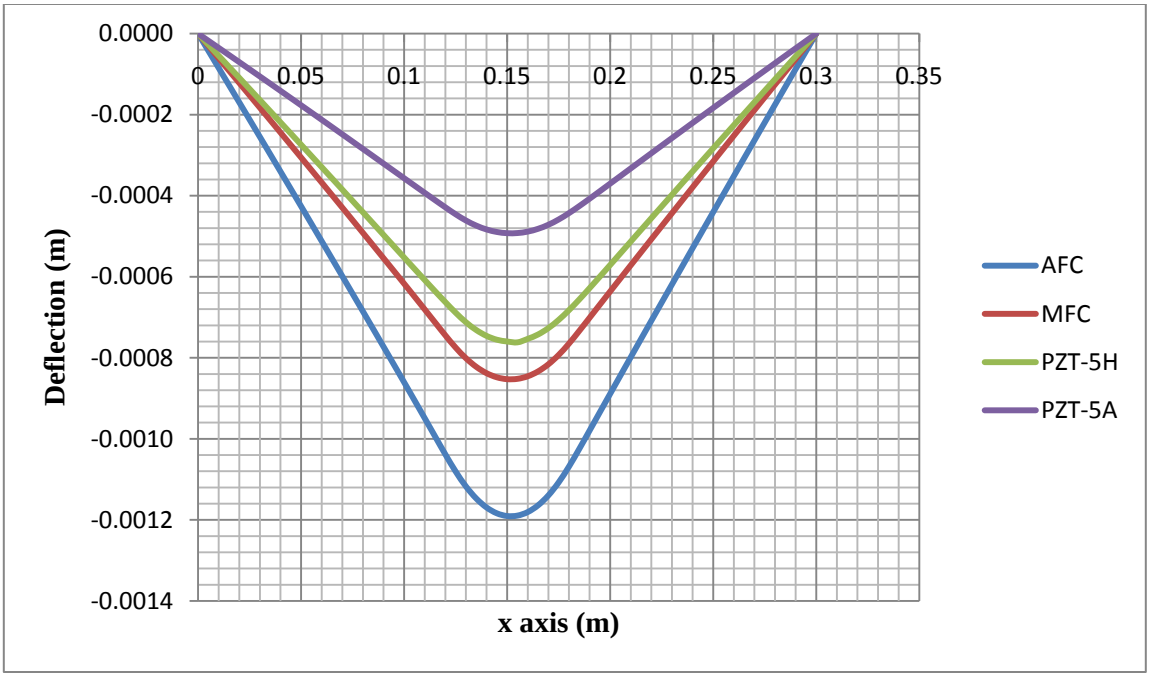

Figure 3.20: Predicted steady-state deflection of a simply supported composite beam subjected to different actuators under 1.25MV/m electric field

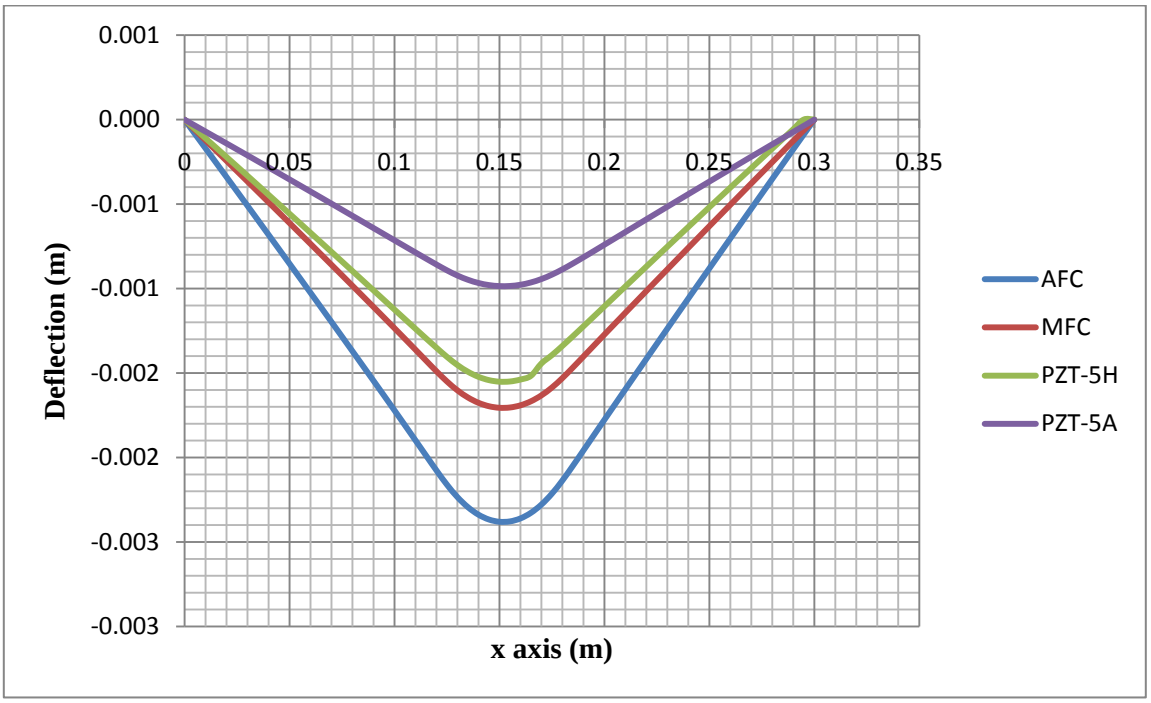

Figure 3.21: Predicted steady-state deflection of a simply supported composite beam subjected to different actuators under 2.5MV/m electric field

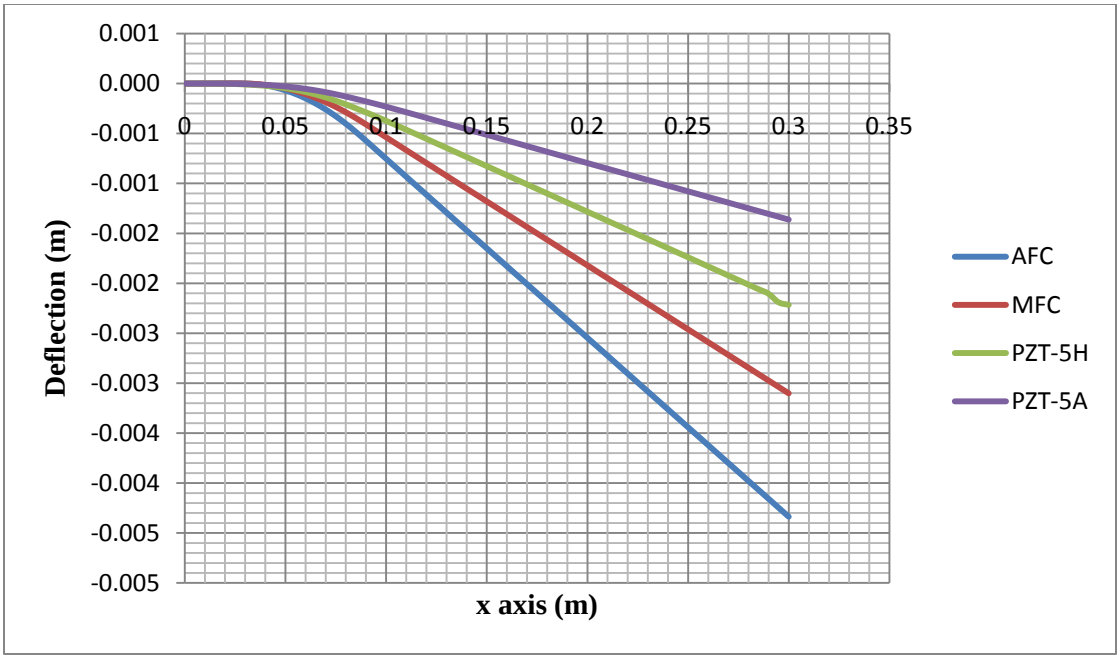

Figure 3.22: Predicted steady-state deflection of a cantilever composite beam subjected to different actuators under 1.25MV/m electric field

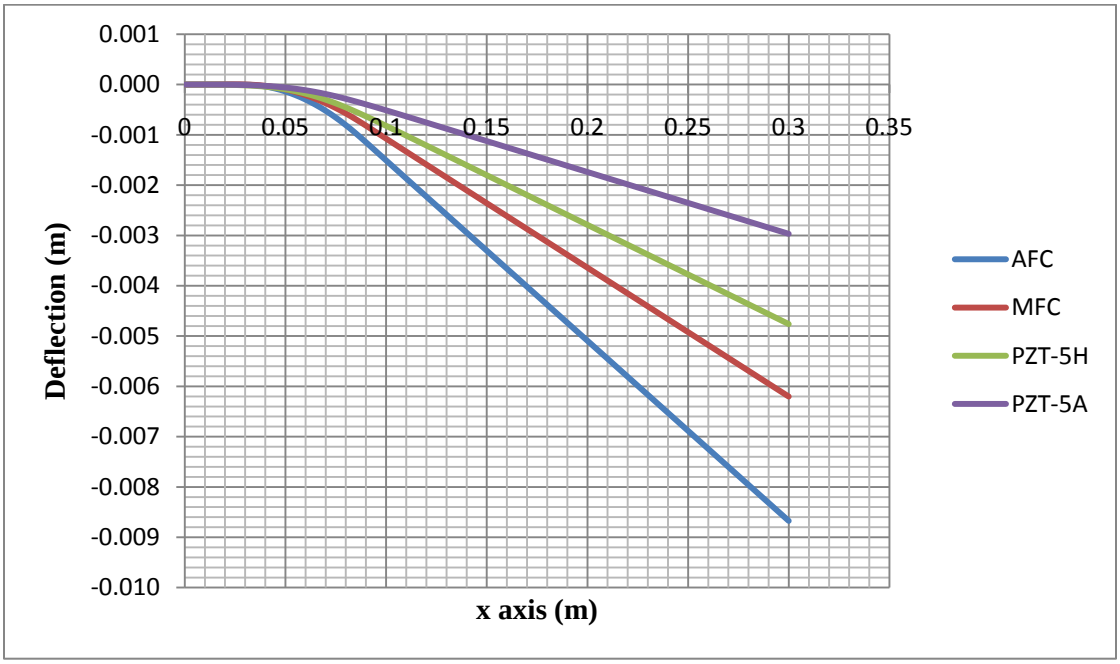

Figure 3.23: Predicted steady-state deflection of a cantilever composite beam subjected to different actuators under 2.5MV/m electric field

In order to further verify the results obtained from the previous study, we define an important property used in piezoelectric materials called the energy density which defines the maximum energy per unit volume that can be produced by the piezoelectric device.

In the case where the PFC actuators had longitudinal fibers embedded in the matrix and actuated through the longitudinal direction. The desired extension in this case is parallel to the actuation direction. Therefore, the 33 mode of the piezoelectric material is utilized in these applications. The volumetric energy density in this case can be given as [43]

$$E_v = \frac{1}{2} E_3 {d_{33}}^2 \xi_1^2 \tag{3.54}$$

The energy density is an important figure of merit when comparing different types of piezoelectric materials and when comparing different materials with one another. It is also an intrinsic property of the material since it does not depend on the geometry. At equivalent electric fields, one can form a figure of merit, $\frac{1}{2} E_3 {d_{33}}^2$ and assess the relative ability of different materials to do mechanical work. A higher value of $\frac{1}{2} E_3 {d_{33}}^2$ indicates that a material can perform more mechanical work at the same electric fields, but this does not mean that it is necessarily a better material in every aspect since a material may require much larger voltages or may not work over a large temperature range, and so on, but it does indicate that the material has better intrinsic properties as an electromechanical actuator.

In the case where both PZT and the PFC actuators which had embedded fibers through the matrix thickness encompass the operating mode along the axis of polarization defined as the 3 axis of the material. The poling direction of the piezoelectric material is parallel with the thickness direction of the piezoelectric layer and the desired extension is perpendicular to the poling direction. Therefore, the 31 mode of the piezoelectric material is utilized in these applications. The energy density function in this case is defined as [39]

$$E_v = \frac{1}{2} E_1 d_{13}^{\ 2} \xi_3^{\ 2} \tag{3.55}$$

The reduction in volumetric energy density in this case is due to the fact that d_{13} is usually a factor of 2 or 3 lower than d_{33}. The reduction in strain coefficient in the 13 direction is offset somewhat by the increase in elastic modulus in the 1 direction. Table 3.2 shows the energy density function for the different actuators used in the shape control of the composite structure under an electric field 1.25MV/m. It can be observed that the energy density obtained from the 31 mode of the piezoelectric material had the largest value when using a PZT-5H actuator while an AFC actuator provides the largest in the 33 mode.

Table 3.2 Energy density of different types of piezoelectric materials for different actuation modes at an electric field of 1.25 MV/m

Actuator	d_{33} (pm/V)	d_{31} (pm/V)	E_1 (GPa)	E_3 (GPa)	E_v (kJ/m^3) (33 mode)	E_v (kJ/m^3) (31 mode)
PZT-5H	593	274	61	48	-	2012.5
PZT-5A	374	171	61	53.2	-	783.84
MFC	418	198	30	15.5	2115.8	516.8
AFC	540	260	35	10.41	2371.5	1039.7

The Effect of ply orientation on the transverse deflection of a cantilever beam for a 1MV/m and 2MV/m electric field is shown in Figure 3.24 and Figure 3.25 respectively. It can be observed that the plies with orientation 45° have larger deflections than those for 20° for the same applied voltage. In addition, Figure 3.26 and Figure 3.27 show a comparison between two beams one with cross laminates and another having a stacking sequence $[0/45]_s$ subjected to 1MV/m and 2MV/m electric field, respectively. It can be seen that the difference is almost negligible (error = 0.2%) between the deflections of both beams. It can also be concluded from the figures that the laminates that contain 0° plies have less deflection from those with only angle plies for the same applied voltage.

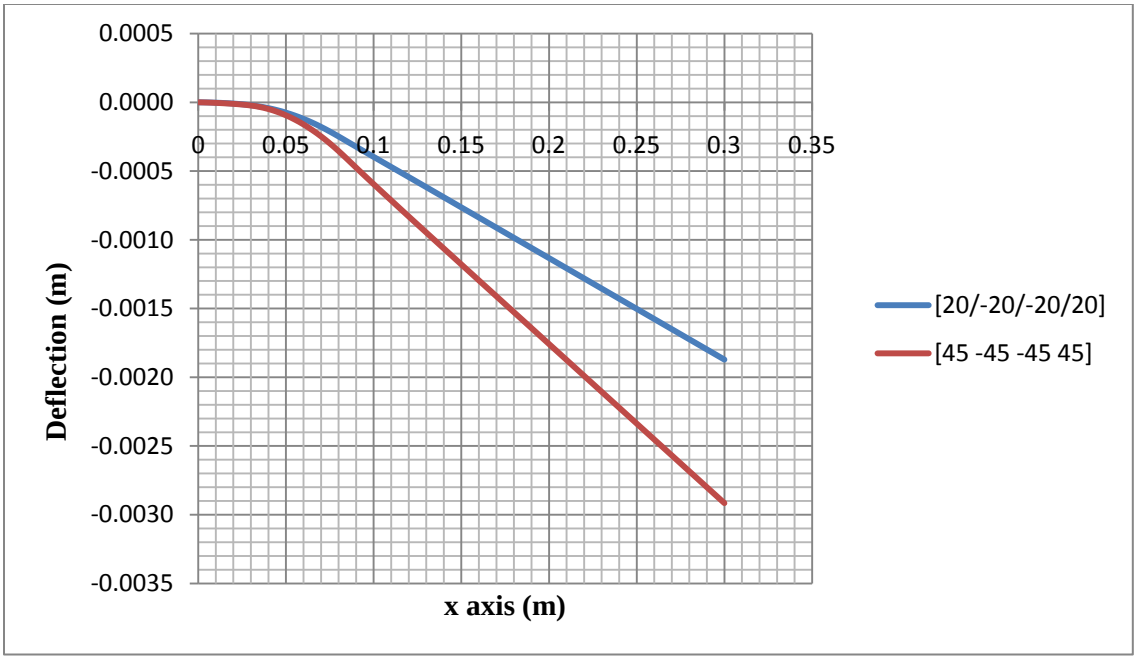

Figure 3.24: Predicted steady-state deflection for different ply orientation composite beams subjected to 1MV/m electric field

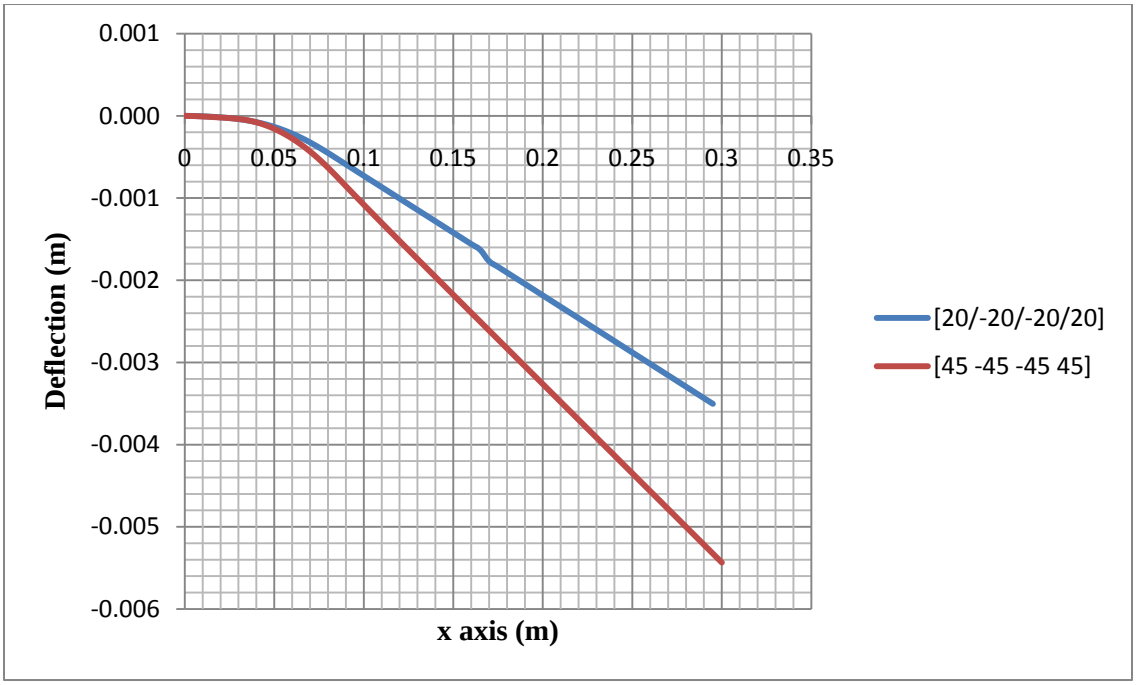

Figure 3.25: Predicted steady-state deflection for different ply orientation composite beams subjected to 2MV/m electric field

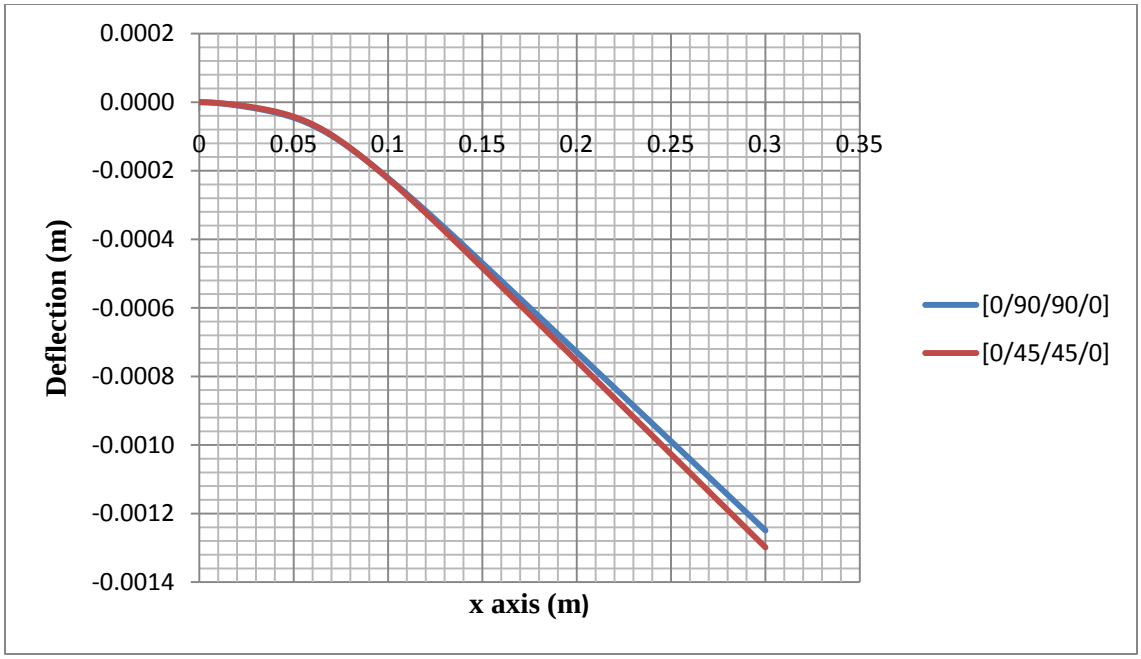

Figure 3.26: Predicted steady-state deflection for different ply orientation composite beams subjected to 1MV/m electric field

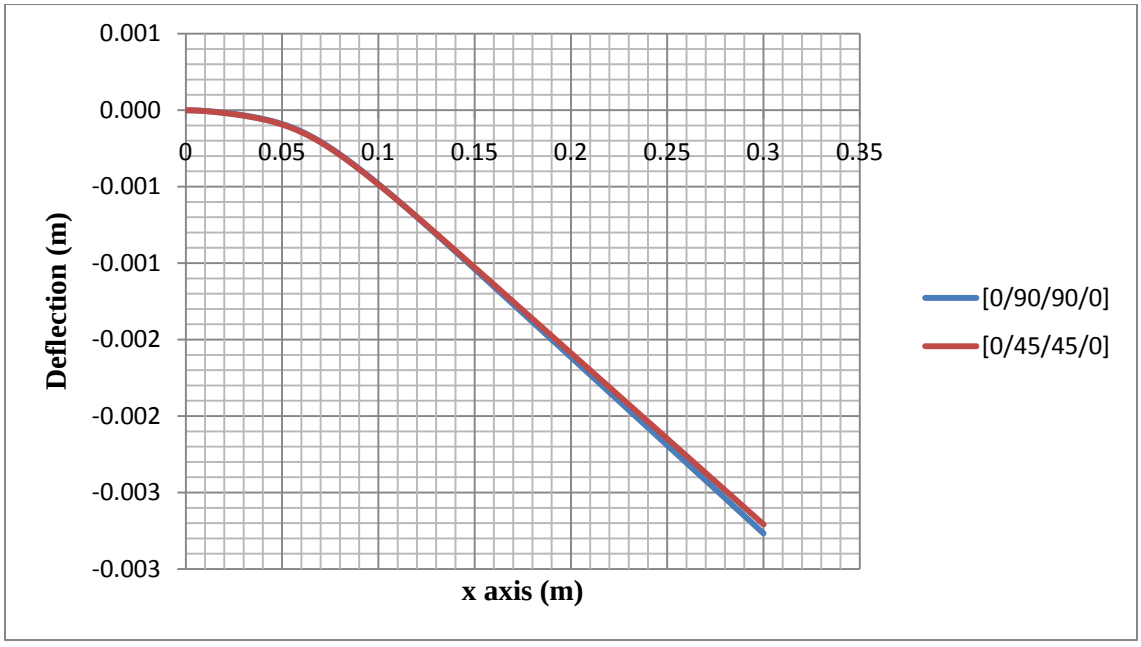

Figure 3.27: Predicted steady-state deflection for different ply orientation composite beams subjected to 2MV/m electric field

The stress distribution along the mid section of a simply supported composite beam with a stacking sequence [Actuator/0/45/-45]s for different types of actuators is calculated using Eq. (3.51-3.53) under the application of a 1kN applied at the mid-section. The stress discontinuity between each layer in the composite layup can be shown in Figure 3.28. It can be observed that a higher stress discontinuity is caused by using MFC and AFC due to their lower young's modulus compared to PZT. In addition, the effect of applying a voltage difference to the actuator along the ply thickness can be seen in Figure 3.29, Figure 3.30 and Figure 3.31 for AFC, MFC and PZT-5H actuators respectively. It can be observed that by increasing the voltage difference along the actuator the axial stress in each ply will increase leading to higher stress concentration between the host structure and the actuator which may lead to delamination as show in Figure 3.32. This phenomenon has been known to be one of the major reasons for failure in smart structures. Delamination consists in the separation of the plies of a composite laminate which leads to a significant reduction in the compressive load-carrying capacity of a composite structure. The stress gradients that occur near geometric discontinuities such as ply drop-offs, stiffener terminations and flanges, bonded and bolted joints, and access holes promote delamination initiation, trigger intraply damage mechanisms, and may cause a significant loss of structural integrity [31]. This leads to alternative designs where this stress concentration can be decreased while attaining the same overall response. An alternative method used in such structures is studied which decreases such stress concentration leading to less failure probability.

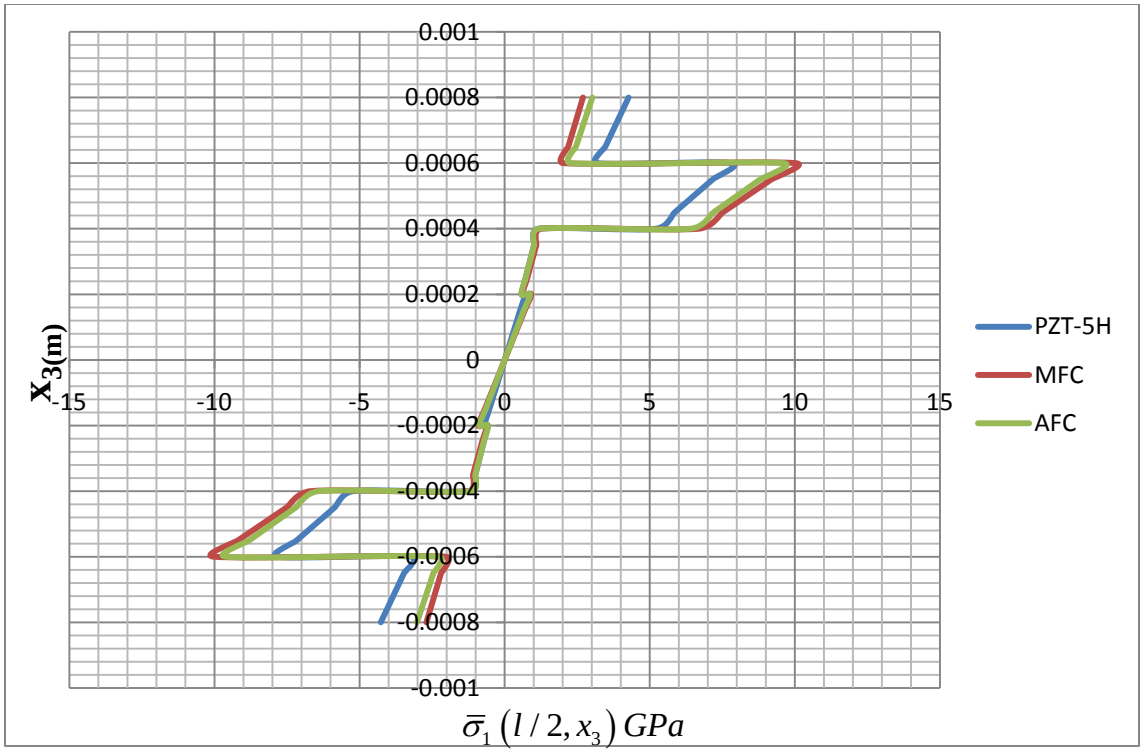

Figure 3.28: Stress distribution along the thickness of a composite beam using different actuators

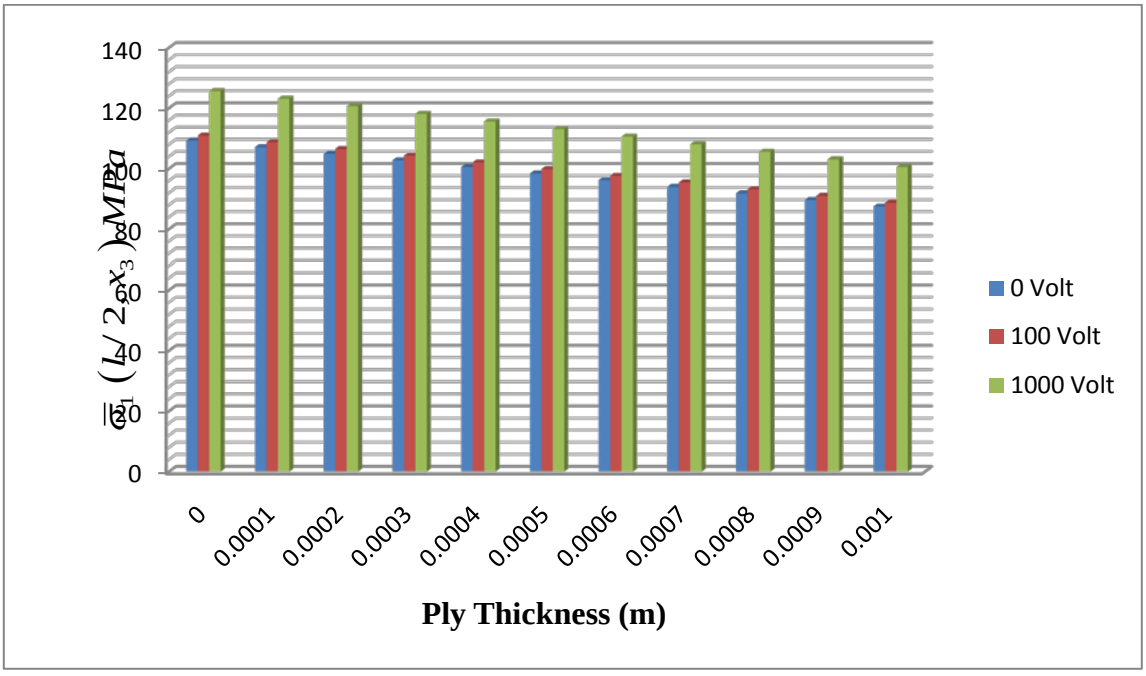

Figure 3.29: Stress distribution along the thickness of an AFC actuator for different voltage values

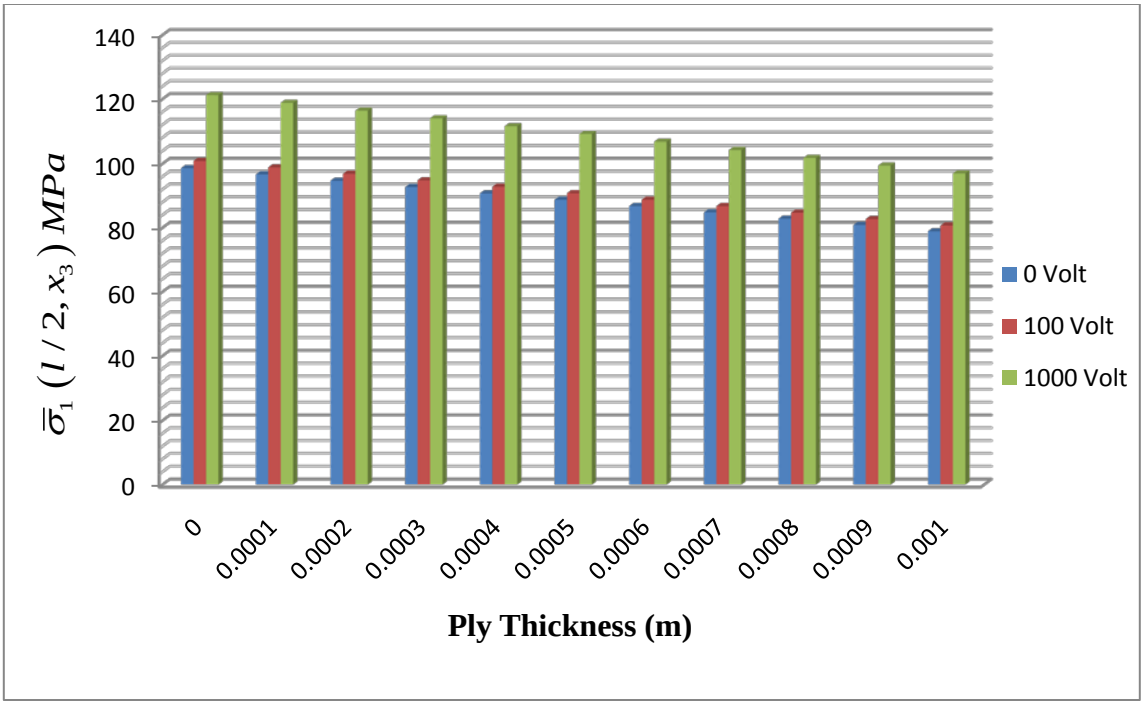

Figure 3.30: Stress distribution along the thickness of an MFC actuator for different voltage values

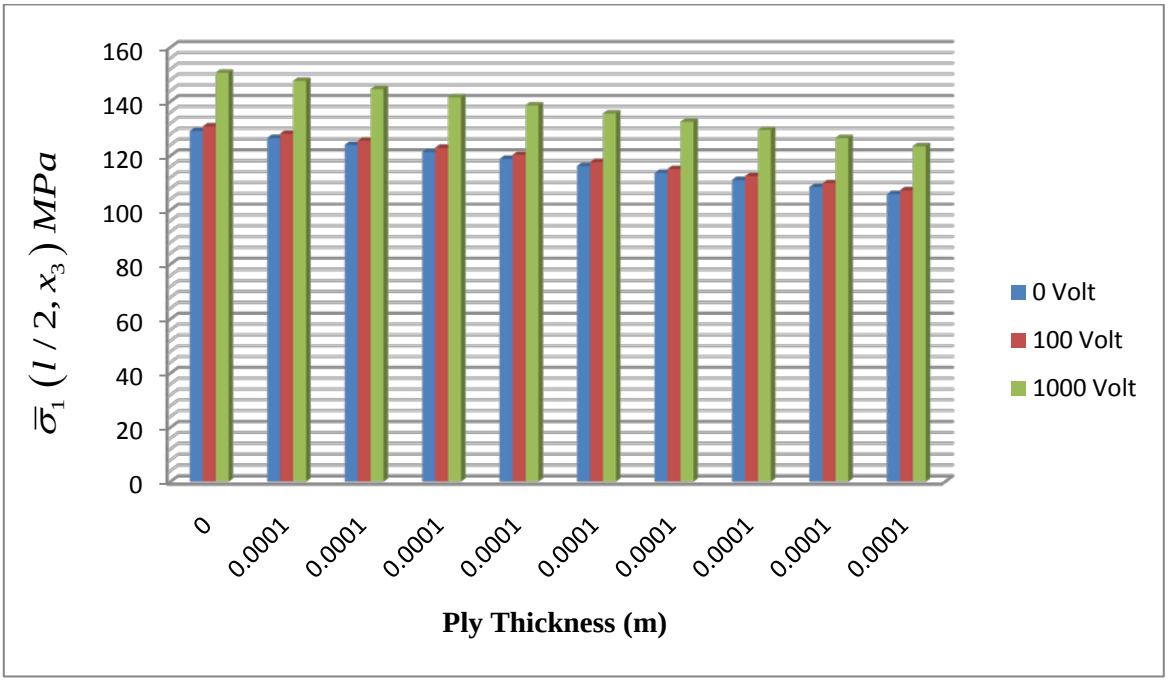

Figure 3.31: Stress distribution along the thickness of an PZT-5H actuator for different voltage values

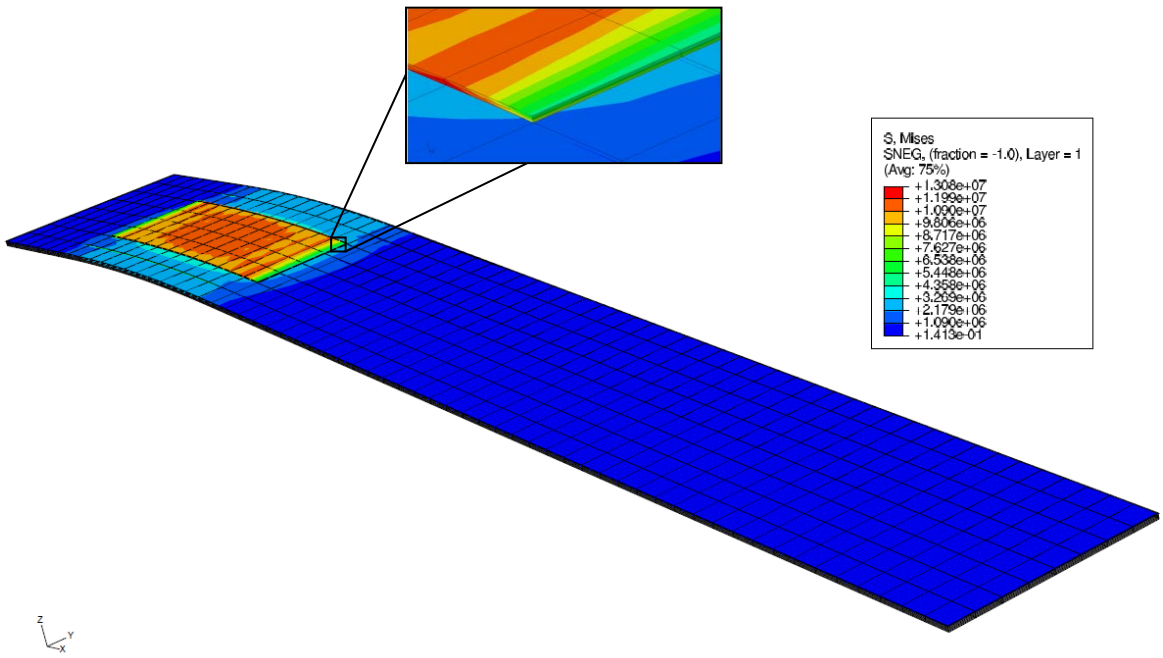

Figure 3.32: Composite laminate with PZT actuator attached

During the manufacturing process, an actuator can be incorporated into the layer by becoming part of one of the composite layers as shown in Figure 3.33, a. This could lead to enhanced behavior of the overall structure and exclude all the stress concentration that existed in the previous patched design as shown in Figure 3.34 and Figure 3.35. Figure 3.36 show the deflection of a composite beam using patched and embedded actuators both made of carbon epoxy AS4 with the same stacking sequence [0/45/45/0]. It can be observed that other than excluding the stress concentration in the embedded design, the deflection is larger than the patched case for both PZT-5H and MFC actuators. This is because the geometry discontinuity between the actuator and the composite laminate is absent and the in-plane stress is continuously distributed in the

laminate. Another possible design could be by using a modified design of the actuators as shown in Figure 3.33, b. This gives similar deflection values to the patched case while decreasing the stress concentration.

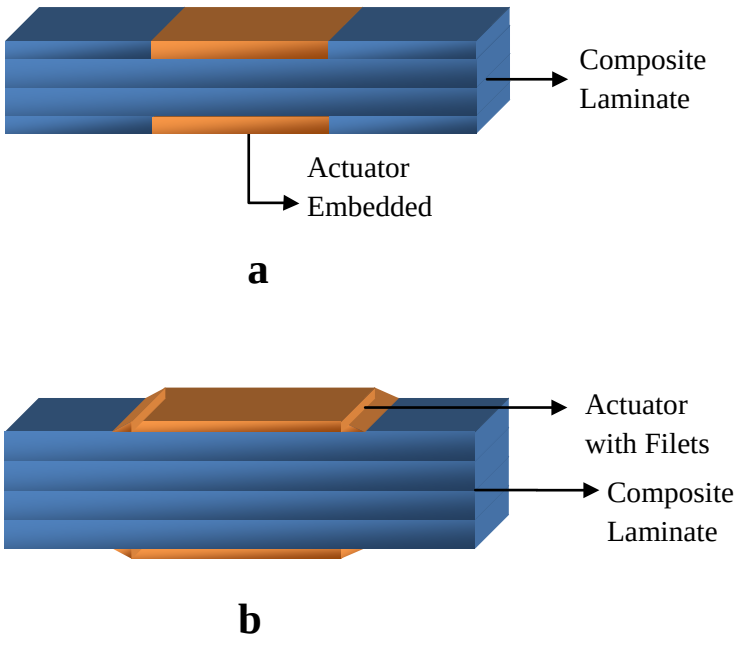

Figure 3.33: (a, b). Schematic for different designs methods used to patch the actuators on the host structure

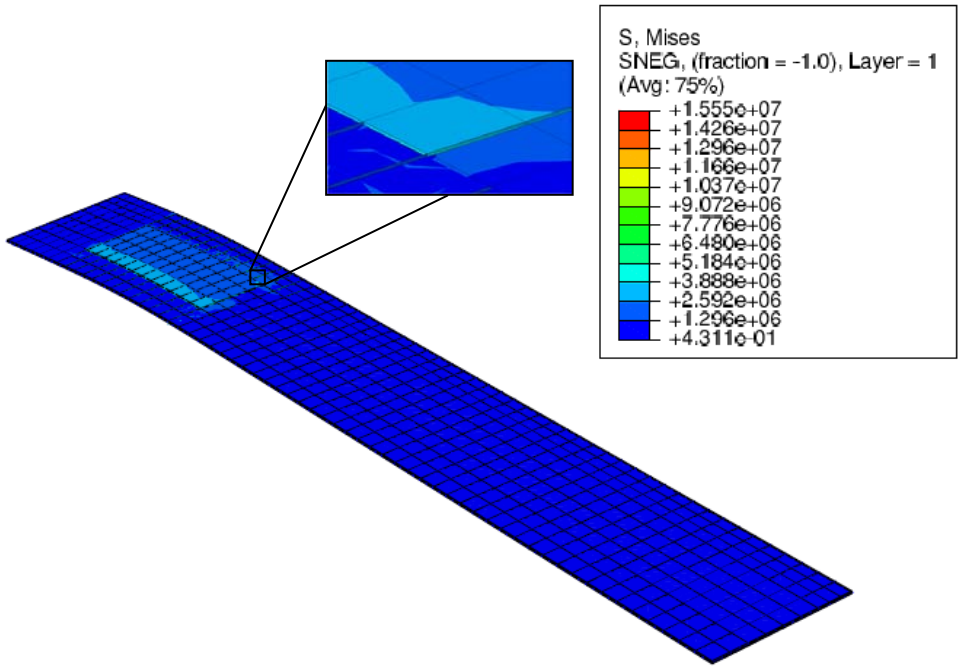

Figure 3.34: Composite laminate with PZT actuator embedded into the first composite layer

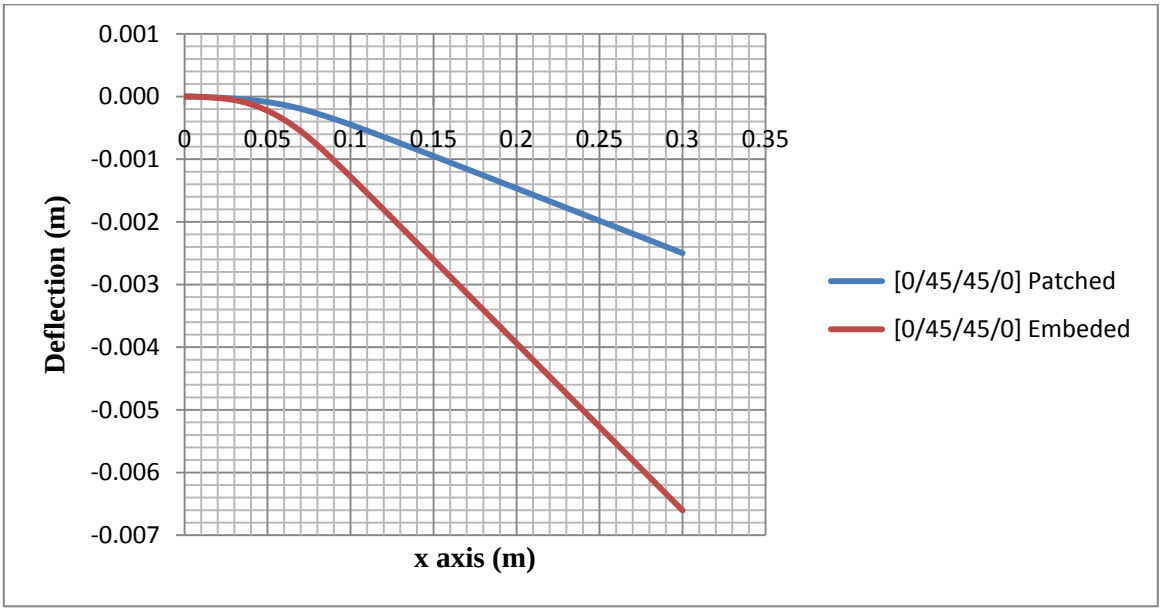

Figure 3.35: Predicted steady-state deflection of a composite beam using embedded and patched PZT-5H actuator under 1MV/m

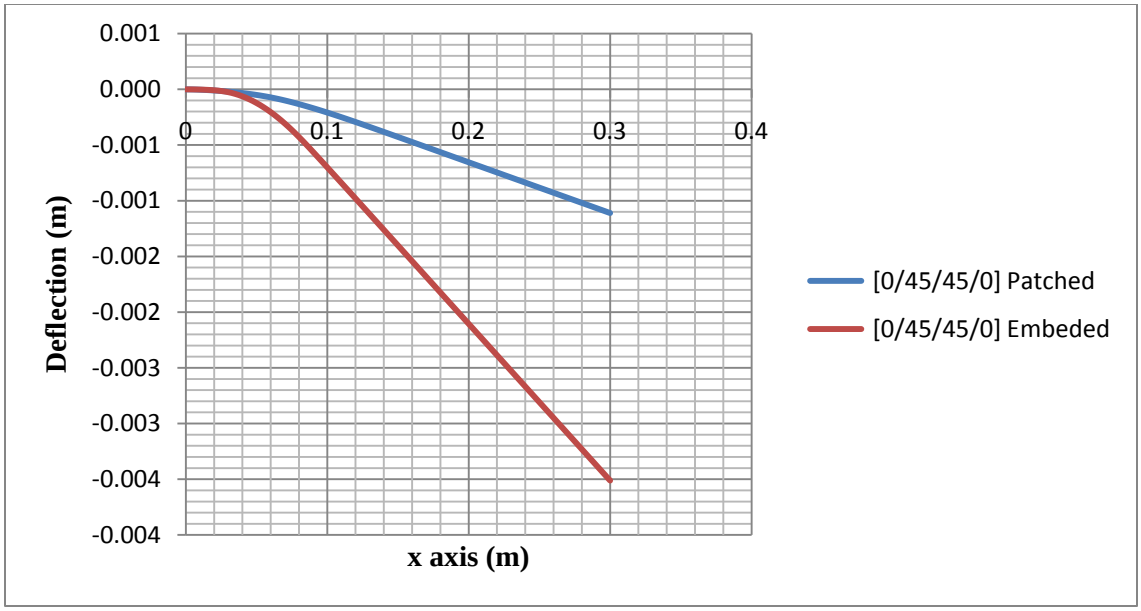

Figure 3.36: Predicted steady-state deflection of a composite beam using imbedded and patched MFC actuator under 1MV/m

CHAPTER IV

FAILURE ANALYSIS OF SMART LAMINATED COMPOSITES

The following chapter presents failure analysis of composite laminates including hygrothermal and electric effects using the first-ply failure (FPF) and ultimate laminate failure (ULF) criteria of composite laminates in order to predict the failure stress and mode of a composite laminate under a uniaxial and biaxial loading. We focus on analyzing response of thin laminated composites such that the effect of transversely shear deformation on the overall performance of composite is less significant. Thus, the in-plane components of stress and strain are the primary parameters in determining bending of laminated composites. We start by analyzing failure in smart laminated composites due to uniaxial and biaxial loading, in which the composites are under constant stain/deformation through their thickness, followed by failure analysis under bending, where non-uniform stress/strain occur in the composite body. Various commonly known macroscopic failure criteria including Tsai-Hill, Tsai Wu, maximum stress and maximum strain are used. A detailed sample calculation based on the Classical Lamination Theory (CLT) for Carbon/Epoxy (AS4/3501-6) laminate with stacking sequence [90/45/-45/0]s under uniaxial and biaxial loading is introduced using both the FPF and ULF criteria's. The results obtained from the uniaxial case were compared with experimental data available in literature; moreover, a finite element model is implemented and compared with the analytical results.

4.1 Review of Failure Theories

When a component is subject to increasing loads it eventually fails. It is comparatively easy to determine the point of failure of a component subject to a single tensile force. The ultimate data on the material identifies this strength. However, when the material is subject to a number of loads in different directions some of which are tensile and some of which are shear, then the determination of the point of failure is more complicated. When dealing with composite materials, several theories have been proposed by extending and adapting isotropic failure theories to account for the anisotropy in stiffness and strength of the composite. Lamina failure theories can be classified in the following three groups [40]:

- Limit or non-interactive theories, in which specific failure modes are predicted by comparing individual lamina stress or strains with corresponding strengths or ultimate strains, for example maximum stress and maximum strain theories have no interaction among different stress components on failure is considered.
- Interactive theories (the Tsai-Hill and the Tsai-Wu theories) in which all stress components are included in one expression (failure criterion). Overall failure is predicted without reference to particular failure modes.
- Partially interactive or failure mode based theory (the Hashin-Rotem) where separate criteria are given for fiber and interfiber failures.

4.1.1 Maximum Stress Theory

The theory was adapted for maximum stress to composites under plane stress conditions and was used to predict the off-axis strength of a unidirectional lamina as a

function of fiber orientation by three different curves corresponding to three different failure modes. According to the maximum stress theory, failure occurs when at least one stress component along one of the principal material axes exceeds the corresponding strength in that direction. The strength values are obtained for each certain material from their own charts. It should be noted that in the case of shear stress and strength referred to the principle material axes, the sign of the shear stress indicates the shearing direction and only absolute values needed be used for failure criteria. There are three different modes of failure that can be classified as:

1. Fiber failure (tensile and compressive).
2. In-plane shear interfiber failure.
3. Transverse normal stress interfiber failure (tensile and compressive).

The maximum stress theory is more applicable for the brittle (For brittle materials, it is quite reasonable to assume linear elastic behavior for predicting the overall deformation of the material up to the ultimate strength) modes of failure of the material, closer to transverse and longitudinal tension, and does not take into account any stress interaction under a general biaxial state of stress. So the lamina is considered to be failed if the following is violated

$$\begin{aligned} -(\sigma_1^C)_{ult} < \sigma_1 < (\sigma_1^T)_{ult} \\ -(\sigma_2^C)_{ult} < \sigma_2 < (\sigma_2^T)_{ult} \\ -(\tau_6^C)_{ult} < \tau_6 < (\tau_6^T)_{ult} \end{aligned} \tag{4.1}$$

Where $\sigma_1, \sigma_2, \tau_6$ are the stresses along the principal material axes.

4.1.2 Maximum Strain Theory

According to the maximum strain theory failure occurs when at least one of the strain components along the principle material axes exceeds the corresponding ultimate strain in that direction.

$$\begin{aligned} -(\varepsilon_1^C)_{ult} < \varepsilon_1 < (\varepsilon_1^T)_{ult} \\ -(\varepsilon_2^C)_{ult} < \varepsilon_2 < (\varepsilon_2^T)_{ult} \\ -(\gamma_6^C)_{ult} < \gamma_6 < (\gamma_6^T)_{ult} \end{aligned} \tag{4.2}$$

where $\varepsilon_1, \varepsilon_2, \gamma_6$ are the strains along the principal material axes.

The theory allows some interaction of stress components due to Poisson's ratio effect. From here, we can observe some relationship between the previous two theories. The ultimate strains can be found from the ultimate strength parameters and the elastic moduli, assuming the stress-strain response is linear until failure and loading is under load/stress control. For the maximum strain failure theory, it is not always proper to assume linear elastic behavior in predicting stress-strain response of materials as nonlinear stress-strain relations and ineleastic behaviors could be pronounced.

4.1.3 Energy Based Interaction Theory (TSAI-HILL)

Is a modified theory based on the distortional energy theory for isotropic materials, modified for the case of ductile metals with anisotropy and proposed the following form

$$A\sigma_1^2 + B\sigma_2^2 + C\sigma_1\sigma_2 + D\tau_6^2 = 1 \tag{4.3}$$

where A, B, C, D are material parameters characteristic of the current state of anisotropy and depend among the strength of the material instead of C that accounts for interaction

between normal stress σ_1 and σ_2 must be determined by means of a biaxial test. Based on the distortion energy theory they proposed that the lamina will fail if

$$\begin{aligned}&(G_2+G_3)\sigma_1^2+(G_1+G_3)\sigma_2^2+(G_1+G_2)\sigma_3^2-2G_3\sigma_1\sigma_2-2G_2\sigma_1\sigma_3-\\&2G_1\sigma_1\sigma_3+2G_4\tau_4^2+2G_5\tau_5^2+2G_6\tau_6^2<1\end{aligned} \tag{4.4}$$

The components G_1 - G_6 of the strength criteria depend on the failure strength. One disadvantage is that it does not distinguish directly between tensile and compressive strengths. For a two dimensional state of stress the equation becomes

$$\left[\frac{\sigma_1}{(\sigma_1^T)_{ult}}\right]^2-\left[\frac{\sigma_1\sigma_2}{(\sigma_1^T)^2_{ult}}\right]+\left[\frac{\sigma_2}{(\sigma_2^T)_{ult}}\right]^2+\left[\frac{\tau_6}{(\tau_6)_{ult}}\right]^2<1 \tag{4.5}$$

Unlike the maximum strain and maximum stress failure theories, the Tsai-Hill failure theory considers the interaction among the three unidirectional lamina strength parameter. The Tsai-Hill failure theory does not distinguish between the compressive and tensile strengths in its equation. This can result in underestimation of the maximum loads that can be applied when compared to other failure theory. Tsai-Hill failure theory underestimates the failure stress because the transverse strength of a unidirectional lamina is generally much less than its transverse compressive strength.

4.1.4 Interactive Tensor Polynomial Theory (TSAI-WU)

This theory is capable of predicting strength under general states of stress for which no experimental data are available. It uses the concept of strength tensors which allows for transformation from one coordinate system to another. It also has the capability to account for the difference between tensile and compressive strengths. For a

two dimensional state of stress (σ_1, σ_2, τ_6) the criterion is reduced to the most familiar form

$$f_1\sigma_1 + f_2\sigma_2 + f_{11}\sigma_1^2 + f_{22}\sigma_2^2 + f_{66}\tau_6 + 2f_{12}\sigma_1\sigma_2 = 1 \qquad (4.6)$$

f_1, f_2, etc are strength tensors of second, fourth and higher orders. f_{12} is a function of the basic strength parameters plus the equal biaxial strength. The Tsai-Wu failure criterion has several desirable features; it is operationally simple and readily amenable to computational procedures. Like the Tsai- Hill theory, it is expressed in terms of a single criterion, instead of six sub criteria required in the maximum stress and max strain theories. The stress interaction terms can be treated as independent material properties determined by appropriate experiments, unlike the Tsai-Hill theory where the interaction terms are fixed as functions of the other terms. The theory, through its linear terms accounts for the difference between tensile and compressive strengths. In the classical lamination theory, stress-strain or load-deformation relations were developed for multidirectional laminates. It was shown how the laminate deformation can be fully described in terms of the reference plane strains and the curvatures, from which the strains can be obtained at any through the thickness location of the laminate. It was pointed out that, whereas strains are continuous through the thickness, stresses can be discontinuous from layer to layer, depending on the material properties and orientation of the layers. Failure analysis of a laminate is much more complex than that of a single lamina. The stresses in the individual laminae are fundamental and control failure initiation and progression in the laminate. Failure of a lamina does not necessarily imply total failure of the laminate, but is only the beginning of an interactive failure process.

The purpose of the lamina failure criterion is to determine the stress and mode of failure of a unidirectional composite or lamina in a state of combined stress. The existing lamina failure criteria's that are considered in this study are basically phenomenological in which detailed failure processes are not described (macromechanical). Further, they are all based on linear elastic analysis. The majority of the lamina failure criteria were developed for two-dimensional stress states in orthotropic materials. Some of the failure criteria's, such as the Tsai-Wu criterion which is a completely general tensor polynomial failure equation, have reduced forms in order to utilize two strength properties for two-dimensional stress states. In this study, only such 2-D criteria are included. The in-plane principal strengths in a composite system are denoted as follows; F_{1t}, F_{1c} are the tensile and compressive strengths, respectively, in fiber direction, F_{2t}, F_{2c} are the tensile and compressive strengths, respectively, in transverse direction and F_6 is the shear strength. For a strain based analysis, the corresponding failure strains are denoted as F^e_{1t}, F^e_{1c}, F^e_{2t}, F^e_{2c}, F^e_6. In this study, the in-plane principal strengths of the composite laminate are considered not the strain based strengths.

4.2 Types of Failure

Failure in a laminate may be caused by failure of individual laminae or plies within the laminate (intralaminar failure). Failure of a laminate may be defined as the initial failure or the ultimate failure, depending on the degree of conservatism applied. In the first definition, called the first ply failure (FPF), a laminate is considered failed when the first layers (or group of layers) fail. This is determined by conducting a stress analysis of the laminate under the given loading condition, determining the state of stress

in each individual layer, and assessing the strength of each layer by applying a selected failure criterion. This assumes that a layer, or lamina, within the laminate has the same properties and behaves in the same manner as an isolated unidirectional lamina. This approach is conservative, but it can be used with low safety factors. The second definition which is known as the ultimate laminate failure (ULF), there is no generally accepted definition of what constitutes such failure. It is generally accepted that a laminate is considered failed when the maximum load level is reached. The determination of the ULF requires an iterative procedure taking into account the damage progression in the various plies. The general approach consists first of determining the first ply failure, then discounting the damaged ply; after that the stresses are recalculated and checked against failure criterion to verify that the undamaged laminae do not fail immediately under their increased share of stress following the FPF above. In this analysis the strengths of the previously failed lamina (with reduced or totally discounted stiffness's) are assumed to be fictitiously very high to avoid repeated failure indication in the same plies. The load is then increased until the next ply or group of plies fail. This could be a failure in a previously undamaged ply or a new failure in a previously damaged one and all of the above calculations are repeated again. The process continues until the criterion for ultimate laminate failure (ULF) is met. Criteria's such as maximum load, last ply failure have been proposed. Theoretical predictions of ULF vary widely

depending on the definition of ULF and failure occurs when the laminate, at any stage of the progressive ply failures, cannot sustain the stresses. The flow diagrams for the FPF and ULF failure criteria's are shown in Figure 4.1 and Figure 4.2 respectively. The following section presents a sample calculation for a specific case study in order to clarify the calculation procedure.

4.3 Sample Calculation

4.3.1 Uniaxial Tensile Loading

This section presents a sample calculation to predict the failure stress and mode of each ply of a [90/45/-45/0]s Carbon/Epoxy (AS4/3501-6) laminate under uniaxial tensile stress by using the following failure theories, Maximum Stress, Maximum Strain, Tsai-Hill, and Tsai-Wu. The tensile strength of the laminate was calculated based on First Ply Failure (FPF) and Ultimate Laminate Failure (ULF). All calculations are based on the Classical Laminate Theories (CLT). The properties of (AS4/3501-6) are shown in Table 4.1.

Table 4.1: Material properties of carbon/epoxy (AS4/3501-6)

Longitudinal modulus E_1	21.3 (Msi)
Transverse modulus E_2	1.5 (Msi)
In-plane shear modulus G_{12}	1 (Msi)
Poisson's ratio ν_{12}	0.27 (Msi)
Longitudinal tensile strength F_{1t}	330 (Msi)
Transverse tensile strength F_{2t}	8.3 (Msi)
In plane shear strength F_6	11 (Msi)
Longitudinal compressive strength F_{1c}	250 (Msi)
Transverse compressive strength F_{2c}	33 (Msi)

We begin our calculation by finding the values of the reduced stiffness matrix for each of the eight plies first by neglecting hygrothermal and electrical effects, substituting into Eq. (2.26) we get

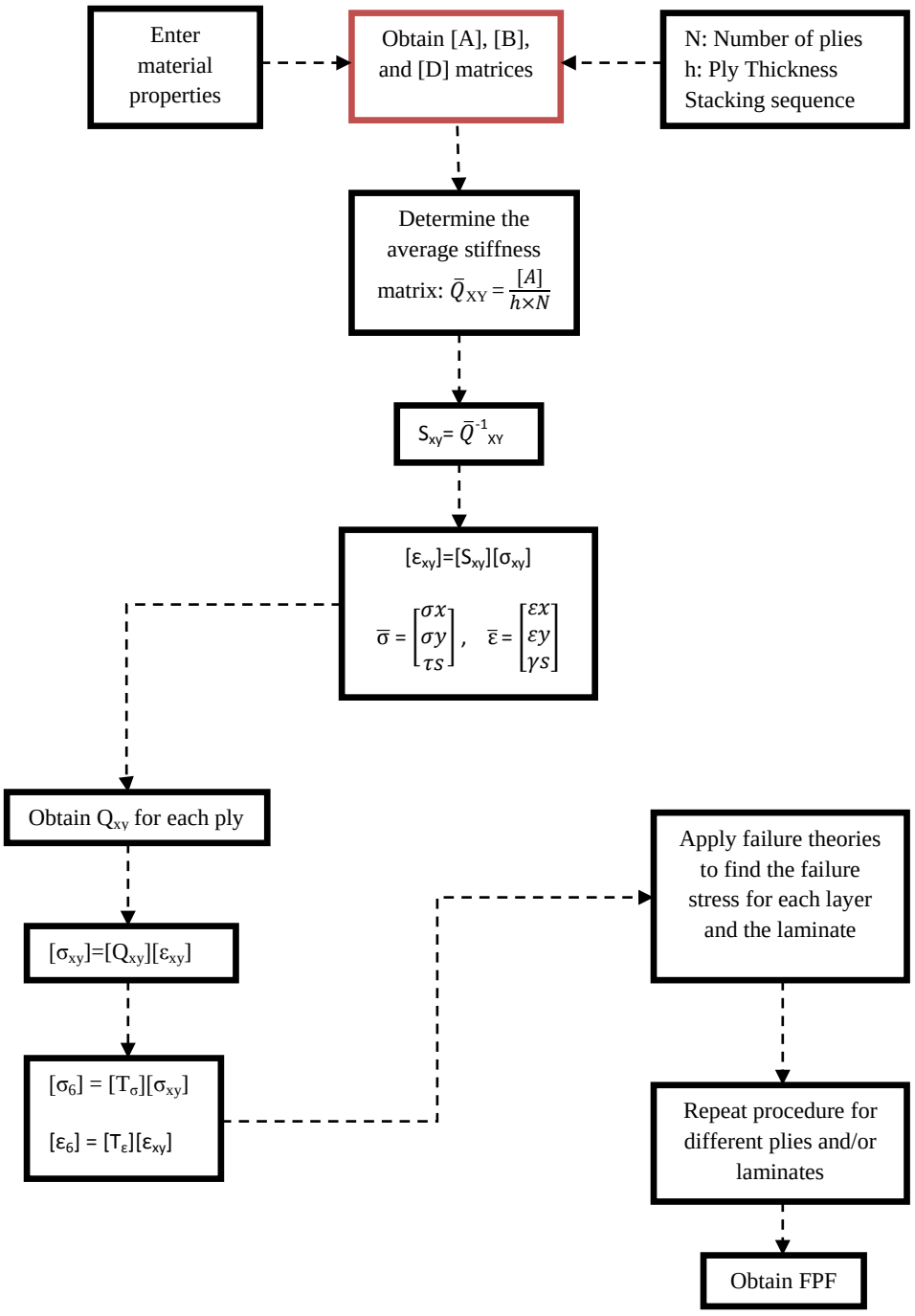

Figure 4.1: FPF flow chart

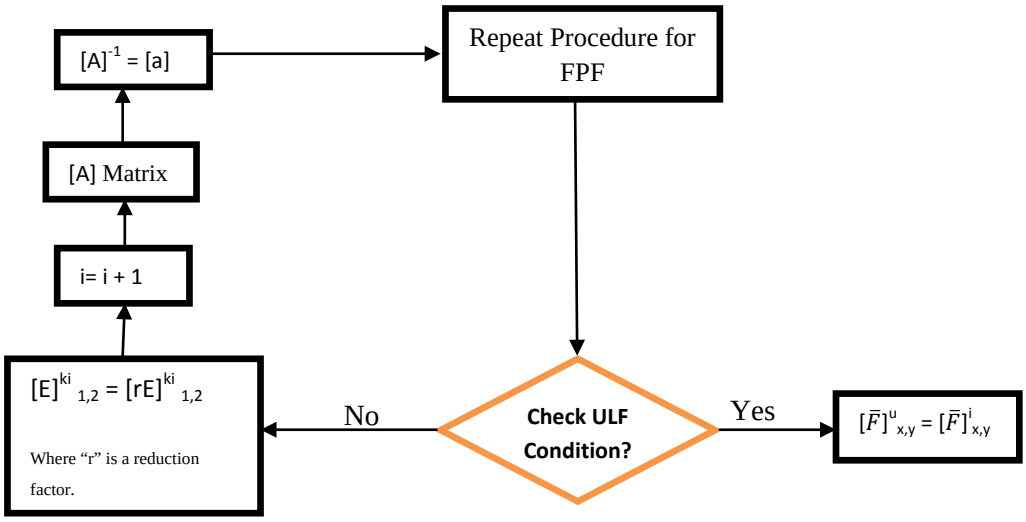

Figure 4.2: ULF flow chart

$$[Q]_{90^\circ} = \begin{bmatrix} 1.5081 & 0.4283 & 0 \\ 0.4283 & 21.4156 & 0 \\ 0 & 0 & 1.0000 \end{bmatrix} \; Msi$$

$$[Q]_{45^\circ} = \begin{bmatrix} 6.9530 & 4.9451 & 4.9805 \\ 4.9451 & 6.9372 & 4.9733 \\ 4.9805 & 4.9733 & 5.5168 \end{bmatrix} \; Msi$$

$$[Q]_{-45^\circ} = \begin{bmatrix} 6.9530 & 4.9451 & -4.9805 \\ 4.9451 & 6.9372 & -4.9733 \\ -4.9805 & -4.9733 & 5.5168 \end{bmatrix} \; Msi \qquad (4.7)$$

$$[Q]_{0^\circ} = \begin{bmatrix} 21.4156 & 0.4283 & 0 \\ 0.4283 & 1.5081 & 0 \\ 0 & 0 & 1.0000 \end{bmatrix} \; Msi$$

The other four plies are symmetric, so, they have the same values. The total thickness of the laminate is h = (0.005) × (8) = 0.04 inch. The midplane is 0.02 inch from the top and the bottom of the laminate and from Eq. (2.42), the extensional stiffness matrix **[*A*]** can be found as

$$[A] = \begin{bmatrix} 0.3683 & 0.1075 & 0 \\ 0.1075 & 0.3680 & 0 \\ 0 & 0 & 0.1303 \end{bmatrix} \; Msi \tag{4.8}$$

From Eq. (2.42), the coupling stiffness matrix **[*B*]** can be found as

$$[B] = \begin{bmatrix} 0 & 0 & 0 \\ 0 & 0 & 0 \\ 0 & 0 & 0 \end{bmatrix} \; Msi \tag{4.9}$$

From Eq. (2.42), the bending stiffness matrix **[*D*]** can be found as

$$[D] = \begin{bmatrix} 0 & 0 & 0 \\ 0 & 0 & 0 \\ 0 & 0 & 0 \end{bmatrix} \; Msi \tag{4.10}$$

We now find the average reduced stiffness matrix, which is defined as $[Q]_{xy(ave)} = \dfrac{[A]}{N \times h}$ where N is the number of plies and h is the ply thickness given as

$$[Q]_{xy(ave)} = \begin{bmatrix} 9.2075 & 2.6867 & 0 \\ 2.6867 & 9.1995 & 0 \\ 0 & 0 & 3.2584 \end{bmatrix} \; Msi \tag{4.11}$$

Since we have $Q_{xy(ave)}$ and the state of stress is known($\bar{\sigma}_1 = \bar{\sigma}_1$, $\bar{\sigma}_2 = 0$, $\bar{\tau}_6 = 0$), we can find the strain in the whole laminate, which is uniform through the thickness as discussed in Chapter II and given as

$$\begin{bmatrix} \bar{\sigma}_1 \\ \bar{\sigma}_2 \\ \bar{\tau}_6 \end{bmatrix} = \begin{bmatrix} \bar{Q}_{11} & \bar{Q}_{12} & \bar{Q}_{16} \\ \bar{Q}_{21} & \bar{Q}_{22} & \bar{Q}_{26} \\ \bar{Q}_{61} & \bar{Q}_{62} & \bar{Q}_{66} \end{bmatrix} \begin{bmatrix} \bar{\varepsilon}_1 \\ \bar{\varepsilon}_2 \\ \bar{\gamma}_6 \end{bmatrix} \tag{4.12}$$

$$\begin{bmatrix} \bar{\varepsilon}_1 \\ \bar{\varepsilon}_2 \\ \bar{\gamma}_6 \end{bmatrix} = \begin{bmatrix} 0.1187 \\ -0.0347 \\ 0 \end{bmatrix} \bar{\sigma}_1 \tag{4.13}$$

The average stress in each layer is now determined by obtaining the reduced stiffness matrix of each ply and multiplying it by the overall laminate strain to get

$$\begin{bmatrix} \bar{\sigma}_1 \\ \bar{\sigma}_2 \\ \bar{\tau}_6 \end{bmatrix}_{90^\circ} = \begin{bmatrix} 0.1642 \\ -0.6917 \\ 0 \end{bmatrix} \bar{\sigma}_1$$

$$\begin{bmatrix} \bar{\sigma}_1 \\ \bar{\sigma}_2 \\ \bar{\tau}_6 \end{bmatrix}_{45^\circ} = \begin{bmatrix} 0.6542 \\ 0.3467 \\ 0.4191 \end{bmatrix} \bar{\sigma}_1$$

$$\begin{bmatrix} \bar{\sigma}_1 \\ \bar{\sigma}_2 \\ \bar{\tau}_6 \end{bmatrix}_{-45^\circ} = \begin{bmatrix} 0.6539 \\ 0.3464 \\ -0.4187 \end{bmatrix} \bar{\sigma}_1 \tag{4.14}$$

$$\begin{bmatrix} \bar{\sigma}_1 \\ \bar{\sigma}_2 \\ \bar{\tau}_6 \end{bmatrix}_{0^\circ} = \begin{bmatrix} 2.5267 \\ -0.0014 \\ 0 \end{bmatrix} \bar{\sigma}_1$$

We will now find the transformation matrix of each ply in order to obtain the principle stress of each lamina.

$$
\begin{aligned}
[T]_{90^\circ} &= \begin{bmatrix} 0 & 1.0000 & 0 \\ 1.0000 & 0 & 0 \\ 0 & 0 & -1.0000 \end{bmatrix} \\
[T]_{45^\circ} &= \begin{bmatrix} 0.5004 & 0.4996 & 1.0000 \\ 0.4996 & 0.5004 & -1.0000 \\ -0.5000 & 0.5000 & 0 \end{bmatrix} \\
[T]_{-45^\circ} &= \begin{bmatrix} 0.5004 & 0.4996 & -1.0000 \\ 0.4996 & 0.5004 & 1.0000 \\ 0.5000 & -0.5000 & 0 \end{bmatrix} \\
[T]_{0^\circ} &= \begin{bmatrix} 1.0000 & 0 & 0 \\ 0 & 1.0000 & 0 \\ 0 & 0 & 1.0000 \end{bmatrix}
\end{aligned}
\tag{4.15}
$$

Substituting into Eq. (2.24) we get

$$
\begin{aligned}
\begin{bmatrix} \sigma_1 \\ \sigma_2 \\ \tau_6 \end{bmatrix}_{90^\circ} &= \begin{bmatrix} -0.6917 \\ -0.1642 \\ 0 \end{bmatrix} \bar{\sigma}_1 \\
\begin{bmatrix} \sigma_1 \\ \sigma_2 \\ \tau_6 \end{bmatrix}_{45^\circ} &= \begin{bmatrix} 0.9196 \\ 0.0813 \\ -0.1534 \end{bmatrix} \bar{\sigma}_1 \\
\begin{bmatrix} \sigma_1 \\ \sigma_2 \\ \tau_6 \end{bmatrix}_{-45^\circ} &= \begin{bmatrix} 0.9189 \\ 0.0813 \\ 0.1534 \end{bmatrix} \bar{\sigma}_1 \\
\begin{bmatrix} \sigma_1 \\ \sigma_2 \\ \tau_6 \end{bmatrix}_{0^\circ} &= \begin{bmatrix} 2.5277 \\ -0.0014 \\ 0 \end{bmatrix} \bar{\sigma}_1
\end{aligned}
\tag{4.16}
$$

By applying the failure theories previously discussed, we obtain the minimum failure stresses in each ply and then select the minimum stress of all the given plies in the

laminate which will correspond to our failure stress according to the first ply failure criteria. The results obtained using the maximum stress failure criteria are as follows

Ply 90°
Compressive failure stress = 0.3614 Msi
Tensile failure stress = 0.0505 Msi
Shear failure stress = 39.5936 Msi

Ply 0°
Tensile failure stress = 0.1306 Msi
Compressive failure stress = 22.898 Msi
Shear failure stress = 178.8404 Msi

Ply 45°
Tensile failure stress = 0.3588 Msi
Tensile failure stress = 0.1021 Msi
Shear failure stress = 0.0717 Msi

Ply -45°
Tensile failure stress = 0.3588 Msi
Tensile failure stress = 0.1021 Msi
Shear failure stress = 0.0717 Msi

The previous calculation can be repeated for all failure theories e.g. (Maximum Strain, Tsai-Hill and Tsai-Wu). The minimum load of each ply and its corresponding mode are shown in Table 4.2 - Table 4.5 for the different failure theories.

Table 4.2: Maximum stress theory ($\Delta T = 0$, $\Delta C = 0$)

	Minimum Stress ksi / Ply	Mode
90°	50	Transverse tensile stress
45°	75	Shear stress
-45°	75	Shear stress
0°	130	Longitudinal tensile stress

Table 4.3: Maximum strain theory (ΔT = 0, ΔC= 0)

	Minimum Stress ksi / Ply	Mode
90°	46	Transverse tensile stress
45°	75	Shear stress
-45°	75	Shear stress
0°	130	Longitudinal tensile stress

Table 4.4: Tsai-Hill theory (ΔT = 0, ΔC= 0)

	Minimum Stress ksi / Ply	Mode
90°	49.6	Transverse tensile stress
45°	59	Shear stress
-45°	59	Shear stress
0°	130	Longitudinal tensile stress

Table 4.5: Tsai-Wu theory (ΔT = 0, ΔC= 0)

	Minimum Stress ksi / Ply	Mode
90°	46.2	Transverse tensile stress
45°	90	Shear stress
-45°	90	Shear stress
0°	130	Longitudinal tensile stress

We can observe from the results that the FPF occurs in the 90° ply with a value of 51 ksi in the transverse tensile direction (based on maximum stress theory) and the failure stresses for the other failure theories vary slightly when comparing them with each other, yet, each one predicted the same mode and failure ply.

In order to apply the second criteria which is the Ultimate Laminate Failure (ULF), an iterative solution has to take place; so according to our data of the FPF we

eliminate the 90° ply and multiply its Longitudinal modulus, Transverse modulus, In-plane shear modulus and Poisson's ratio with a so called stiffness reduction factors which basically depend on the experiment environment (empirical approach) and can be obtained from analysis or experiments. In the case where matrix or interfiber failures are identified, the matrix dominated stiffness's are reduced as shown in Eq. (4.17). Typical values of for reduction factors are $r_1 = 1$ and $r_2 = r_{12} = 0.25$. These values were obtained for a carbon epoxy laminate having $[0/90_2]$s stacking sequence where it was observed that at the limiting crack density, the laminate modulus was reduced to approximately 90% of its original value and the reduced effective modulus of the 90° layer was reduced to approximately 25% of its original value [40]. Having obtained the reduction factors, the properties of the failed ply will then be updated according to Eq. (4.17)

$$\begin{aligned} E_1^{'} &= r_1 \times E_1 \\ E_2^{'} &= r_2 \times E_2 \\ G_{12}^{'} &= r_{12} \times G_{12} \\ \nu_{12}^{'} &= r_1 \times \nu_{12} \end{aligned} \tag{4.17}$$

Repeating all of the above calculations based on the new stiffness values for the 90° ply (failed ply) and continuing on with this process until the last ply failure is reached, in this particular case we will find that the failed ply is for each failure theory is shown in Table 4.6.

Table 4.6: ULF stress (ΔT = 0, ΔC= 0)

Failed Ply	Maximum Stress (ksi)	Maximum Strain (ksi)	Tsai-Hill (ksi)	Tsai-Wu (ksi)	Mode
0°	115.1	115	114.8	116	Longitudinal tensile stress

From here we obtain the failure load and mode according to the ULF criteria and as concluded for the FPF criteria, the failure stresses for the other failure theories varies slightly comparing them with each other, yet, each one predicted the same mode and failure ply. It could also be concluded from our analysis that the failure for the uniaxial loading case always occurs at the beginning in the fibers that are oriented in the transverse direction, which have the least resistance to overcome the load; then come the plies that are oriented towards the axis where the load is applied (0° plies) as shown in Figure 4.3.

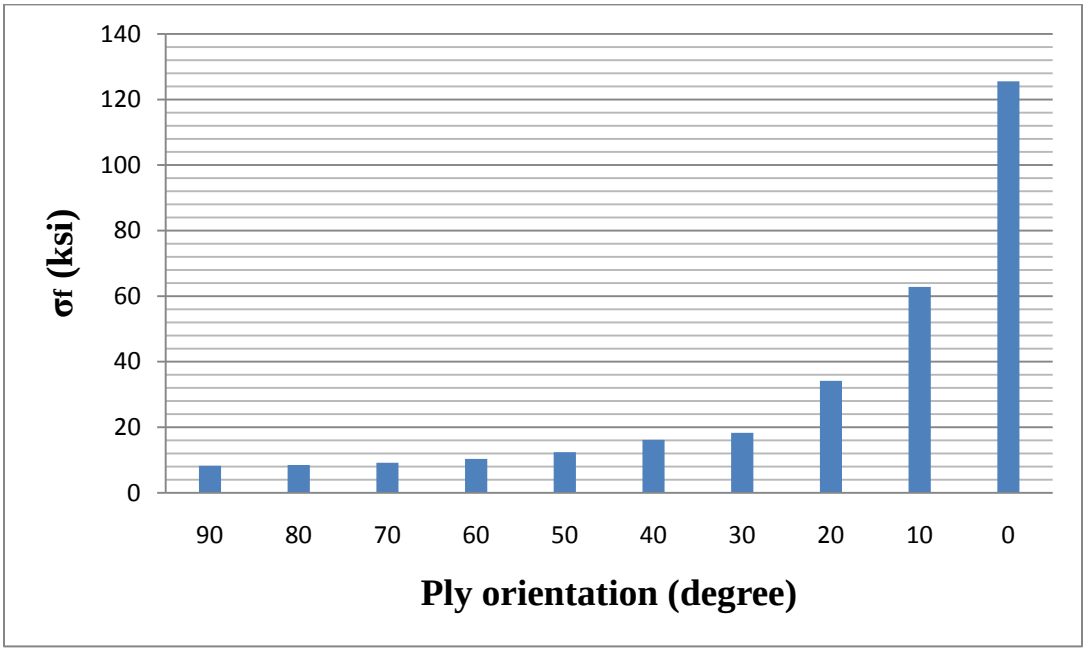

Figure 4.3: Variation of failure stress with fiber orientation

The next step describes the same analysis previously done but this time, a temperature difference is taken into account (ΔT = -100 °F) while keeping the moisture content equal to zero. The following results shown in Table 4.7 - Table 4.10 are obtained

Table 4.7: Maximum stress theory (ΔT = -100 °F, ΔC= 0)

Minimum Stress	ksi / Ply	Mode
90°	36.6	Transverse tensile stress
45°	70.7	Shear stress
-45°	70.7	Shear stress
0°	130.2	Longitudinal tensile stress

Table 4.8: Maximum strain theory (ΔT = -100 °F, ΔC= 0)

Minimum Stress	ksi / Ply	Mode
90°	33.7	Transverse tensile stress
45°	75	Shear stress
-45°	75	Shear stress
0°	130.1	Longitudinal tensile stress

Table 4.9: Tsai-Hill theory (ΔT = -100 °F, ΔC= 0)

Minimum Stress	ksi / Ply	Mode
90°	36.2	Transverse tensile stress
45°	48	Shear stress
-45°	48	Shear stress
0°	129	Longitudinal tensile stress

Table 4.10: Tsai-Wu theory (ΔT = -100 °F, ΔC= 0)

Minimum Stress	ksi / Ply	Mode
90°	33.7	Transverse tensile stress
45°	85	Shear stress
-45°	85	Shear stress
0°	127.6	Longitudinal tensile stress

Table 4.11: ULF stress (ΔT = -100 °F, ΔC= 0)

Failed Ply	Maximum Stress (ksi)	Maximum Strain (ksi)	Tsai-Hill (ksi)	Tsai-Wu (ksi)	Mode
0°	115.1	115	113.7	114	Longitudinal tensile stress

We can conclude from the results that by adding a temperature effect to the analysis, the failure load of the FPF was affected in a decreasing manner while the ULF failure value didn't have much significant difference. It also can be observed that the failed ply and corresponding mode are also the same compared to the results of the pure mechanical part. In addition, a moisture content difference is taken into account (ΔC = 0.5%) while keeping the temperature difference equal to zero. The following results shown in Table 4.12 - Table 4.16 are obtained.

Table 4.12: Maximum stress theory (ΔT = 0, ΔC= 0.5%)

Minimum Stress	ksi / Ply	Mode
90°	59.4	Transverse tensile stress
45°	75	Shear stress
-45°	75	Shear stress
0°	130.6	Longitudinal tensile stress

Table 4.13: Maximum strain theory (ΔT = 0, ΔC= 0.5%)

Minimum Stress	ksi / Ply	Mode
90°	54.7	Transverse tensile stress
45°	75	Shear stress
-45°	75	Shear stress
0°	130.5	Longitudinal tensile stress

Table 4.14: Tsai-Hill theory (ΔT = 0, ΔC= 0.5%)

Minimum Stress	ksi / Ply	Mode
90°	53	Transverse tensile stress
45°	51.4	Shear stress
-45°	51.4	Shear stress
0°	129.6	Longitudinal tensile stress

Table 4.15: Tsai-Wu theory (ΔT = 0, ΔC= 0.5%)

Minimum Stress	ksi / Ply	Mode
90°	54.4	Transverse tensile stress
45°	61.9	Shear stress
-45°	61.9	Shear stress
0°	132	Longitudinal tensile stress

Table 4.16: ULF stress (ΔT = 0, ΔC= 0.5%)

Failed Ply	Maximum Stress (ksi)	Maximum Strain (ksi)	Tsai-Hill (ksi)	Tsai-Wu (ksi)	Mode
0°	115.6	115.5	114.6	117	Longitudinal tensile stress

We can conclude from the results that by adding a moisture content effect to the analysis, the failure load of the FPF was only affected in an increasing manner while the

ULF failure value didn't have significant difference. It also can be observed that the failed ply and corresponding mode are also the same compared to the results of the pure mechanical part. Moreover, a moisture content in addition to a temperature difference simultaneously are taken into account (ΔC = 0.5% and ΔT = -100 °F). The following results shown in Table 4.17 - Table 4.21 are obtained

Table 4.17: Maximum stress theory (ΔT = -100 °F, ΔC= 0.5%)

Minimum Load	ksi / Ply	Mode
90°	45	Transverse tensile stress
45°	75	Shear stress
-45°	75	Shear stress
0°	130.8	Longitudinal tensile stress

Table 4.18: Maximum strain theory (ΔT = -100 °F, ΔC= 0.5%)

Minimum Load	ksi / Ply	Mode
90°	42.2	Transverse tensile stress
45°	75	Shear stress
-45°	75	Shear stress
0°	130.7	Longitudinal tensile stress

Table 4.19: Tsai-Hill theory (ΔT = -100 °F, ΔC= 0.5%)

Minimum Load	ksi / Ply	Mode
90°	45.3	Transverse tensile stress
45°	55.6	Shear stress
-45°	55.6	Shear stress
0°	128.9	Longitudinal tensile stress

Table 4.20: Tsai-Wu theory (ΔT = -100 °F, ΔC= 0.5%)

Minimum Load	ksi / Ply	Mode
90°	42	Transverse tensile stress
45°	88.7	Shear stress
-45°	88.7	Shear stress
0°	130.6	Longitudinal tensile stress

Table 4.21: ULF stress (ΔT = -100 °F, ΔC= 0.5%)

Failed Ply	Maximum Stress (ksi)	Maximum Strain (ksi)	Tsai-Hill (ksi)	Tsai-Wu (ksi)	Mode
0°	115.8	115.7	113.9	116.2	Longitudinal tensile stress

We can conclude from the previous results that by incorporating both moisture content and temperature effect to the analysis, the failure load of the FPF was only affected in a decreasing manner in this case which means that the temperature change had a more dominant effect on the overall behavior, also, the ULF value didn't have much significant difference as in the previous two cases. It also can be observed that the failed ply and corresponding mode are also the same compared to the results of the pure mechanical part.

The current study also focused on the failure of composite laminates including piezoelectric material layers in the composite layup. In order to observe the behavior of such composite laminates, several different case studies are adopted. Table 4.22 shows a summary of the different stacking sequences and materials considered.

Table 4.22: Summary of the different case studies considered

Stacking Sequence	Material of the (Actuator /Fiber Composite)
1- [Actuator/0/90/45/-45]s	AFC/Carbon Epoxy (AS4-3560)
2- [Actuator/0/90/45/-45]s	PZT-5A/Carbon Epoxy (AS4-3560)
3- [0/Actuator/90/45/-45]s	AFC/ Carbon Epoxy (AS4-3560)
4- [0/Actuator/90/45/-45]s	PZT-5A/ Carbon Epoxy (AS4-3560)

The analysis starts by neglecting both hygrothermal and electric effects and considering only the uniaxial mechanical load. The strength properties of the active materials used in the analysis are shown in Table 4.23; the assumed values are based on comparing the strength ratios with other fiber reinforced composite materials which have known material strengths. By following the same procedure done previously for the FPF and ULF considering only the maximum stress theory, results shown in Table 4.24 - Table 4.31 are obtained.

Table 4.23: Strength of different actuators

	F_{1t}/ksi	F_{2t}/ksi	F_{1c}/ksi	F_{2c}/ksi	F_6/ksi
AFC	3.48†	1.74	3.91†	1.95	2.37
MFC	4.35	2.17	3.91	1.95	2.61
PZT-5A	5.8‡	2.9	72.5*	36.2	3.19

†Ref [41], ‡ Ref [42], *Ref [43], the rest are assumed

Table 4.24: FPF stress (AFC/0/90/45/-45)s

Minimum Load	ksi / Ply	Mode
AFC	5.42	Longitudinal tensile stress
0°	119.7	Longitudinal tensile stress
90°	46.12	Transverse tensile stress
45°	67.5	Shear Stress
-45°	67.5	Shear Stress

Table 4.25: ULF stress (AFC/0/90/45/-45)s

Failed Ply	Maximum Stress (ksi)	Mode
0°	108.31	Longitudinal tensile stress

Table 4.26: FPF stress (PZT/0/90/45/-45)s

Minimum Load	ksi / Ply	Mode
PZT5A	6.1	Longitudinal tensile stress
0°	128.2	Longitudinal tensile stress
90°	49.6	Transverse tensile stress
45°	71.5	Shear Stress
-45°	71.5	Shear Stress

Table 4.27: ULF stress (PZT/0/90/45/-45)s

Failed Ply	Maximum Stress (ksi)	Mode
0°	120.1	Longitudinal tensile stress

Table 4.28: FPF stress (0/AFC/90/45/-45)s

Minimum Load	ksi / Ply	Mode
AFC	12.6	Longitudinal tensile stress
0°	120.5	Longitudinal tensile stress
90°	46.6	Transverse tensile stress
45°	65.2	Shear Stress
-45°	65.2	Shear Stress

Table 4.29: ULF stress (0/AFC/90/45/-45)s

Failed Ply	Maximum Stress (ksi)	Mode
0°	108	Longitudinal tensile stress

Table 4.30: FPF stress (0/PZT/90/45/-45)s

Minimum Load	ksi / Ply	Mode
PZT5A	2.33	Longitudinal tensile stress
0°	133.4	Longitudinal tensile stress
90°	51.3	Transverse tensile stress
45°	73.2	Shear Stress
-45°	73.2	Shear Stress

Table 4.31: ULF stress (0/PZT/90/45/-45)s

Failed Ply	Maximum Stress (ksi)	Mode
0°	119	Longitudinal tensile stress

It can be observed form the previous results that the FPF always occurs in active layer due to its low strength properties compared to the remaining carbon epoxy layers while the ULF takes place in the 0° ply as expected due to its high resistance to the load. It can also be observed that the failure loads vary with stacking sequence since, in the case where the active layer is incorporated into the laminate as in the third and forth sequence, the AFC layer had higher FPF stress unlike the PZT layer where the value of the FPF stress decreased.

The effect of applying a 1MV/m electric field to the active part of an [Actuator/90/60/-60]s composite layup is shown in Table 4.32. In addition, the effect of including a $\Delta T = 100°F$ temperature difference to the composite is observed in Table 4.33.

Table 4.32: FPF stress including ξ = 1MV/m

Actuator	FPF (E = 0)	FPF (E = 1MV/m)
AFC/31mode	1.92 ksi	1.82 ksi
AFC/33mode	1.92 ksi	2.12 ksi
PZT	2.36 ksi	2.13 ksi

Table 4.33: FPF stress including ξ = 1MV/m and $\Delta T = 100°F$

Actuator	FPF (E = 0 ΔT = 0)	FPF (E = 1MV/m, ΔT = 100°F)
AFC/31mode	1.92 ksi	0.477 ksi
AFC/33mode	1.92 ksi	0.76 ksi
PZT	2.36 ksi	1.1 ksi

According to these results, it could be observed that the applied electric field reduced the failure stress when considering the AFC (31 mode) while it increased the failure stress it in the case of using the 33 mode. This is due to the positive piezoelectric strain coefficient in that direction unlike the 31 mode where it has a negative value. It could also be observed that the 33 mode had a more significant effect than the 31 mode due to the higher piezoelectric coefficient in the 33 mode case. The temperature variation also decreased the value of the failure load but with a more significant effect compared to the electric field variation.

4.3.2 Biaxial Loading

Composite laminates under biaxial loading is also taken into consideration in this study, the same methodology used in the uniaxial loading is considered but in this case, the geometry and loading condition are as shown in Figure 4.4.

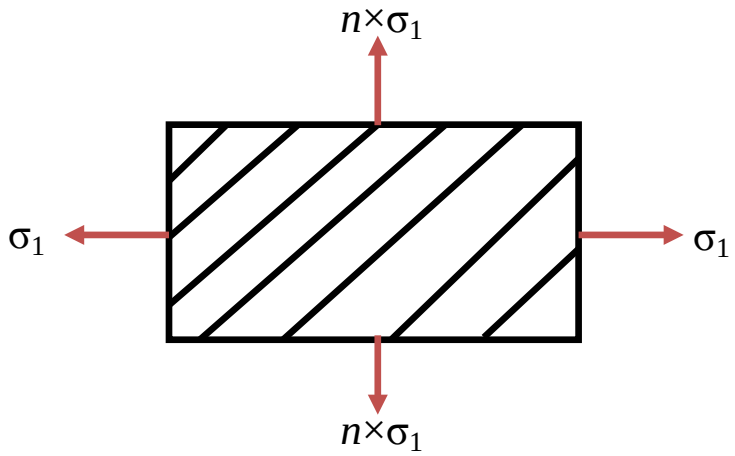

Figure 4.4 Laminate under biaxial load

The factor *n* shown in the figure is the ratio of the stress applied in the transverse direction to that in the axial direction. A summary of each case is shown in Eq. (4.18); as can be seen from the equation, when the value of *n* = 0, a pure uniaxial load arises which is obviously a special case of the biaxial loading.

$$n = \frac{\sigma_2}{\sigma_1} = \begin{Bmatrix} 0 \rightarrow \textit{Uniaxial Load} \\ 1 \rightarrow \textit{Biaxial Load} \\ 0 \prec n \prec 1 \rightarrow \textit{Biaxial Load} \\ n \succ 1 \rightarrow \textit{Biaxial Load} \end{Bmatrix} \tag{4.18}$$

In order generalize the analysis as much as possible; we take into account all possible load combinations whether the load is in tension or compression as shown in Figure 4.5. The state of stress can now be defined as ($\sigma_1 = \sigma_1, \sigma_2 = n \times \sigma_1, \tau_1 = 0$).

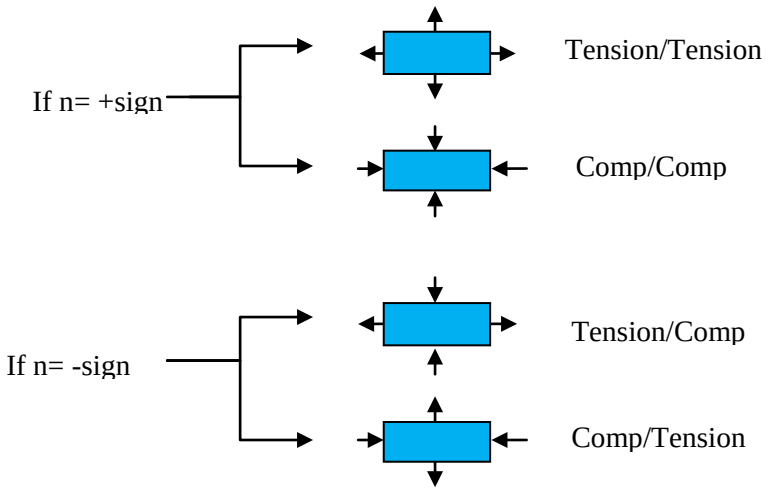

Figure 4.5 Biaxial load combinations

In order to observe the effect of applying a biaxial load on the composite laminate, a detailed calculation for the same composite layup and material used in the uniaxial case is performed in order to get the failure stress by considering the same two types of failure criteria's FPF and ULF mentioned previously, in addition to using the four failure theories that were previously mentioned. The results are summarized in the following tables.

Table 4.34: FPF stress for several different failure theories; n=0 (Tension)

Failure Stress Based on FPF criteria (ksi) for [90/45/-45/0]s Sequence					**Mode**
Ply Orientation	Maximum Stress	Maximum Strain	Tsai-Hill	Tsai-Wu	
90°	50	46	49.6	46.6	Transverse Tensile Stress
45°	75	75	59	55	Shear Stress
-45°	75	75	59	55	Shear Stress
0°	130	130	130	130.8	Longitudinal Tensile Stress

Table 4.35: ULF stress for several different failure theories; n=0 (Tension)

Failed Ply	**Maximum Stress (ksi)**	**Maximum Strain (ksi)**	**Tsai-Hill (ksi)**	**Tsai-Wu (ksi)**	**Mode**
0°	115.1	115	113.7	114	Longitudinal tensile stress

Table 4.34 and Table 4.36 show the results of applying a pure uniaxial load in tension and compression on the composite laminate respectively. As shown in the tables, the FPF occurred in the 90° ply for the tension case as expected while in the

compression case, it occurred in the 45°/-45° plies. The ULF in both cases were dominated by the cross plies where it occurred in the 0 ply in the tension case and 90 ply in the compression case as shown in Table 4.35and Table 4.37 respectively.

Table 4.36: FPF stress for several different failure theories; n=0 (Compression)

Failure Stress Based on FPF criteria (ksi) for [90/45/-45/0]s Sequence					**Mode**
Ply Orientation	Maximum Stress	Maximum Strain	Tsai-Hill	Tsai-Wu	
90°	201	201	182	167.4	Transverse Compressive Stress
45°	71.7	71.7	68.5	85.3	Shear Stress
-45°	71.7	71.7	68.5	85.3	Shear Stress
0°	98.9	98.9	98.9	97.8	Longitudinal Compressive Stress

Table 4.37: ULF stress for several different failure theories; n=0 (Compression)

Failed Ply	**Maximum Stress (ksi)**	**Maximum Strain (ksi)**	**Tsai-Hill (ksi)**	**Tsai-Wu (ksi)**	**Mode**
90°	161	161	158	155	Transverse Compressive Stress

\

Table 4.38: FPF stress for several different failure theories; n=1 (Ten/Ten)

Failure Stress Based on FPF criteria (ksi) for [90/45/-45/0]s Sequence					Mode
Ply Orientation	Maximum Stress	Maximum Strain	Tsai-Hill	Tsai-Wu	
90°	51	51	49.2	58	Transverse Tensile Stress
45°	50.9	50.9	49.2	58	Transverse Tensile Stress
-45°	51	51	49.2	58	Transverse Tensile Stress
0°	50.9	50.9	49.2	58	Transverse Tensile Stress

Table 4.39: ULF stress for different failure theories; n=1 (Ten/Ten)

Failed Ply	Maximum Stress (ksi)	Maximum Strain (ksi)	Tsai-Hill (ksi)	Tsai-Wu (ksi)	Mode
0°	50.9	51	49.2	58	Transverse Tensile Stress

Table 4.38 and Table 4.40 show the results of applying a biaxial load in tension - tension case and compression – compression case on the composite laminate respectively. As shown in the tables; the stress is almost equally distributed throughout all the plies of the laminate which will lead all the plies to fail at once. The ULF in both cases is equal to the FPF since there is no variation between the plies as shown in Table 4.39 and Table 4.41 respectively.

Table 4.40: FPF stress for several different failure theories; n=1 (Comp/Comp)

Failure Stress Based on FPF criteria (ksi) for [90/45/-45/0]s Sequence					Mode
Ply Orientation	Maximum Stress	Maximum Strain	Tsai-Hill	Tsai-Wu	
90°	136	136	116	58	Transverse Compressive Stress
45°	136	136	116	58	Transverse Compressive Stress
-45°	136	136	116	58	Transverse Compressive Stress
0°	136	136	116	58	Transverse Compressive Stress

Table 4.41: ULF stress for several different failure theories; n=1 (Comp/Comp)

Failed Ply	Maximum Stress (ksi)	Maximum Strain (ksi)	Tsai-Hill (ksi)	Tsai-Wu (ksi)	Mode
90°	136	136	116	58	Transverse Compressive Stress

Table 4.42: FPF stress for several different failure theories; n = -1 (Ten/Comp)

Failure Stress Based on FPF criteria (ksi) for [90/45/-45/0]s Sequence					Mode
Ply Orientation	Maximum Stress	Maximum Strain	Tsai-Hill	Tsai-Wu	
90°	50.1	50.1	41.8	37.9	Transverse Tensile Stress
45°	35.8	35.8	35.8	35.9	Shear Stress
-45°	35.8	35.8	35.8	35.9	Shear Stress
0°	102.5	102.5	89.3	87.3	Longitudinal Tensile Stress

Table 4.43: ULF stress for several different failure theories; n = -1 (Ten/Comp)

Failed Ply	Maximum Stress (ksi)	Maximum Strain (ksi)	Tsai-Hill (ksi)	Tsai-Wu (ksi)	Mode
0°	81	81	78	75	Longitudinal Tensile Stress

Table 4.44: FPF stress for several different failure theories; n = -1 (Comp/Ten)

Failure Load Based on FPF criteria (ksi) for [90/45/-45/0]s Sequence					Mode
Ply Orientation	Maximum Stress	Maximum Strain	Tsai-Hill	Tsai-Wu	
90°	102.4	102.4	89.3	87.3	Longitudinal Tensile Stress
45°	35.8	35.8	35.8	35.8	Shear Stress
-45°	35.8	35.8	35.8	35.8	Shear Stress
0°	50.1	50.1	41.8	37.9	Transverse Tensile Stress

Table 4.45: ULF stress for several different failure theories; n = -1 (Comp/Ten)

Failed Ply	Maximum Stress (ksi)	Maximum Strain (ksi)	Tsai-Hill (ksi)	Tsai-Wu (ksi)	Mode
90°	81	81	78	75	Longitudinal Tensile Stress

Table 4.42 and Table 4.44 show the results of applying a pure biaxial loading, but this time, the load fraction *n* has a negative value giving the possibility of applying either tension - compression or compression - tension to the composite laminate respectively. As shown in the tables, the minimum stress occurred in the 45°/-45° ply for the tension- compression case due to their low resistance regarding the given loading condition while the compression - tension case gives a reverse behavior keeping the

45°/-45 plies the least resistive hence the first to fail. The ULF in both cases were dominated by the cross plies where it occurred in the 0° ply in the tension- compression case and 90° ply in the compression -tension case as shown in Table 4.43and Table 4.45 respectively.

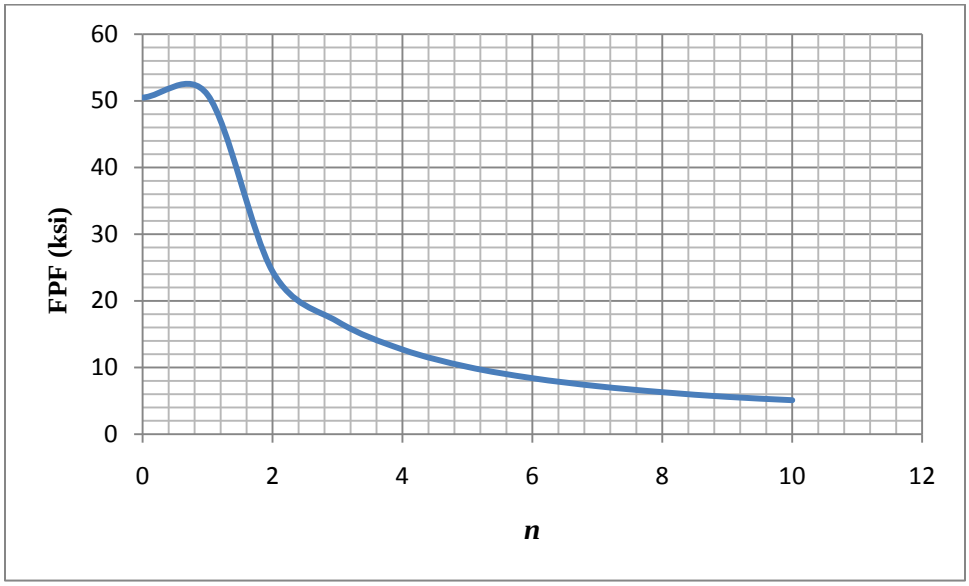

Figure 4.6: Variation of failure stress with load fraction for [90/45/-45/0]s sequence (Ten/Ten) case

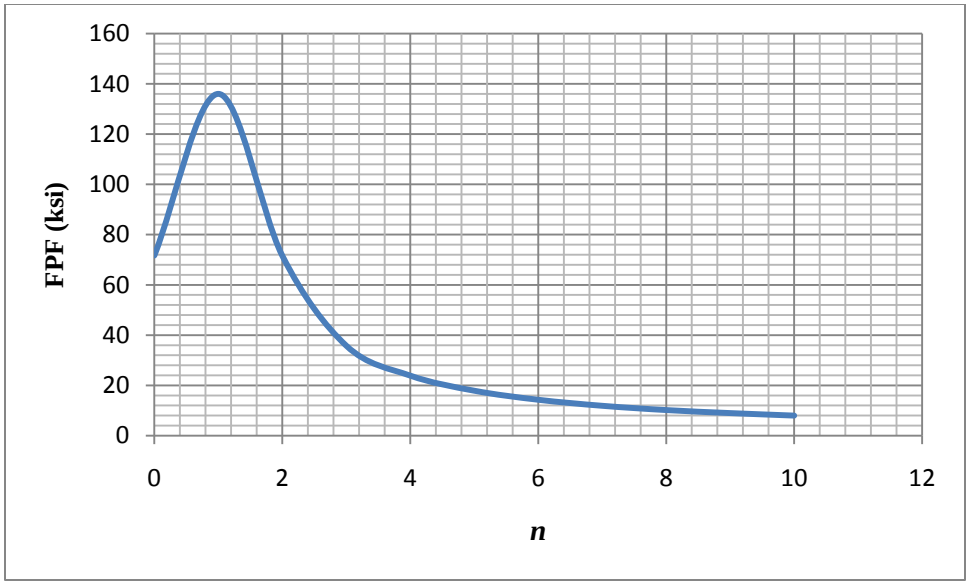

Figure 4.7: Variation of failure stress with load fraction for [90/45/-45/0]s sequence (Comp/Comp) case

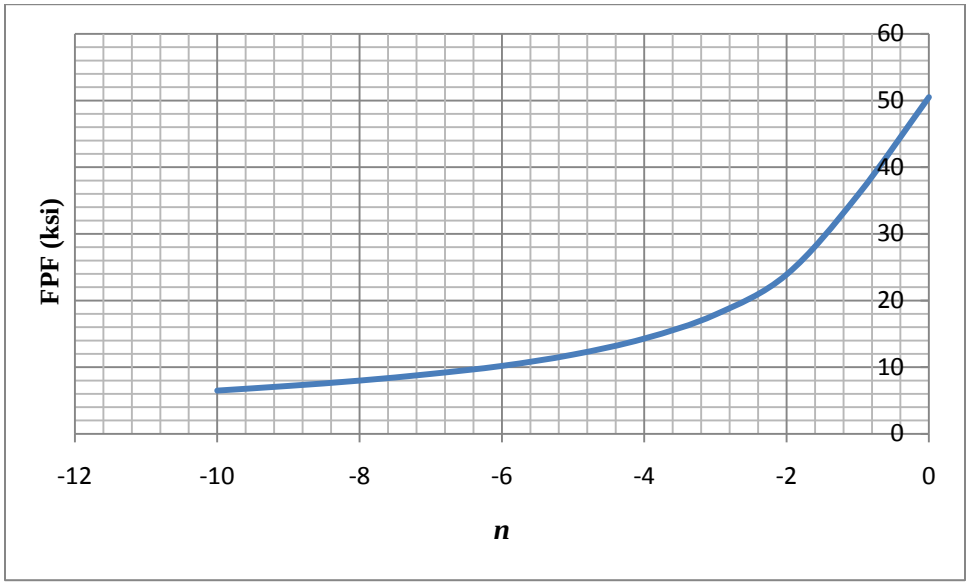

Figure 4.8: Variation of failure stress with load fraction for [90/45/-45/0]s sequence (Ten/Comp) case

The variation of the FPF with respect to the load fraction *n* is considered for the composite layup. Figure 4.6 shows the variation for the tension –tension case, it can be

observed that the failure stress first increases followed by a decreasing scheme, this behavior is due to the failure occurrence in the 90° ply for n = 0 and continues in the 0° ply afterwards. Figure 4.7 shows the variation for the compression – compression case, it can also be observed that the failure stress first increases followed by a decreasing scheme, this behavior is due to the failure occurrence in the 45° ply continuously throughout the application of the load. In the last case as shown in Figure 4.8, considering compression /tension or tension /compression, there is no difference in the behavior hence; taking the tension /compression case, we have a deceasing trend occurring first in the 90° then continuing in the 45° ply.

Similar to the uniaxial case, the failure of composite laminates including piezoelectric material layers in the composite layup is also taken into account. The same case studies shown in Table 4.22 are considered with the same stacking sequences and materials. The analysis starts by neglecting both hygrothermal and electric effects and considering only the biaxial loading with different load fractions. By following the same procedure done previously for the FPF and ULF, results shown in Table 4.46 - Table 4.49 are obtained for the case of using n = 1 (Ten/Ten) load.

Table 4.46: FPF stress; n=1, Ten/Ten - (AFC/0/90/45/-45)s

Minimum Load	ksi / Ply	Mode
AFC	6.48	Longitudinal tensile stress
0°	38.9	Transverse tensile stress
90°	41.5	Transverse tensile stress
45°	40.1	Transverse tensile stress
-45°	40.1	Transverse tensile stress

Table 4.47: FPF stress; n=1, Ten/Ten – (PZT/0/90/45/-45)s

Minimum Load	ksi / Ply	Mode
PZT5A	2.5	Longitudinal tensile stress
0°	71.3	Transverse tensile stress
90°	71.3	Transverse tensile stress
45°	71.3	Transverse tensile stress
-45°	71.3	Transverse tensile stress

Table 4.48: FPF stress; n=1, Ten/Ten – (0/AFC/90/45/-45)s

Minimum Load	ksi / Ply	Mode
AFC	1.79	Longitudinal tensile stress
0°	42.5	Transverse tensile stress
90°	45.6	Transverse tensile stress
45°	44	Transverse tensile stress
-45°	44	Transverse tensile stress

Table 4.49: FPF stress; n=1, Ten/Ten – (0/PZT/90/45/-45)s

Minimum Load	ksi / Ply	Mode
PZT5A	3.14	Longitudinal tensile stress
0°	50.77	Transverse tensile stress
90°	50.77	Transverse tensile stress
45°	50.77	Transverse tensile stress
-45°	50.77	Transverse tensile stress

In this case, the failure also occurs in the active layer due to its low strength properties in the longitudinal and transverse direction compared to the other carbon epoxy layers, in addition, the stacking sequence also had significant effect related to the stress distribution between the different plies. In all cases it can be observed that the

failure takes place in the active layer with the same mode of failure. Table 4.50 - Table 4.53 are the results obtained for the case of using n = -1 with a (Ten/Comp) load.

Table 4.50: FPF stress; n= -1, Ten/Comp – (AFC/0/90/45/-45)s

Minimum Load	ksi / Ply	Mode
AFC	4.46	Longitudinal tensile stress
0°	174.7	Transverse tensile stress
90°	50.8	Transverse tensile stress
45°	49	Shear stress
-45°	49	Shear stress

Table 4.51: FPF stress; n= -1, Ten/Comp – (PZT/0/90/45/-45)s

Minimum Load	ksi / Ply	Mode
PZT5A	5.9	Longitudinal tensile stress
0°	33.63	Transverse tensile stress
90°	8.41	Transverse tensile stress
45°	10.9	Shear stress
-45°	10.9	Shear stress

Table 4.52: FPF stress; n= -1, Ten/Comp – (0/AFC/90/45/-45)s

Minimum Load	ksi / Ply	Mode
AFC	0.98	Longitudinal tensile stress
0°	94.6	Longitudinal tensile stress
90°	47.68	Transverse tensile stress
45°	31.4	Shear stress
-45°	31.4	Shear stress

Table 4.53: FPF stress; n= -1, Ten/Comp – (0/PZT/90/45/-45)s

Minimum Load	ksi / Ply	Mode
PZT5A	1.85	Longitudinal tensile stress
0°	106.1	Longitudinal tensile stress
90°	51.9	Transverse tensile stress
45°	36.5	Shear stress
-45°	36.5	Shear stress

The results shown indicate that the failure occurs in the active layer as expected due to its low strength properties in the longitudinal and transverse direction compared to the other carbon epoxy layers as in the previous case, while this time, the modes of failure are different. Moreover, the stacking sequence also had significant effect in the stress distribution between the different plies. In all cases it can be observed that the failure takes place in the active layer with the same mode of failure. The effect of applying a 1MV/m electric field to the active part of an [Actuator/90/60/-60]s composite layup is shown in Table 4.54. In addition, the effect of including a $\Delta T = 100°F$ temperature difference to the composite is observed in Table 4.55.

Table 4.54: FPF stress including E = 1MV/m

Actuator	FPF (E = 0)	FPF (E = 1MV/m)
AFC/31mode	1.92 ksi	1.82 ksi
AFC/33mode	1.92 ksi	2.12 ksi
PZT	2.36 ksi	2.33 ksi

Table 4.55: FPF including E = 1MV/m and ΔT = 100°F

Actuator	FPF (E = 0 ΔT = 0)	FPF (E = 1MV/m ΔT = 100°F)
AFC/31mode	1.92 ksi	0.56 ksi
AFC/33mode	1.92 ksi	0.76 ksi
PZT	2.36 ksi	0.91 ksi

Similar to the results found for the uniaxial case, it could be observed that the electric field minimized the failure load for both active layers while maximized it in the case of using the 33 mode for the AFC due to the positive piezoelectric strain coefficient in that direction unlike the 31 mode where it has a negative value. The temperature variation also decreased the value of the failure load in all cases but with a more significant effect compared to the electric field variation.

It can be observed from the previous analysis that at each stage of failure there is a corresponding strength at which we define the initial stage as the FPF and the last stage as the ULF. The ratio of these two strengths is a measure of the laminate efficiency and indicates the level of fiber strength utilization at FPF which is defined as

$$\phi = \frac{FPF}{ULF} \tag{4.19}$$

The ratio obviously depends on both the material used and the laminate layup. Table 4.56 and Table 4.57 show a comparison of the FPF and ULF of different multidirectional laminates under uniaxial tensile loading and there corresponding laminate efficiency. It can be observed that the laminate efficiency ratio for the $[0/90]_s$ crossply laminates are low for all materials ranging from 0.25 for E-Glass Epoxy to 0.37

for Carbon/Epoxy. In the case of $[0/45/-45]_s$ laminates the laminate efficiency ratio are higher and range from 0.39 to 0.89. It could be concluded that the laminates that consist of cross ply laminas have a higher range for factors of safety unlike the laminates that include other oriented laminas in their sequence, this could be associated with the nature of the failure criteria used, since, the FPF is more conservative than the ULF and higher factors of safety have to be taken into account when considering it in the design process. It could also be thought of both failure criteria's as lower and upper bound for the failure stress for any general composite layups.

Table 4.56: Comparison of FPF and ULF for different materials of [0/90]s laminate

Material	**FPF (ksi)**	**ULF (ksi)**	**Laminate Efficiency Ratio Φ = FPF/ULF**
E-Glass/Epoxy	14.5	57.4	0.25
Carbon/Epoxy (AS4/3501-6)	50	134.6	0.37
S-Glass/Epoxy	18.3	69.7	0.26
Kevlar/Epoxy	32.9	99	0.33

Table 4.57: Comparison of FPF and ULF for different materials of [0/45/-45]s laminate

Material	FPF (ksi)	ULF (ksi)	Laminate Efficiency Ratio Φ = FPF/ULF
E-Glass/Epoxy	37.2	69.7	0.53
Carbon/Epoxy (AS4/3501-6)	64.6	123.6	0.52
S-Glass/Epoxy	37.8	94.8	0.39
Kevlar/Epoxy	66	74	0.89

In order to gain confidence in the results obtained we compare the ULF results predicted using the previous analysis with available experimental results in the literature. Table 4.58 shows a comparison between measured and predicted ULF values for a number of laminates using Carbon/Epoxy (AS4/3501-6). It can be concluded that the predictions of the failure theories used in the analysis are almost in agreement with the experimental values but with some variations regarding the failure theory used. In the case where the laminates include 0° plies, the failure is fiber dominated because the 0° plies carry a substantial portion of the total load where in the case of angle ply laminates the failure is matrix dominated. It can also be observed that in the case of using angle ply laminates, predictions by the limit or non interactive theories are not usually in agreement with each other and with experimental results.

Table 4.58: Comparison of ULF with available experimental data

Laminate	Experimental (ksi)	Maximum Stress (ksi)	Maximum Strain (ksi)	Tsai-Hill (ksi)	Tsai-Wu (ksi)
$[0/90_2]_s$*	113	113	114	93	124
$[0_2/90_2]_s$*	161	167	168	138	181
$[0/-+45]_s$*	127	123	122	112	111
$[+-20]_{2s}$*	117	116	116	105	125
$[+-45]_s$*	22	22	22	21	23
$[-60/60/0_2]_s$**	106	115	115	114	116

*** Ref. [40], ** Ref. [44]**

4.3.3 Finite Element Verification

In order to further verify the results obtained from the analysis, a finite element model is implemented through the commercial finite elements software ABAQUS to perform a certain case study. A composite laminate made of Carbon/Epoxy (AS4/3501-6) which has properties defined previously in Table 4.1; the model consists of 8 plies with fiber orientation [90/45/-45/0]s. The composite plate is modeled using 20-node quadratic continuum elements with reduced integration (C3D20R), the total number of elements are 12000. The finite element mesh is shown in Figure 4.9. In order to simulate the failure, we apply the predicted failure load to the composite plate as was found from the previous study for both a pure uniaxial load in addition to a biaxial load (Tension/Compression with n = -1). In the uniaxial case, it is observed that the transverse stress (σ_2 = 130 ksi) in the 90° ply exceeds the transverse tensile strength of the material which means that it failed according to macromechanical failure theories,

while all the other plane stresses in the rest of the plies have not exceeded the corresponding strength as it can be shown in Table 4.59 Similarly, for the biaxial case shown in Table 4.60, the shear stress (τ_6 = 11.3 ksi) exceeded the corresponding strength as was predicted in the previous analysis.

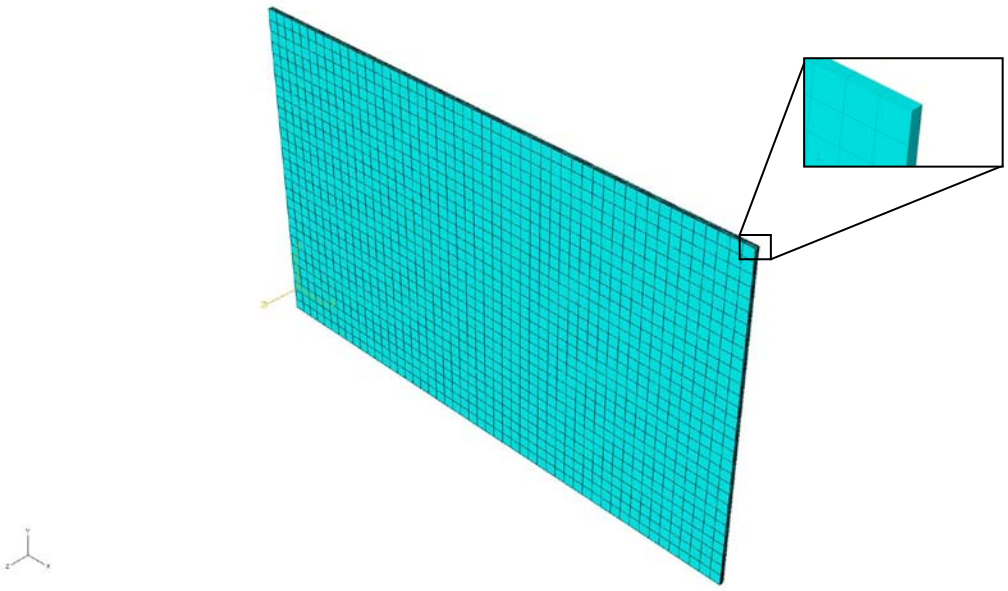

Figure 4.9: Finite element mesh

Table 4.59: Predicted finite element stresses in each ply (uniaxial case)

Ply	σ_1 (ksi)	σ_2 (ksi)	τ_6 (ksi)	F_{1t} (ksi)	F_{2t} (ksi)	F_6 (ksi)
0˚	133	0.67	0.014	330	8.3	250
90˚	36	8.7	0.0054	330	8.3	250
45˚	47.3	4.13	8.1	330	8.3	250
-45˚	47.2	4.16	8.2	330	8.3	250

Table 4.60: Predicted finite element stresses in each ply (biaxial case *n* = -1) Ten/Comp

Ply	σ_1 (ksi)	σ_2 (ksi)	τ_6 (ksi)	F_{1t} (ksi)	F_{2t} (ksi)	F_6 (ksi)
0˚	118.8	7.07	0.001	330	8.3	250
90˚	118.6	6.22	.008	330	8.3	250
45˚	0.038	0.011	254	330	8.3	250
-45˚	0.021	0.006	254	330	8.3	250

In addition, a composite laminate consisting of 10 plies with the following sequence [AFC/Carbon-Epoxy$_4$]s and fiber orientation [0 /0 /90 /45/ -45]s both for uniaxial and biaxial loading is also considered; by applying the failure load that was obtained from the previous uniaxial and biaxial analysis to the composite laminate respectively; it can be observed that the AFC ply is the one that exceeded the

corresponding ply strength for the same predicted failure mode, hence, the one to fail as shown in Table 4.61 and Table 4.62. According to the result obtained from the FE model, we can conclude that the results obtained from the failure analysis are reliable.

Table 4.61: Predicted finite element stresses in each ply (uniaxial hybrid composite)

Ply	σ_1 (ksi)	σ_2 (ksi)	τ_6 (ksi)	F_{1t} (ksi)	F_{2t} (ksi)	F_6 (ksi)
AFC	4.14	0.36	0.0024	3.48	1.74	2.43
0˚	16.3	0.188	0.005	330	8.3	250
90˚	2.2	0.94	0.00003	330	8.3	250
45˚	9.89	0.62	0.855	330	8.3	250
-45˚	9.89	0.62	0.855	330	8.3	250

Table 4.62: Predicted finite element stresses in each ply (biaxial hybrid composite *n* = -1) Ten/Comp

Ply	σ_1 (ksi)	σ_2 (ksi)	τ_6 (ksi)	F_{1t} (ksi)	F_{2t} (ksi)	F_6 (ksi)
AFC	3.66	0.98	0.0003	3.48	1.74	2.43
0˚	117.7	6.3	0.0005	330	8.3	250
90˚	119.8	6.2	0.0001	330	8.3	250
45˚	4.3	.59	1.62	330	8.3	250
-45˚	4.4	.56	1.62	330	8.3	250

The effect applying of an out of plane loading followed by a temperature difference on the failure of smart composite laminates is also considered in this study. The plate considered is cantilevered at one end and subjected to out of plane loading at the free end in the first part and a temperature difference in the second part. The finite element model is used on a [0/45/-45/90]s laminate with two MFC actuators embedded into the composite structure. The material used and their properties are shown in Table 4.63. The geometry of the composite plate with the MFC actuators is shown in Figure 4.10. The structure is subjected to an increase in the external loading by applying a 100N followed by a 1kN external load to the free end of the plate respectively. Moreover, a temperature difference of 100°C is applied to the composite plate in order to measure the stresses accumulated from this temperature difference. Table 4.64 shows the calculated in-plane plate stresses in the composite laminate layers and the actuator; by comparing them with the corresponding strength properties of each material, it can be observed that the failure occurs in the MFC actuators before the composite layers at a lower load due to the low strength properties of the MFC actuators. The 90° layer is shown to have the highest capability to sustain the load since it shows the lowest stress compared to all other plies. In addition, by applying a 1kN load to the smart composite plate, several layers in the composite exceeded the corresponding strength hence failed as shown in Table 4.65. The only ply that sustained the applied load was the 90° ply which as indicated before has the highest resistance to overcome the out of plane load.

Table 4.63: Composite material and actuator properties

Material Property	Carbon Epoxy (AS4-3601)	MFC
E_1 (GPa)	147	30.3
E_2 (GPa)	10.3	15.9
E_3 (GPa)	10.3	11.47
ν_{12}	0.27	0.31
ν_{13}	0.27	0.289
ν_{23}	0.54	0.327
G_{12}(GPa)	7	5.5
G_{13}(GPa)	7	2.6
G23(GPa)	3.7	2.14
α_1 (μ/°C)	-0.09	5.9
α_2(μ/°C)	27	29.6
α_3(μ/°C)	27	19
t (mm)	0.3	0.3

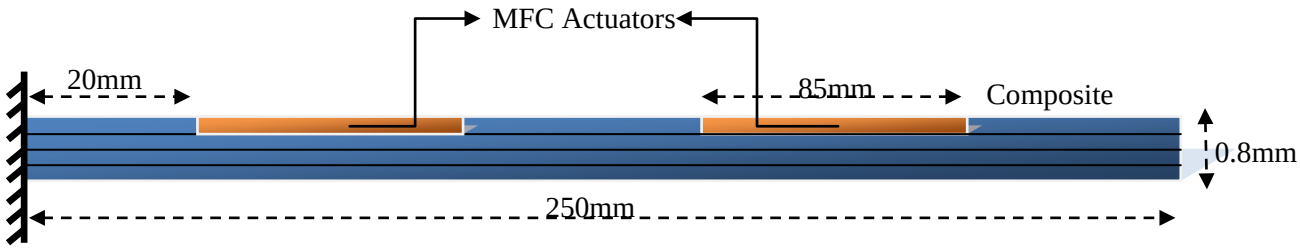

Figure 4.10: Composite plate geometry

Table 4.64: Predicted finite element stresses of the composite plate under 100N out of plane loading

Ply	σ_1 (ksi)	σ_2 (ksi)	τ_6 (ksi)	F_{1t} (ksi)	F_{2t} (ksi)	F_6 (ksi)
0˚	51.1	2.1	0.152	330/33	8.3/11	250
45˚	15.95	1.71	1.71	330/33	8.3/11	250
-45˚	12.8	1.44	1.021	330/33	8.3/11	250
90˚	-0.029	0.6135	0.123	330/33	8.3/11	250
90˚	-0.217	-0.536	0.101	330/33	8.3/11	250
-45˚	-9.25	-1.39	0.903	330/33	8.3/11	250
45˚	-13.8	-1.087	1.23	330/33	8.3/11	250
0˚	-40.26	-0.71	0.025	330/33	8.3/11	250
MFC	**-15.22**	-2.36	0.223	3.58/**4.2**	1.9/2.3	2.5

Table 4.65: Predicted finite element stresses of the composite plate under 1kN out of plane loading

Ply	σ_1 (ksi)	σ_2 (ksi)	τ_6 (ksi)	F_{1t} (ksi)	F_{2t} (ksi)	F_6 (ksi)
0	**551.14**	**23.19**	0.816	**330**/33	**8.3**/11	250
45	183.4	**17.4**	19.13	330/33	**8.3**/11	250
-45	129.5	**17.4**	11.21	330/33	**8.3**/11	250
90	-6.99	7.672	0.614	330/33	8.3/11	250
90	-1.89	-4.67	0.436	330/33	8.3/11	250
-45	**-102.62**	**-13.32**	89.27	330/**33**	8.3/**11**	250

Table 4.65 Continued

Ply	σ_1 (ksi)	σ_2 (ksi)	τ_6 (ksi)	F_{1t} (ksi)	F_{2t} (ksi)	F_6 (ksi)
45	**-131.05**	**-11.8**	120.68	330/**33**	8.3/**11**	250
0	**-406.9**	-7.57	0.0514	330/**33**	8.3/11	250
MFC	**-136.8**	**-23.56**	**4.2**	**3.58/4.2**	**1.9/2.3**	**2.5**

Table 4.66: Predicted finite element stresses of the composite plate under 100°C temperature difference

Ply	σ_1 (ksi)	σ_2 (ksi)	τ_6 (ksi)	F_{1t} (ksi)	F_{2t} (ksi)	F_6 (ksi)
0	-6.41	8.499	0.022	330/33	8.3/11	250
45	-0.265	3.945	0.0703	330/33	8.3/11	250
-45	-4.322	7.73	0.729	330/33	8.3/11	250
90	-1.35	4.49	0.141	330/33	8.3/11	250
90	2.16	7.179	0.133	330/33	8.3/11	250
-45	-3.45	7.788	0.677	330/33	8.3/11	250
45	-2.77	3.959	0.156	330/33	8.3/11	250
0	-3.945	3.988	0.0471	330/33	8.3/11	250
MFC	**6.831**	**3.582**	0.0789	**3.58**/4.2	**1.9**/2.3	2.5

A temperature difference of 100°C is also applied to the composite plate and the corresponding stresses are found as shown in Table 4.66. It can be observed that the

longitudinal and transverse stresses in the MFC actuator exceeded the corresponding strength in that direction which causes failure.

4.4 Carpet Plots

A carpet plot is one that illustrates the interacting behavior of two independent variables, which among other things facilitates interpolation in both variables at once, mainly used as a design tool. Carpet plots can be created for all laminates, where, they are beneficial for the designer to select the appropriate plot for the design application but with the restriction that the laminate must be balanced and symmetric. It is also possible to extend the analysis to include plot for other types of laminates.

A designation of a certain layup is [0m/90n/+-45p]s, where m, n, p denote the number of 0°,90°,+-45° plies, respectively. The in-plane engineering constants of a symmetric laminate depend only on the proportion of the various plies in the entire laminate and not on the exact stacking sequence. Thus, in-plane engineering constants are a function of the fractional values α, β, γ, where

$$\alpha = \frac{2m}{N} \quad \beta = \frac{2n}{N} \quad \gamma = \frac{4p}{N} \tag{4.20}$$

N is total number of plies. As we mentioned a carpet plot is a parametric family of curves with one of the fractions α, β, γ as a variable and the other two as parameters, keeping in mind that $\alpha + \beta + \gamma = 1$. Such plots for Young's modulus, shear modulus, Poisson's ratio, thermal expansion coefficient and moisture expansion coefficient are shown in Figure 4.11-Figure 4.15 respectively for Carbon/Epoxy material (AS4/3501-6).

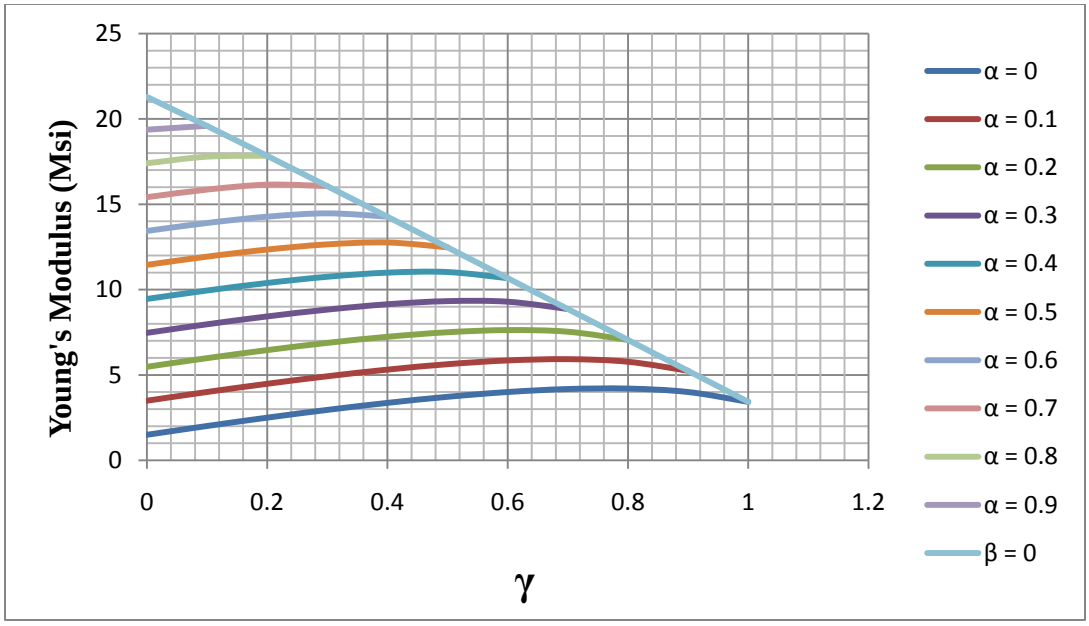

Figure 4.11: Carpet plot for Young's modulus of [90/45/-45/0]s carbon epoxy laminates (AS4/3501-6)

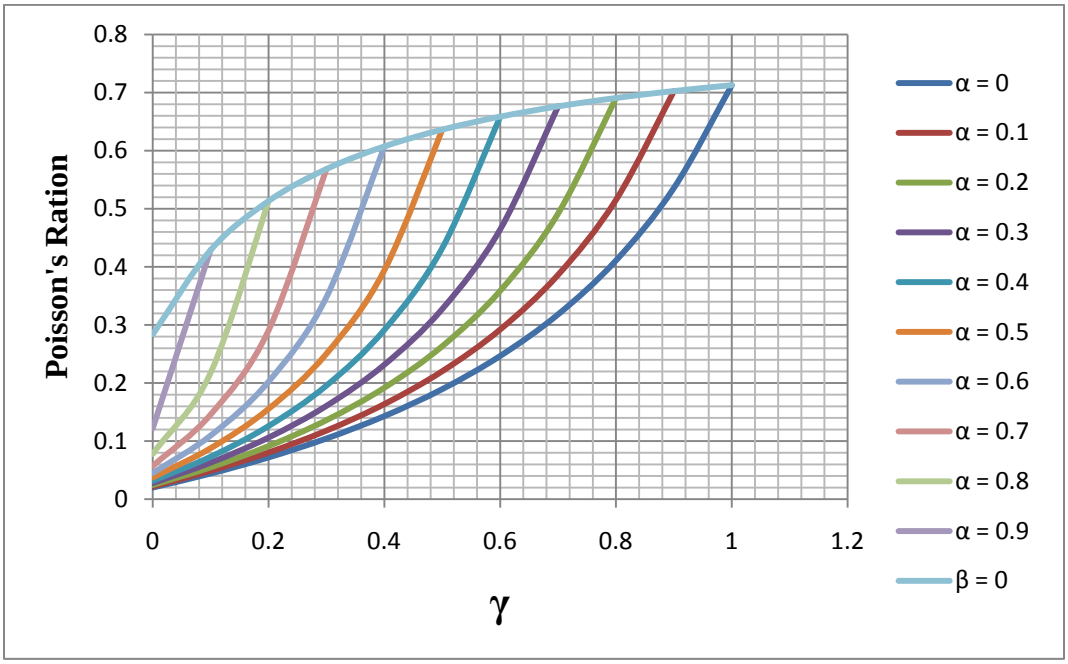

Figure 4.12: Carpet plot for poisson's ratio of [90/45/-45/0]s carbon epoxy laminates (AS4/3501-6)

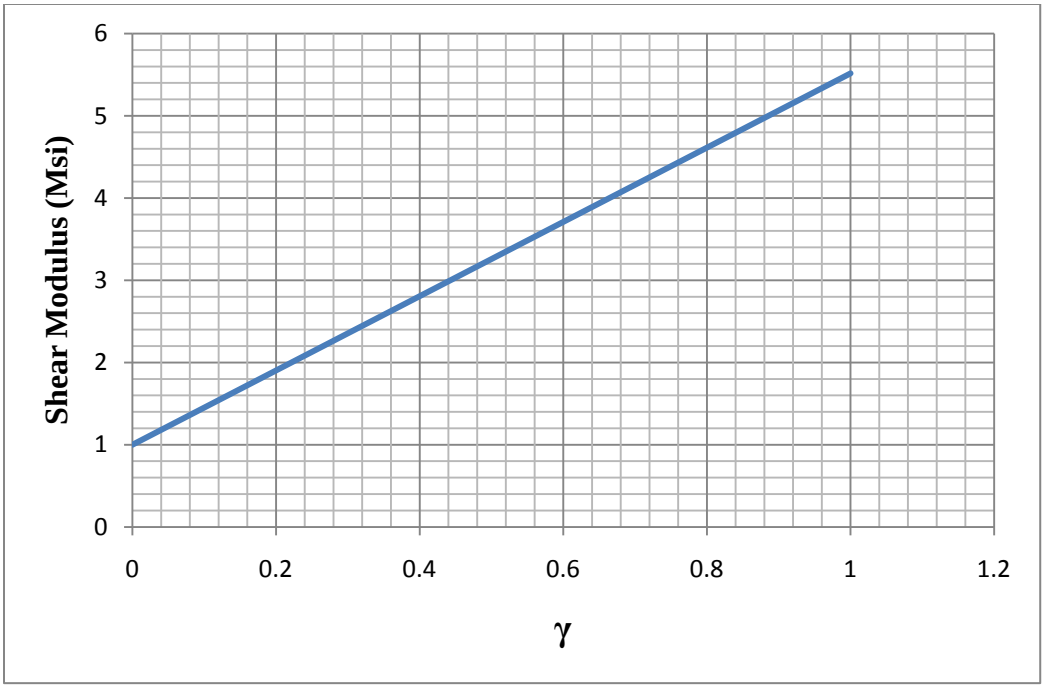

Figure 4.13: Carpet plot for shear modulus of [90/45/-45/0]s carbon epoxy laminates (AS4/3501-6)

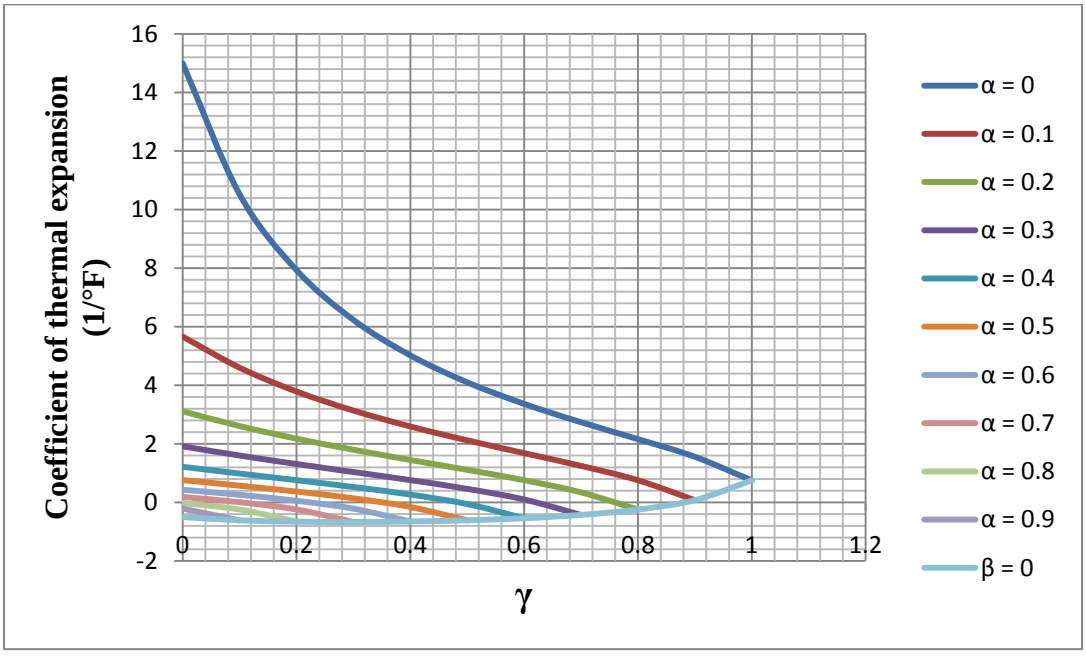

Figure 4.14: Carpet plot for coefficient of thermal expansion of [90/45/-45/0]s carbon epoxy (AS4/3501-6)

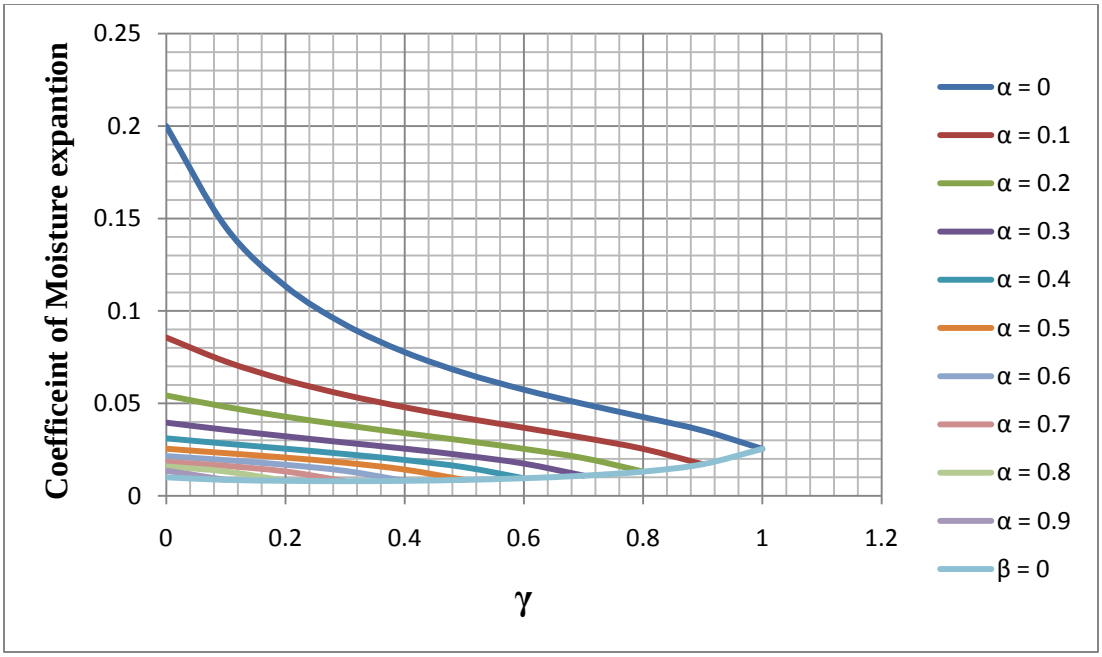

Figure 4.15: Carpet plot for coefficient of moisture expansion of [90/45/-45/0]s carbon epoxy (AS4/3501-6)

CHAPTER V

COMPUTER SOFTWARE AND CONTROL DESIGN

The following chapter introduces the computer software “Hyper Composite” that enables the user to analyze composite laminates under uniaxial tensile loading including both hygrothermal and electrical effects. The results of the program are compared with those obtained in Chapter IV. A control algorithm is proposed that prevents the failure load of the composite laminate to be reached based on the results obtained from the FPF and ULF. The results are used to obtain a recommended voltage value which can be actuated through the active parts of the composite laminate to prevent failure from occurring. A practical control circuit is also proposed and implemented through the simulation software PROTEOUS. A programmable interfacing circuit (PIC) is used as part of the control circuit which is works as the feedback part that biases the actuators whenever the stress value exceeds that of failure.

5.1 The Hyper Composite

The Hyper Composite is an engineering program that analyzes laminated composite plates according to the classical laminated plate theory and includes the effects of both hygrothermal and electrical properties. Familiarity with such analysis is assumed. Input consists of hydro-thermo-electro-mechanical properties for each ply, ply fiber orientation and thickness, stacking sequence, temperature changes, moisture content and electric field. The program calculates the laminate stiffness "ABD" matrices, lamina failure load and mode based on Maximum Stress, Maximum Strain, Tsai-Hill, and Tsai-Wu failure theories, failure load and mode for the entire laminate

based on first ply failure (FPF) and ultimate laminate failure (ULF) criteria's. In addition, carpet plots for orthotropic laminates can be generated that gives the user the ability to generate different carpet plots for different materials, ply angles and types. Moreover, the user has the ability to assign different materials to different plies which in this case provides the capability to analyze hybrid composites. The main screen of the software interface is shown in Figure 5.1; it provides the user with several options to choose from. First, the user can select the desired unit to work with i.e. (English-SI). There are also built-in materials the user can choose from or input their own material properties using the window shown in Figure 5.2. The user also has the ability to enter the laminate stacking sequence, ply thickness and the desired failure theory for the analysis.

Another unique part of the program is the option of defining a hybrid material only by clicking on the hybrid composite button at the bottom of the screen below as in Figure 5.3. This gives the user the ability to enter different types of material and different angles for each ply. After entering the input data, click on calculate, the software starts performing the analysis and the requested output data will be obtained. The laminate stiffness matrices are calculated, and the minimum failure stress for each ply and its corresponding failure mode are obtained, and the minimum failure stress of the whole laminate is calculated as well. The laminate failure stress can be calculated based on two different criteria, FPF, ULF. Also, the stiffness reduction factors due to ply failure that are used in the ULF criteria are inputs to the program, so by changing the values of these factors the user can observe the change in the laminate strength.

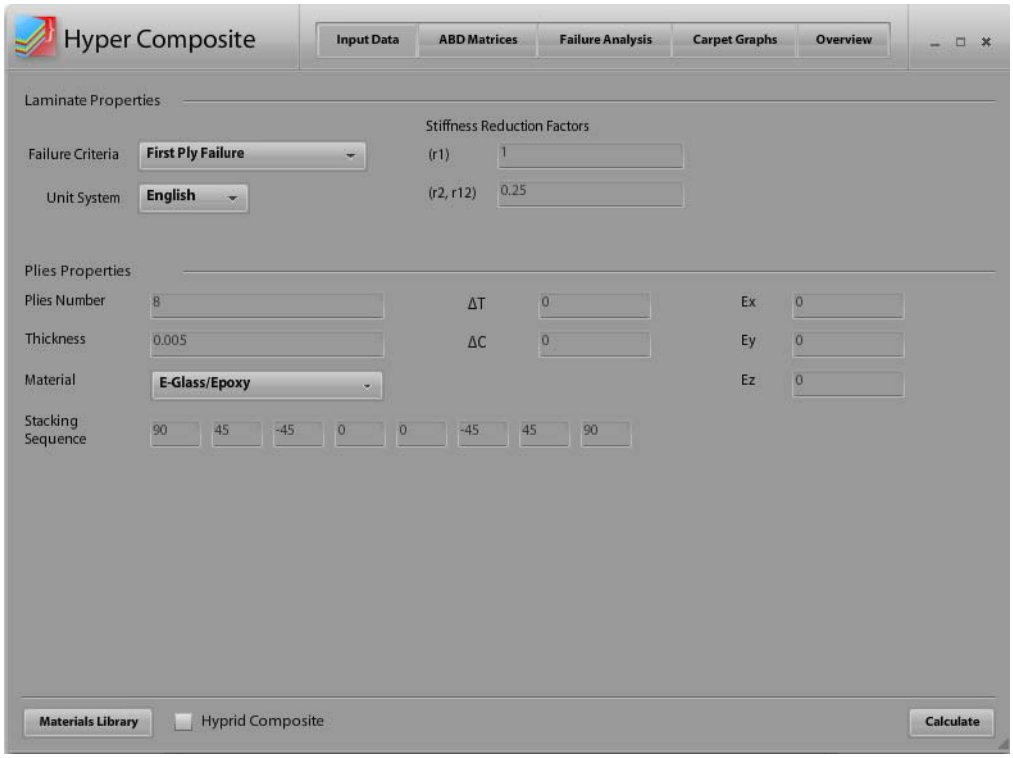

Figure 5.1**:** Main program screen

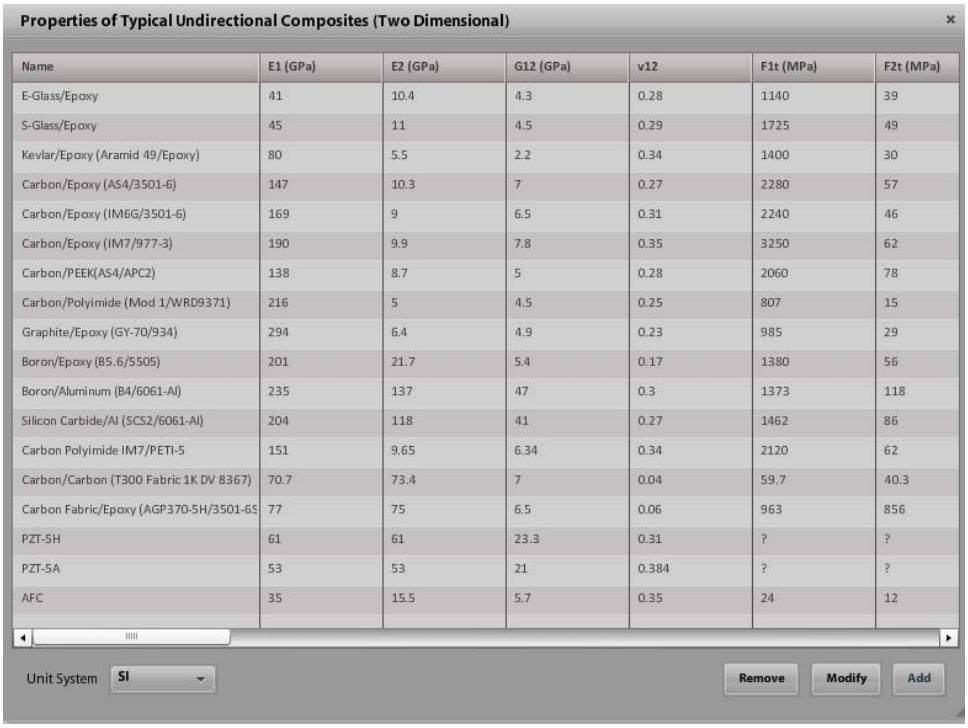

Figure 5.2**:** Material property window

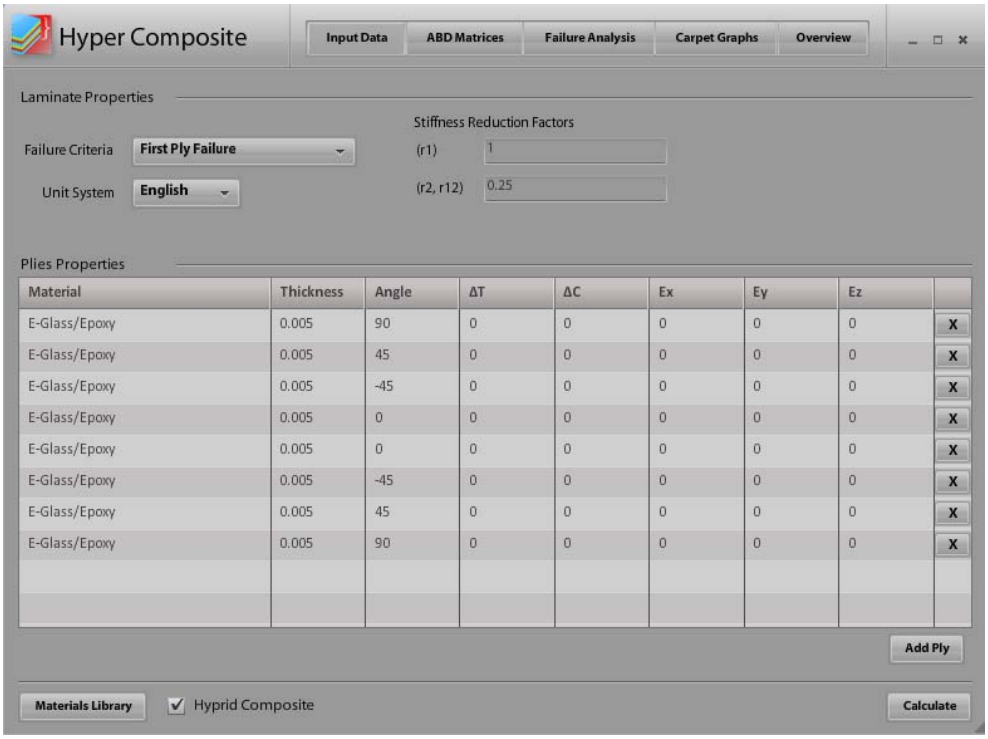

Figure 5.3: Hybrid composite window

5.2 Result Verification

Failure stress analysis is now presented using the Hyper Composite. The results are compared with those obtained from the previous chapter and with available experimental results. Using the same model that was used in the sample calculation of the previous chapter which is a symmetric laminate having a stacking sequence of $[90/45/-45/0]_s$ and ply thickness of 0.005 inch. The material is Carbon/Epoxy (AS4/3501-6). By specifying the following inputs as shown in Figure 5.4 and identifying the maximum stress theory as our failure theory. By clicking on the calculate button shown in the figure we get the **A, B, D** matrices as in Figure 5.5.

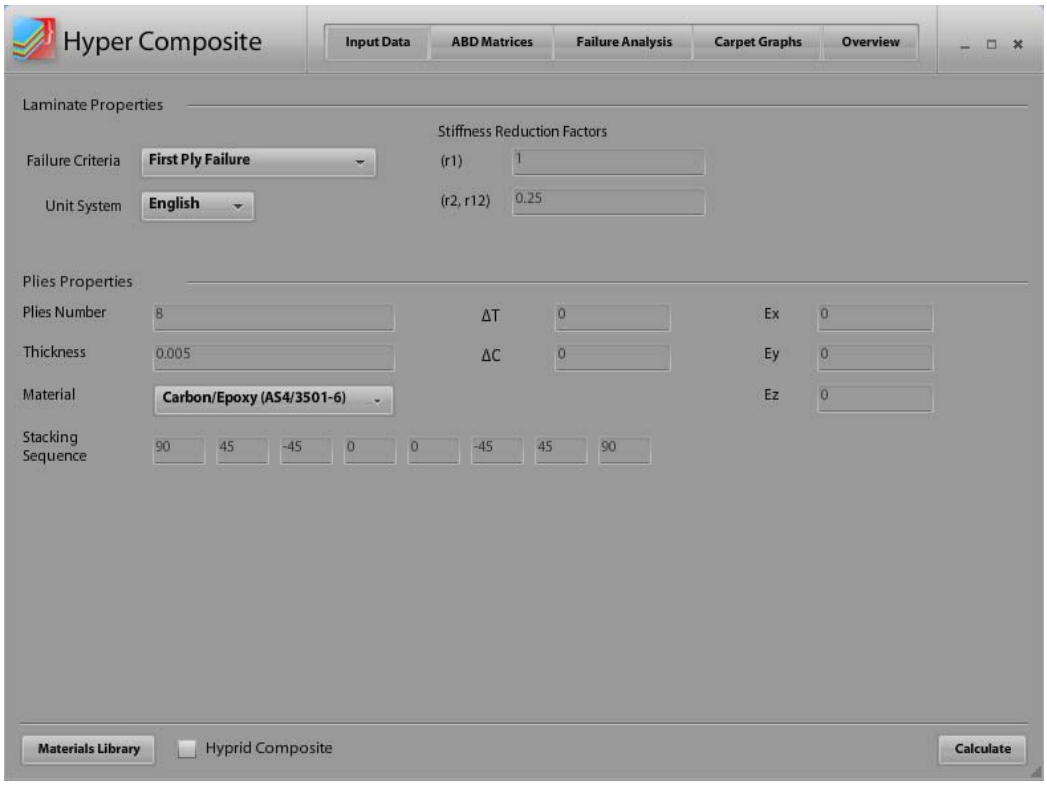

Figure 5.4: Data input to the program

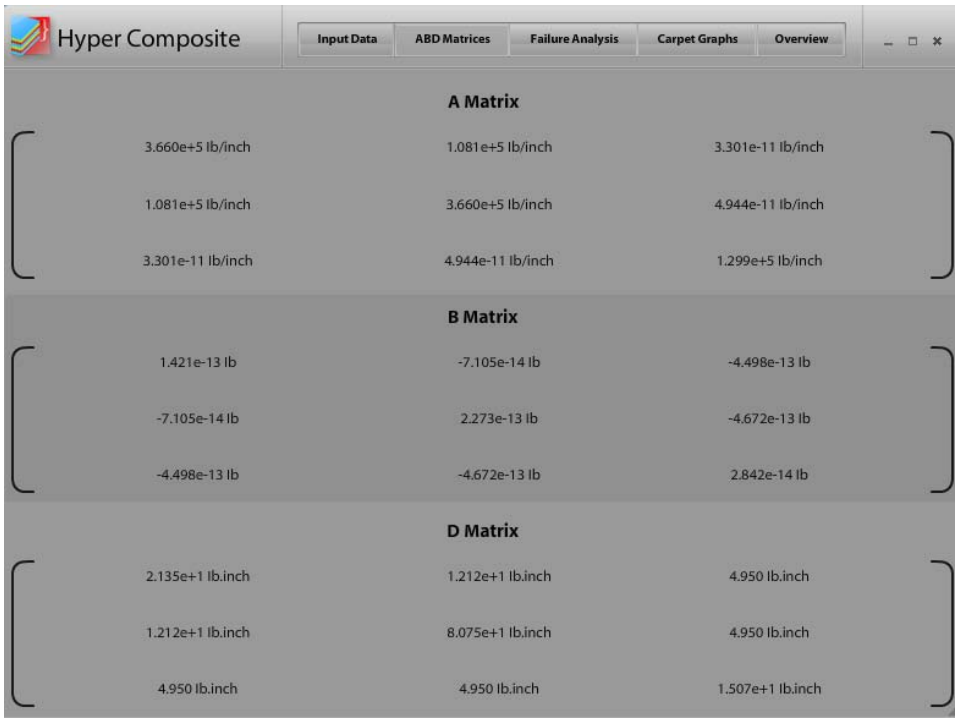

Figure 5.5: Laminate stiffness matrices

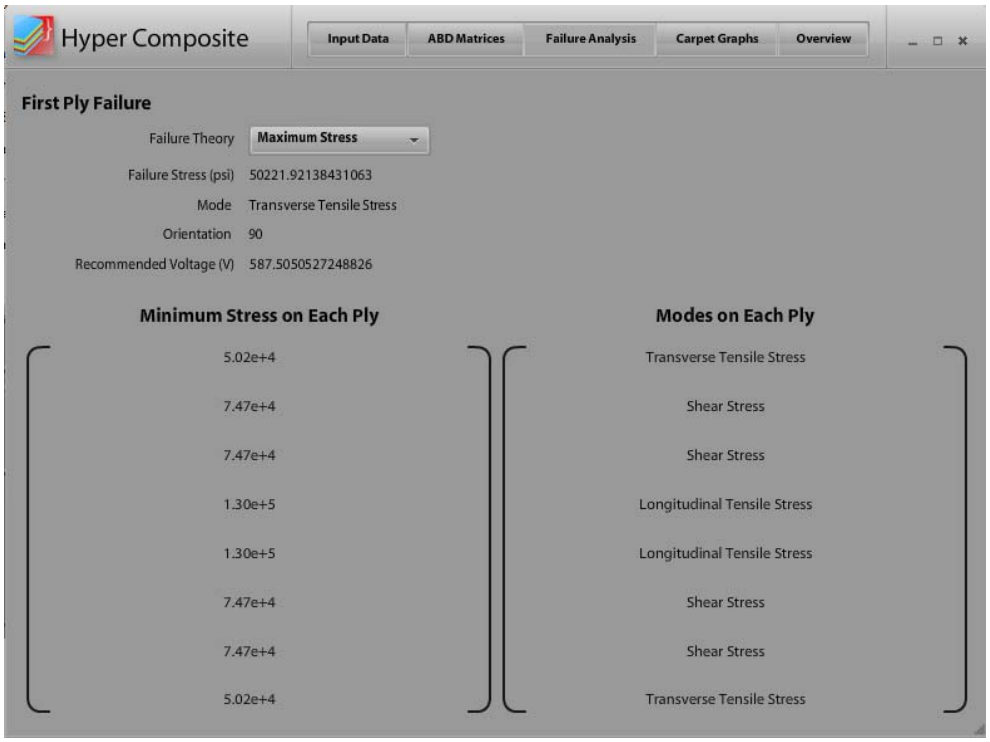

Figure 5.6: Failure stress of each lamina in the composite layup

As shown in Figure 5.6, the result of the FPF is identical to the value obtained from the analytical calculations, and also the values of the loads and modes for each lamina are also identical as shown in Figure 5.6. By changing the analysis type to the ULF criteria, we obtain the results shown in Figure 5.7.

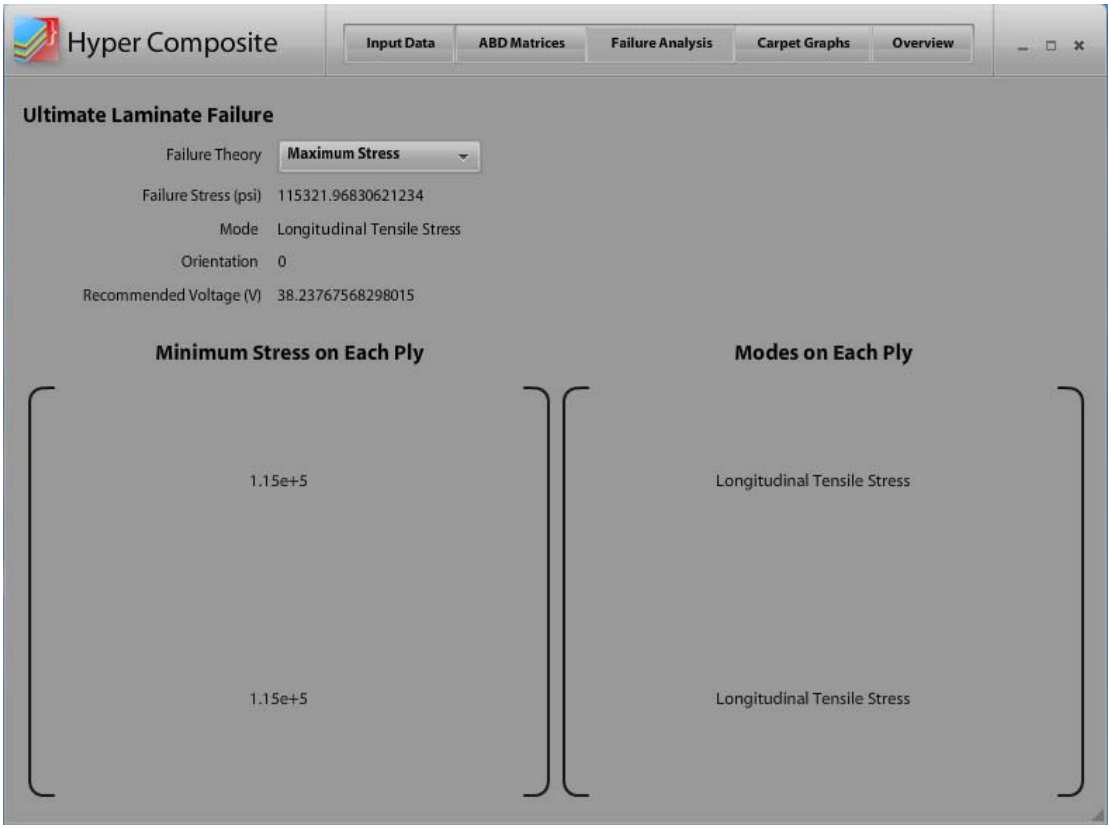

Figure 5.7: Failure stress base on the ULF criteria

Figure 5.8 shows a comparison between the ULF stress obtained from the computer software and experimental values introduced in the previous chapter where; 1, 2, 3, 4 that appear on the x axis indicate the following stacking sequences respectively; $[0/90_2]_s$, $[0_2/90_2]_s$, $[0/+\text{-}45]_s$, $[+\text{-}20]_s$, for Carbon Epoxy (AS4-3601).

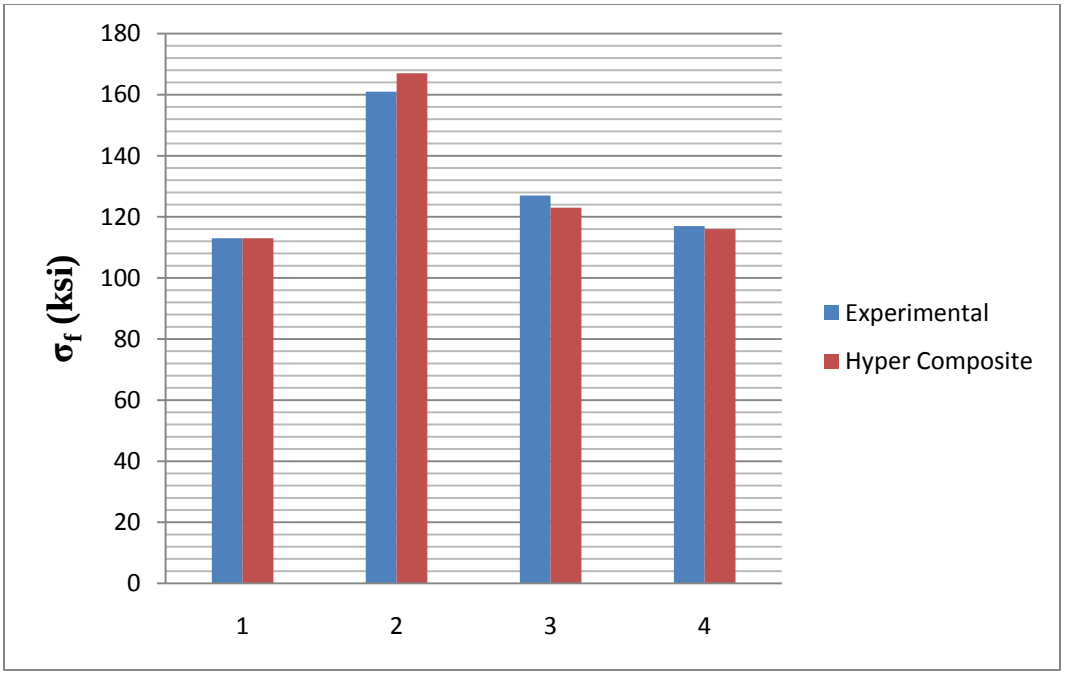

Figure 5.8: Comparison between ULF values from experiment [40] and program

5.3 Control Design

The following section presents a control design that can be applied to systems that are affected by external stimuli which influence their overall behavior. Figure 5.9 and Figure 5.10 present the methodology and the algorithm proposed for this design respectively; it can be observed that by using such technique, it provides the system with a warning that leads the controller to react against it by sending a bias to the actuator in order to activate and overcome the stress or any other desired outcome.

In the present study, we take advantage of a certain type of microcontroller which is often used in practical applications due to its feasibility and low cost compared to other micro-controlling chips.

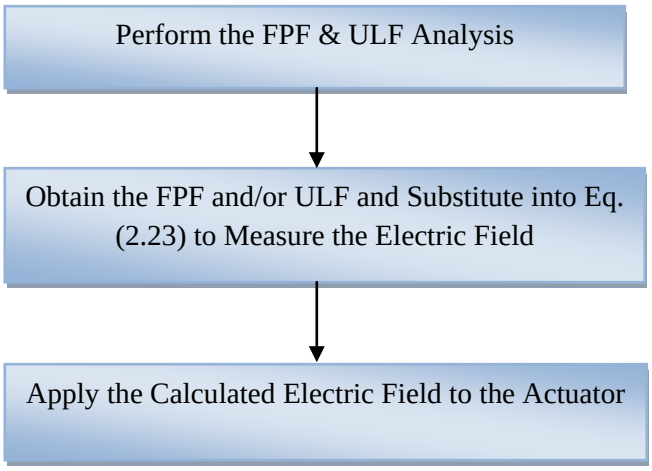

Figure 5.9: Control methodology

This type is known as the Programmable Interfacing Chip (PIC). PIC is a single chip that can stand all functions of microprocessor system like storing data, compiling and downloading programs. This chip is coded using assembly or C language which then can be download as a hex code to the chip to make it the heart for the circuit in which it is inserted to.

The operating voltage rating for driving the PIC is around 2V up to 6V but is recommended to use 5V for allowing simplicity in design and for using switching power supply for more filtration against noise. This type of chip can be used in several applications such as controlling, security purposes, communication medical instruments and power applications.

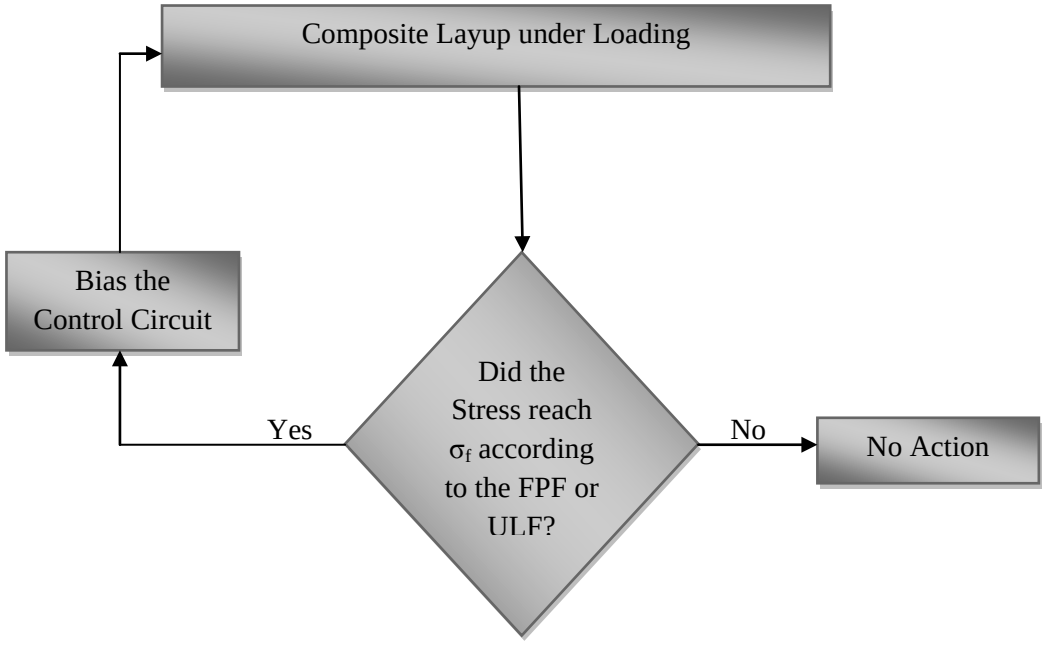

Figure 5.10: Control Algorithm

In order to design the circuit, the PIC chip is used as the smart part of the controlling circuit. The program is written in PIC C Compiler. The main goal of its use is to bias the actuator the recommended voltage value whenever the failure stress or any other controlling parameter is reached depending on the values obtained from the FPF and ULF analysis or any other method. The controlling parameter could also be multiplied by a safety factor before reaching its critical (threshold) value. A simulation of the overall circuit is shown in Figure 5.11. This simulation is done using the simulation program PROTEOUS. A practical circuit is also conducted and the control is simulated by using a potentiometer as the condition at which the PIC gives bias to the actuator. Figure 5.12 shows the practical circuit constructed.

The PIC is programmed to simulate the control methodology as follows; when the potentiometer value is changed (increase or decrease resistance) as shown on the LCD monitor, the value of the FPF is alternating and when it exceeds a certain threshold the LED switches on indicating that the PIC biased the circuit with a voltage to overcome the disturbance.

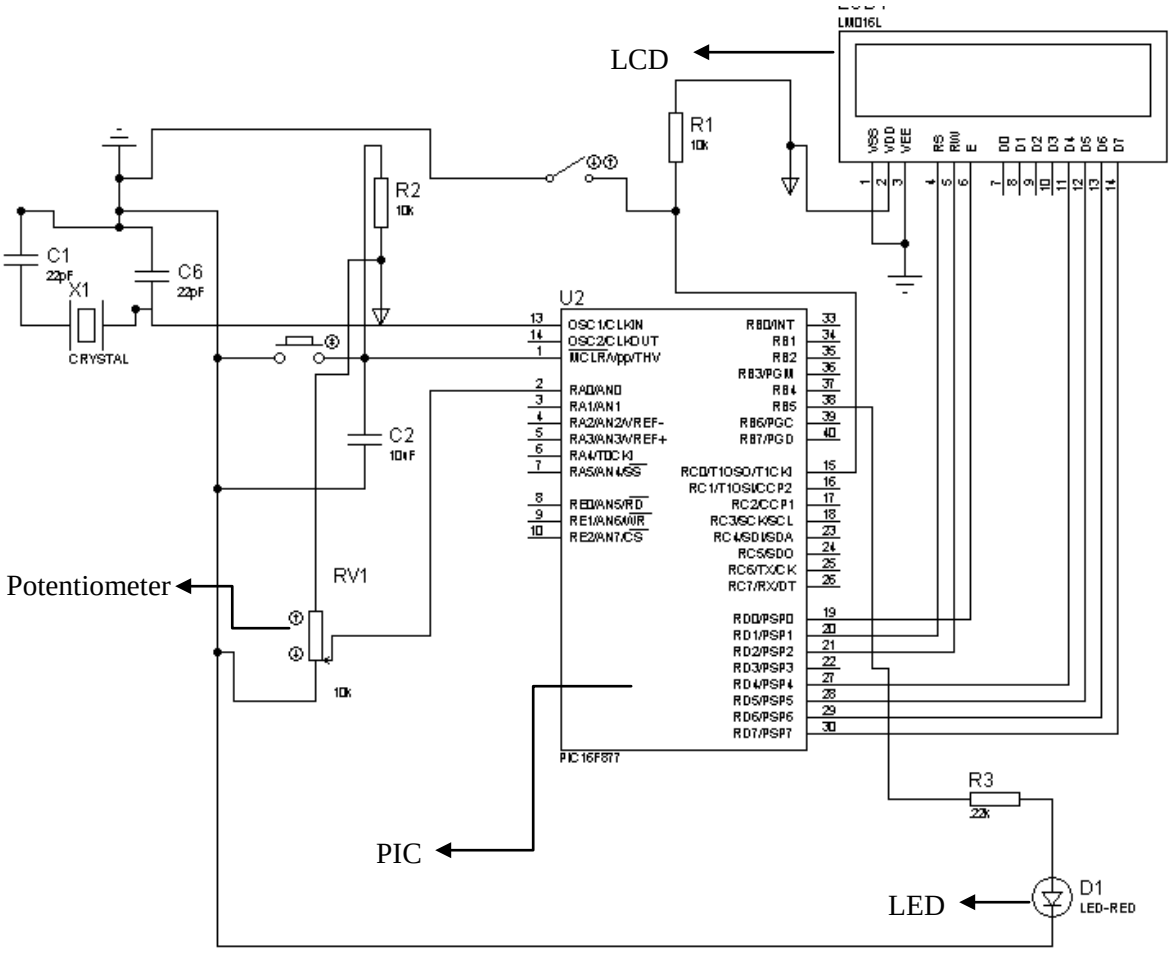

Figure 5.11: Circuit simulation

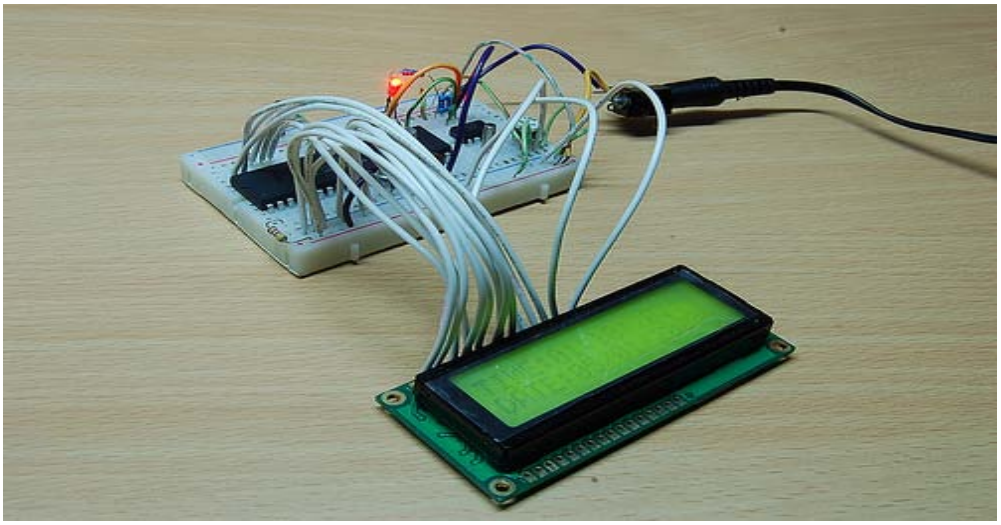

Figure 5.12: Practical circuit implementation

From this analysis, it can be concluded that a feed back control algorithm can be possibly implemented for composite laminates through the use of microcontrollers as the part which gives the orders to bias the actuators in case the stress value exceeded that of failure. It is also possible to use other criteria for controlling the response to prevent failure.

In order to apply the control scheme, the finite element software Abaqus is used to simulate a case study. The simulation considers a laminated composite plate with two MFC actuators embedded into the first ply of the laminate. The plate is cantilevered at one end and subjected to thermal loading. The main goal is to compensate for the distortion caused by the thermal gradient which is applied to the composite plate. The finite element model is used on a $[0/90_3]$s laminate with two MFC actuators embedded into the composite structure. The material used and their properties are shown in Table

5.1. The geometry of the composite plate with the MFC actuators is shown in Figure 5.13. By using the Hyper Composite, the FPF occurs in the 90 ply at a value 396 MPa. In order to prevent this load from being reached, a counter voltage equal to 1000V is applied to the actuators obtained from the hyper composite. The structure is subjected to a linear increase in a temperature difference from a reference temperature of 94°C. The temperature distribution with respect to the analysis step is shown in Figure 5.14. The evolution of voltage applied to the MFC actuators is represented in Figure 5.15. In the first three steps, the actuators are inactive and no voltage is applied. From the third step to the tenth step, electric potential is applied to compensate for the thermal deformation that is induced by the temperature increase. Figure 5.16 shows the calculated plate end displacement in the x_3-direction with and without actuation. The displacements can be compared to the reference position. Without control, the plate end undergoes a displacement of about 18 mm from the reference position while by using a controller; the plate end undergoes a displacement of 10 mm in the tenth step.

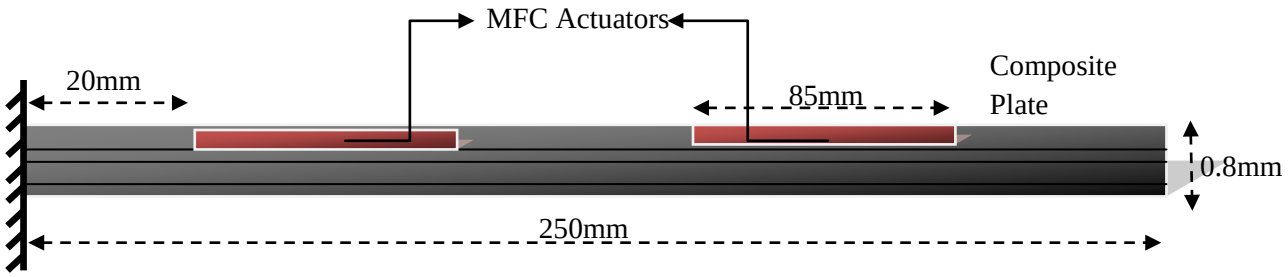

Figure 5.13: Composite Plate with 2 MFC actuators embedded

Table 5.1: Material Properties [45]

Material Property	Panex 33/RS-1	MFC
E_1 (GPa)	101	30.3
E_2 (GPa)	7.91	15.9
E_3 (GPa)	7.91	11.47
ν_{12}	0.318	0.31
ν_{13}	0.318	0.289
ν_{23}	0.458	0.327
G_{12}(GPa)	3.01	5.5
G_{13}(GPa)	3.01	2.6
G23(GPa)	2.71	2.14
α_1 (µ/°C)	-0.0598	5.9
α_2(µ/°C)	41.7	29.6
α_3(µ/°C)	41.7	19
d_{11} (pm/V)	-	360
d_{12} (pm/V)	-	-190
d_{13} (pm/V)	-	-190
t (mm)	0.3	0.3

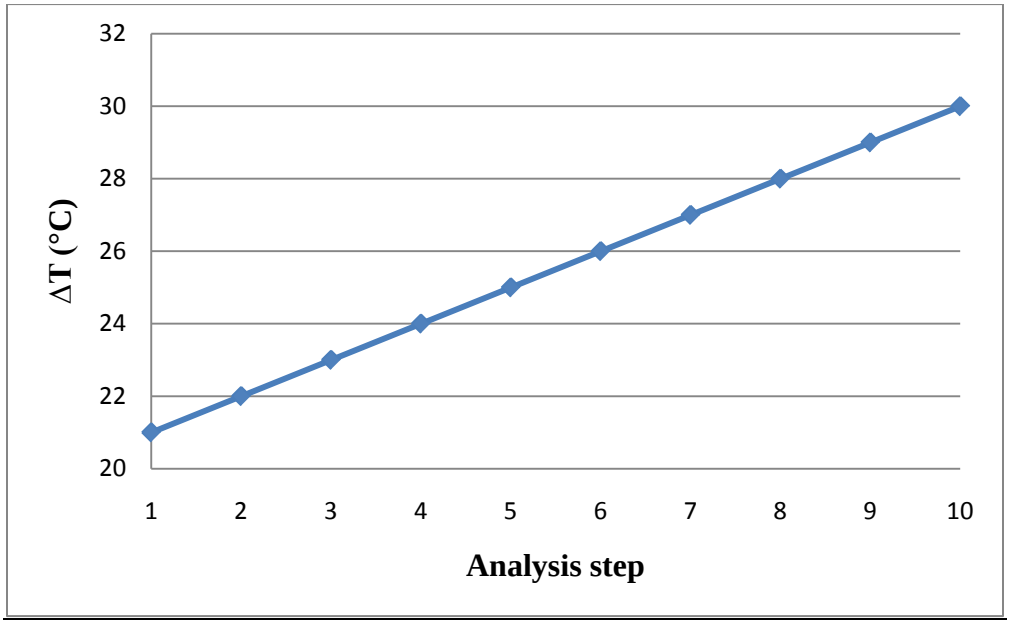

Figure 5.14: Temperature difference variation

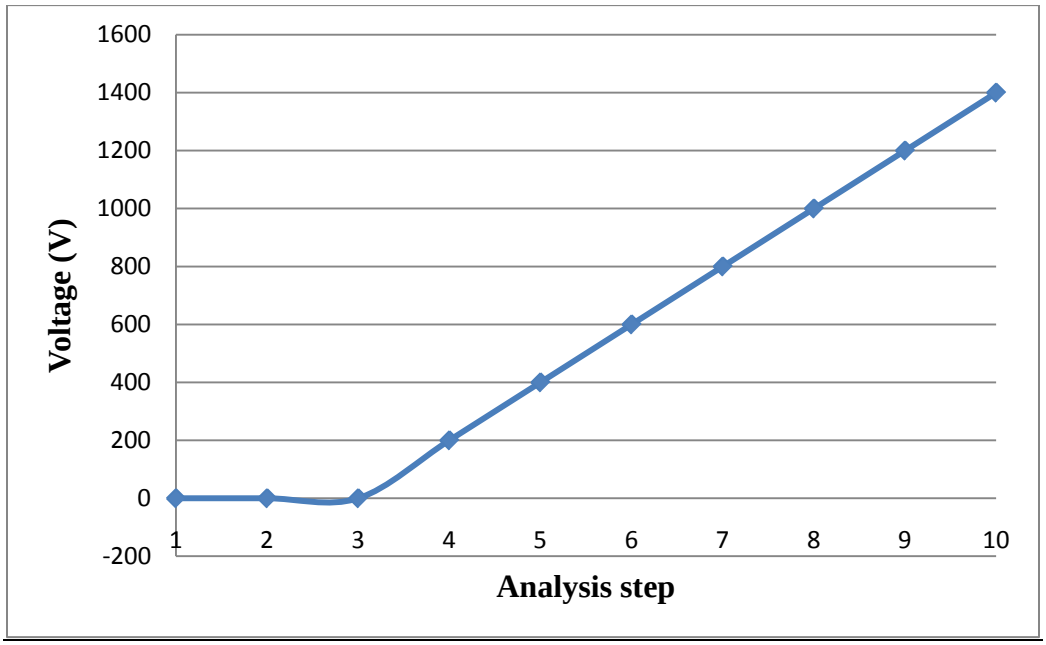

Figure 5.15: Electric potential variation

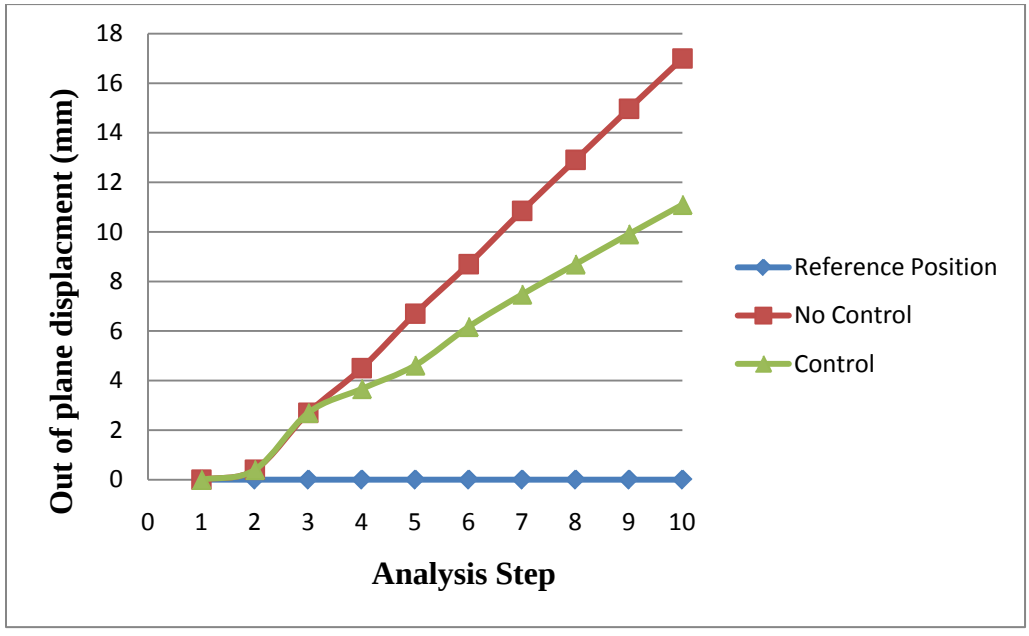

Figure 5.16: Composite Plate displacement

CHAPTER VI

CONCLUSION AND SUMMARY

6.1 Discussion

The present study focused on the use of piezoelectric materials as actuators such as PZT and other piezoelectric fiber composites: Active fiber composites (AFC) and Microfiber composites (MFC) for shape control of composite laminates. Due to the debondining of the actuator from the host structure which will eventually lead to failure caused by the high stress concentration between the interface of the host structure and the active part, we used embedded actuators, such that, the active part is incorporated into one of the layers of the composite beam during the manufacturing process where the stress concentration due to discontinuity in geometry will reduce while obtaining similar or even higher actuation values. Failure analysis of composite laminates was also considered under coupled mechanical, hygrothermal and electrical effects. The first-ply failure and ultimate laminate failure criteria of composite laminates were used in order to predict the failure stress and mode for any general composite laminate by incorporating various commonly known macroscopic failure criteria including Tsai-Hill, Tsai Wu, Maximum stress and Maximum Strain. A detailed calculations based on the Classical Laminate Theory (CLT) was performed for Carbon/Epoxy (AS4/3501-6) laminate with stacking sequence $[90/45/-45/0]_s$ under uniaxial and biaxial loading. Failure analyses were also performed on smart composites having both PZT and AFC layers. The effect of temperature and moisture content on the failure values was also taken into account where they had significant effect on the FPF and less on the ULF values. User friendly

software called the Hyper Composite was also constructed using Action Script that enables the user to analyze any composite material layup under uniaxial loading including temperature, moisture and electrical effects. The program gives the ability to generate a set of carpet plots including Young's modulus, Poisson's ratio, shear modulus, coefficient of thermal expansion and coefficient of moisture expansion at different percentile laminate angles and materials. Moreover, a control algorithm was proposed that enables the composite laminate to overcome the failure load by using an active material such as AFC, MFC or PZT where, a counter electric voltage could be applied which prevents failure from occurring. The finite element software ABAQUS was used to simulate a case study. A control circuit was also proposed using a PIC microcontroller as the feedback part, simulated using PROTEOUS software in addition to a practical implementation of the circuit.

6.2 Conclusion

Failure analysis of smart composite laminates was studied in the previous work. The failure has been investigated from a macromechanical point of view. It was concluded that the failure mechanisms and processes vary widely with type of loading and are intimately related to the properties of the constituent phases, i.e., matrix, reinforcement, and interface-interphase. Numerous failure theories were used in the analysis. They can be classified into, limit or noninteractive theories (maximum stress, maximum strain) and interactive theories (Tsai-Hill, Tsai-Wu). The validity and applicability of a given theory depends on the convenience of application and agreement with experimental results. A wide variation has been observed in the prediction of

laminate failures by the various failure theories and the divergence in the predictions is greater for FPF than for ULF. In the uniaxial loading case, the failure always occurred in the layers that have fibers oriented perpendicular to the direction of the load application, while in the biaxial case, it was observed that the failure occurred in all the plies simultaneously when the fraction of both loads are equal. The effect of temperature and moisture content on the failure analysis of composite laminates had significant contribution in the FPF than the ULF. The control methodology proposed was practically implemented using a simple circuit to demonstrate the failure process. A PIC microcontroller was used as the controlling feedback part of the overall circuit.

Piezoelectric materials are usually used as smart sensors and actuators with the ability to correct surface errors of antenna reflectors or other microwave devices used in orbital satellites which require high surface precision. Surface errors are introduced by manufacturing errors, thermal distortion in orbit, moisture, loose joints, material degradation and creep. These reflectors are made of graphite–epoxy structures because of requirements for low thermal distortion. Significant time and cost are spent during fabrication, analysis and ground tests to minimize and determine the surface errors. Even with this effort, several current spacecraft antennas have experienced degraded performance due to higher than predicted surface errors. Therefore, smart structure technology has the potential of not only improving the performance of these structures, but also reduction in cost for analyses and ground tests. The previous study focused on the use of piezoelectric and piezoelectric fiber composite actuators to control the shape of composite laminates. It was concluded that PZT-5H had the highest actuation value

when considering the 31 mode while AFC was the dominant in the 33 mode. It was also observed that when embedding the actuator into the composite laminate, the stress concentration effect reduces while obtaining higher actuation values.

6.3 Future Work

Several extensions on the current study could be performed; first, experimental study could be conducted related to the shape control of composite laminates using the actuators mentioned in the analysis which can be used for verification purposes and further enhancements of the methods used for shape control of such structures. Several other loading conditions other than uniaxial and biaxial loading could be considered such as out of plane loading and observe their effect on the failure of composite laminates. Piezoelectric fiber composites such as AFCs and MFCs are often utilized for applications at high mechanical loading and electric field. Under such conditions, significant amount of heat could be generated increasing temperatures. At elevated temperatures, materials could experience significant time-dependent behaviors. The effects of viscoelastic matrix on the overall properties of PFCs could be taken into account while studying there feasibility in the shape control or even dynamic control of such structures. Practical implementation of the control methodology could be performed on composite structures by incorporating several different external stimuli to the structure and observe the power of the active part to overcome these distortions.

REFERENCES

[1] Sandhu, R.S. A survey of failure theories of isotropic anisotropic materials. Technical Report, AFFDL-TR-72-7 I; 1972.

[2] Drucker, D.C. Yielding flow and failure in inelastic behavior of composite materials. J ASME, New York 1975; 13: 1-12.

[3] Hemelrijck, D.V., Makris, A., Ramault, C., Lamkanfi, E., Van Paepegem, W., Lecompte, D. Biaxial testing of fiber-reinforced composite laminates. J. Materials, Design and Applications 2008; 222: 231-239.

[4] Reddy, J.N., Pandey, A.K. A first-ply failure analysis of composite laminates. J Composites and Structures 1986; 25: 371-393.

[5] Mayes, J.S., Hansen, A.C. Composite laminate failure analysis using multicontinuum theory. J Composites Science and Technology 2003; 64: 379–394.

[6] Yang, N.H., Nayeb-Hashemi, H., Vaziri, A. multi-axial failure models for fiber-reinforced composites. J of ASTM International 2006; 4:1-13.

[7] Takeda, T., Takano, S., Shindo, Y., Narita, F. Deformation and progressive failure behavior of woven-fabric-reinforced glass/epoxy composite laminates under tensile loading at cryogenic temperatures. J Composites Science and Technology 2005; 65: 1691–1702.

[8] Pipes, R. B., Vinson, J. R., Chou, T. W. On the hygrothermal response of laminated composite systems. J Composite Materials 1976; 10: 129-148.

[9] Shen, C. H., Springer, G. S. Moisture absorption and desorption of composite materials. J Composite Materials 1976; 10: 2-20.

[10] Upadhyay, P.C., Lyons, J.S. Effect of hygrothermal environment on the bending of PMC laminates under large deflection. J Reinforced Plastics and Composites 2000; 19: 465-491.

[11] Chamis, C.C. Simplified composite micromechanics equations for hygral, thermal and mechanical properties. NASA Technical Memorandum 83320. Prepared for the 38th Annual Conference of the Society of the Plastics Industry, Reinforced Plastics Institute, Houston, TX 1983; 1-10.

[12] Gandhi, M.V., Thompson, B. S. Smart materials and structures. Springer; 1992.

[13] Newnham, R.E. Ferroelectric sensors and actuators: smart ceramics. In: Setter N, Colla EL. J Ferroelectric Ceramics 1993; 363–80.

[14] Koconis, D. B., Kollár, L. P. and Springer, G. S. Shape control of composite plates and shells with embedded actuators. J Composite Materials 1994; 28: 459-482.

[15] Agrawal, B.N. Spacecraft vibration suppression using smart structures. Proceeding of the 4th Int. Congress on Sound and Vibration, 1996.

[16] Tiersten, H.F. Linear piezoelectric plate vibrations. Plenum Press, New York; 1969.

[17] Parton, V.Z., Kudryavstev, B.A. Electromagnetoelasticity: piezoelectrics and electrically conductive solids. Gordon and Breach Science Publ, New York; 1988.

[18] Preumont, A. Vibration control of active structures: an introduction. Kluwer Academic Publishers, Dordrecht, 2002.

[19] Rogacheva, N.N. The theory of piezoelectric shells and plates. CRC Press, Boca Raton; 1994.

[20] Lee, C.K. Theory of laminated piezoelectric plates for the design of distributed sensors/actuators Part I: governing equations and reciprocal relationships. J Acoust Soc 1990; 87: 144–58.

[21] Lee, C. K. Piezoelectric laminates: theory and experiments for distributed sensors and actuators. J Intelligent Structural Systems 1992; 28: 75–167.

[22] Lee, C.K. Moon, F.C. Modal sensors/actuators. J Applied Mechanics 1990; 57:434–41.

[23] Kam, T.Y., Sher, H.F. Nonlinear and first ply failure analysis of laminates composite cross plies plates. J Composite Materials 1994; 29: 463-482.

[24] Tzou HS, Zhong JP, Hollkamp JJ. 1994. Spatially distributed orthogonal piezoelectric shell actuators: theory and applications. J Sound Vibration 1994; 177: 363–378.

[25] Agrawal, S.K., Tong, D., Nagaraja, K. Modeling and shape control of piezoelectric actuator embedded elastic plates. J Intelligent Material System Structure 1994; 5: 514–522.

[26] Pagano, N.J. Exact solutions for rectangular bidirectional composites and sandwich plates. J Composite Materials 1970; 4:20–34.

[27] Wu, C.P., Chiu, K.H.,Wang, Y.M. A review on the three-dimensional analytical approaches of multilayered and functionally graded piezoelectric plates and shells. J Computation Material Continua 2008; 8: 93–132.

[28] Atkin, R. Shi, X. Bullough, W. Solution of the constitutive equations for the flow of an electrorheological fluid. J. Rheol 1991; 35: 1441–1461.

[29] Toupin, R.A. 1956. The elastic dielectric. Archives of Rational Mechanics and Analysis 1956; 5: 849–915.

[30] Knops, R.J. Two-dimensional electrostriction. J Mechanics Applied Mathematics 1963; 16 77–88.

[31] Pedro, P. C., P.P. De Engenharia, D.F. Advances in the simulation of damage and fracture in composite structures. Proceeding of Abaqus Conference 2005.

[32] Dragan, D. 1998. Ferroelectric, dielectric and piezoelectric properties of ferroelectric thin films and ceramics. Reports on Progress in Physics 1998; 61: 1267-1324.

[33] Reddy, J.N. On laminated composite plates with integrated sensors and actuators. J Engineering Structures 1999; 21: 568–593.

[34] Nelson, J.G. Neurgaonkar, R.R. Oliver, J.R. Larson, C. Dobbi, S.K. Rosenthal, J.S. Piezoelectric technology research and applications in smart materials and structures. Smart Materials Technologies, Proceedings of SPIE 1998.

[35] Gentilman, R. McNeal, K. and Gerald, S.G. Enhanced performance active fiber composites. Procedding of the Smart Structures and Materials Conference 2003.

[36] Wilkie, W.K. Bryant, R.G. High, J.W. Fox, R.L Hellbaum, R.F. Jalink, A. Little, B.D. Mirick, P.H. Low-cost piezocomposite actuator for structural control applications. Procedding of the Smart Structures and Materials Conference 2000.

[37] Williams, R., Schultz, M., Hyer, M., Inman, D., Wilkie, W. Nonlinear tensile and shear behavior of macro fiber composite actuators. J Composite Materials 2003; 38: 855-869.

[38] Agrawal, B.N. and Treanor, K.E. Shape control of a beam using piezoelectric actuators. J of Smart Material and Structures 1999; 8: 729–740.

[39] Donald J. Leo, D.J. Engineering analysis of smart material systems. John Wiley & Sons, Inc; 2007.

[40] Daniel.,I.M, Ishai., O, Engineering mechanics of composite materials. Oxford University Press; 1994.

[41] Dent,A.C.E., Bowen, C.R., Stevens, R., Cain, M.G., Stewart, M. Tensile strength of active fiber composites – prediction and measurement. J Ferroelectrics 2008; 368: 209–215.

[42] Fett, T., Munz, D., Thun, G. Tensile and bending strength of piezoelectric ceramics. J Materials Science 1999; 18: 1899 –1902.

[43] Bhalla, S., and Soh,C. Progress in structural health monitoring and non-destructive evaluation using piezo-impedence transducers. Smart Materials and Structures: New Research, Nova Science Publishers; 2006.

[44] Darwish.,F.H, Shivakumar., K.N, Hamoush., S. “Performance of patch repaired composite panels – static and fatigue” Proceeding of the AIAA/ASME/ASCE/AHS/ASC Structures, Structural Dynamics, and Materials Conference 2006.

[45] Dano, M.L., and Julli`ere, B. Active control of thermally induced distortion in composite structures using macro fiber composite actuators. J Smart Materials and Structures 2007; 16: 2315–2322.

VITA

Zeaid Fouad Mohammed Hasan received his Bachelor of Science degree in mechanical engineering (aeronautics division) from Jordan University of Science and Technology, Jordan in June 2009. He entered the mechanical engineering program at Texas A&M University in September 2009 and received his Master of Science degree in December 2010. His research interests include solid mechanics and design. He plans to pursue his Doctor of Philosophy degree in this area. Mr. Hasan can be reached at Dorothy Building, Room 301, Texas A&M University, College Station, Texas, 77843. His email address is zeadnws@hotmail.com.